Measurement of low sediment concentrations in a pipe flow

A deep sea mining application

MSc Offshore and dredging technology

Sven Cornelis Theodorus Laken

Delft University of Technology

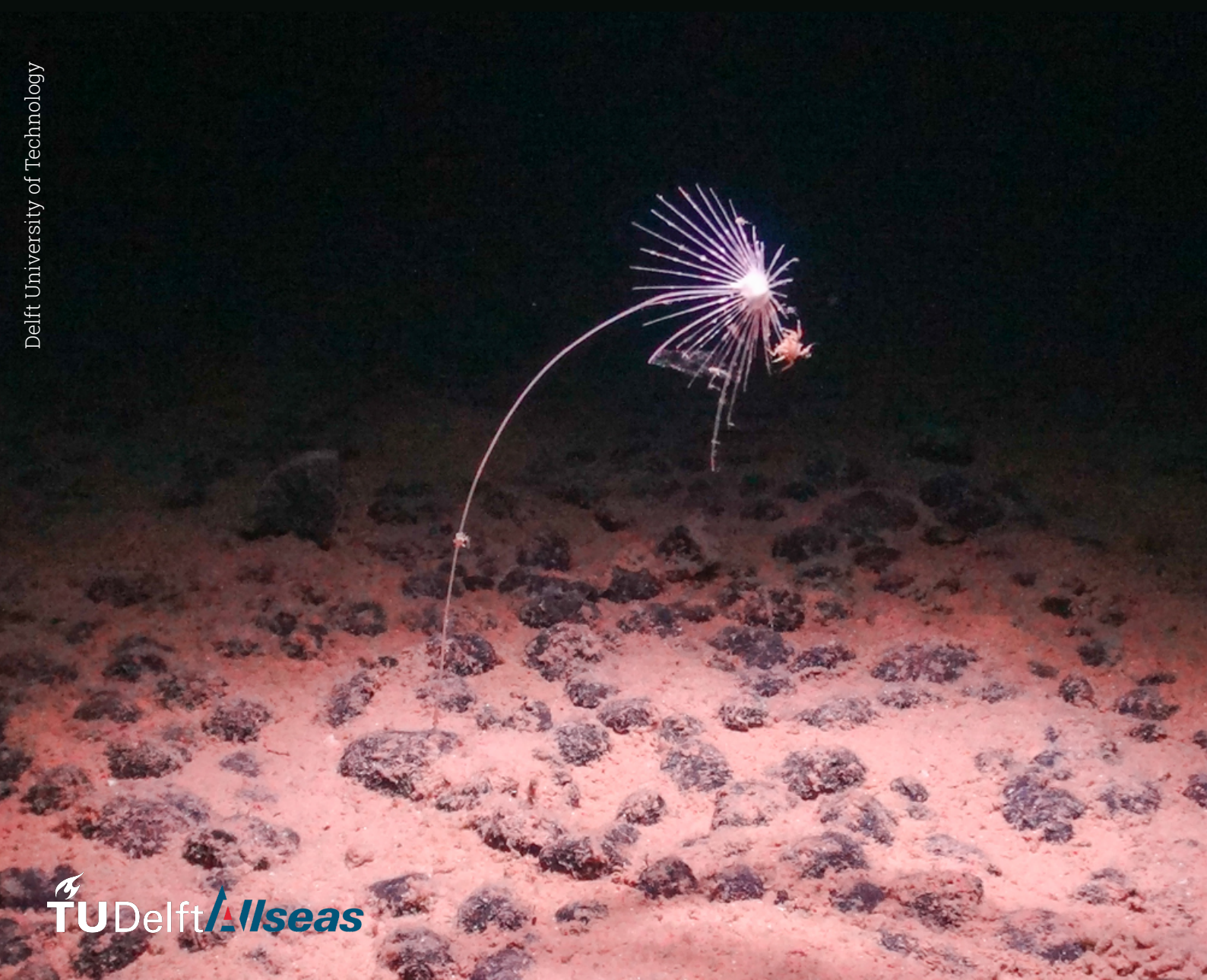

TU Delft Allseas

Measurement of low sediment concentrations in a pipe flow

A deep sea mining application

Sven Cornelis Theodorus Laken (5121817)

Chairman:	Dr.ir. R.L.J. Helmons
Committee:	Dr.ir. AM Talmon
Company supervisors:	Ir. F.A. Doorn
	Ir. F. van Grunsven
Department:	Maritime and transport technology, Delft

Cover: Polymetallic nodules, pictured here dotting the seabed under a carnivorous sponge, contain valuable metals that are in demand by the electric vehicle industry (Modified) [78]

TU Delft Allseas

Preface

The deep sea is a vast and mysterious realm, holding potential for humanity's exploration and resource extraction. Deep sea mining, in particular, offers the potential to access valuable minerals essential for technological advancement and economic growth. However, alongside this potential comes concerns about the environmental impact of such activities.

This thesis focuses on the relationship between deep sea mining and its potential harm to the environment, particularly regarding the disposal of sediments generated during mining. As our understanding of deep sea ecosystems grows, so does the urgency to develop responsible mining practices that minimize damage to marine habitats.

One issue is the lack of an efficient system to monitor sediment disposal. Without proper monitoring, it is hard to quantify the environmental pressure and take timely action to address it. Therefore, improving monitoring systems is crucial to prevent irreversible harm to deep sea ecosystems.

Despite these challenges, there's an opportunity for innovation and progress. By recognizing the shortcomings of current monitoring methods and working toward better solutions, we can ensure a less impactful approach to deep sea mining. This thesis aims to contribute to this effort by exploring ways to develop more effective monitoring strategies. We need to take proactive steps to protect the environment as this industry is developing. The aim is that this research will show people a step in the right direction for sediment disposal monitoring and environmental impact.

If you can not measure it, you can not improve it
-Lord Kelvin-

The completion of this thesis has been a challenging but rewarding journey, and I am grateful to everyone who supported me along the way.

First and foremost, I would like to express my gratitude to Rudy Helmons for his support during my research. His critical feedback and technical expertise were instrumental in addressing key challenges and ensuring the success of my work.

I am grateful to Allseas for their financial support, which made the construction of the test setup possible. This research would not have been feasible without their investment in its practical execution. I am equally appreciative of the continuous and adaptive feedback provided by my colleagues at Allseas, Floris Doorn and Frans van Grunsven. Their insights, collaboration, and constructive suggestions greatly enhanced the quality of my thesis.

I would also like to thank Arno Talmon for providing a second opinion at critical decision points during my research. His thoughtful perspectives and valuable feedback helped me navigate significant milestones with confidence.

Additionally, I extend my heartfelt thanks to the laboratory support team for their assistance during the testing phase of my thesis. While the process presented numerous challenges and unexpected hurdles, their unwavering support ensured we overcame these difficulties and achieved successful outcomes.

Sven Cornelis Theodorus Laken
Delft, February 2025

Abstract

This thesis explores the measurement of low sediment concentrations in pipeline flows, a critical issue in deep-sea mining. The study aims to identify and validate a continuous measurement method capable of accurately detecting suspended sediment concentrations between 10-75 g/L. These measurements are essential for minimizing the environmental impact of sediment plumes generated by mining operations.

The research begins with an analysis of material properties and flow dynamics, emphasizing the role of sediment particle size, and density in influencing suspension and settling behaviours. Highlighting the differences between concentration measurement and density measurement and the additional error involved. A review of flow regimes, turbulence, and their effects on sediment distribution within pipelines sets the foundation for understanding the complexities of representative sampling.

The thesis evaluates a range of measurement methodologies against criteria such as accuracy, range, spatial and temporal resolution, safety, cost, and impact on the flow. Optical, acoustic, conductivity, and radioactive source sensors were unsuitable due to limited range, low accuracy, or safety concerns. Promising alternatives include the U-loop, Coriolis, and vibrating fork sensors. The U-loop offers good accuracy and range, but causes significant pressure drops. Coriolis sensors provide excellent accuracy and broad range, but require careful sampling to ensure reliability. The vibrating fork sensor is simple and has a good range, but suffers from low accuracy and limited spatial resolution.

A key aspect of this research is the experimental setup, which integrates multiple sensor technologies in a controlled flow loop environment. Detailed methodologies for sensor calibration, installation, and data collection ensured the testing conditions. Tests are conducted under varying sediment concentrations, sediment types, grain sizes, and flow velocities to validate the accuracy and reliability of each measurement method.

The results reveal significant differences in sensor performance across test conditions. Test variables such as sediment type, concentration, and flow velocity are shown to influence sensor performance.

In conclusion, suspended sediment concentrations from 10 to 75 g/L can be measured accurately using a Coriolis sensor. This sensor directly measures density which can be converted into concentration with minimal calibration or correction, demonstrating superior accuracy and precision across diverse flow conditions. Although it reliably detects finer deep-sea sediment, minor challenges remain when measuring coarser materials, such as nodule fines. Overall, the findings contribute to the development of environmentally responsible deep-sea mining practices, by facilitating real-time and accurate sediment monitoring.

Contents

List of Figures

List of Tables

Nomenclature

Abbreviations

Abbreviation	Definition
ADV	Acoustic Doppler Velocimeter
ASTM	American Society for Testing and Materials
CCP	Conductivity Concentration Profiler
CCZ	Clarion Clipperton Zone
DAC	Data Acquisition Card
EIS	Environmental Impact Statement
EIT	Electrical Impedance Tomography
FL	Durand Froude Number
ISA	International Seabed Authority
NTU	Nephelometric Turbidity Units
OBS	Optical Backscatter Sensor
ppt	Parts per Thousand
SNR	Signal-to-Noise Ratio
SPM	Suspended Particulate Matter
SSC	Suspended Sediment Concentration
TDR	Time Domain Reflectometry
STD	Standard Deviation
R^2	Coefficient of determination (trendline precision)
rel. R^2	Relative coefficient of determination (accuracy to ideal line)
error	Error between measured and theoretical concentrations
rel. error	Relative error, error as a percentage of theoretical concentration
abs. rel. error	Absolute relative error as a percentage

Symbols

Symbol	Definition	Unit
A	Sensor's vibration amplitude	[m]
B	Vibrating densitometer calibration constant	[-]
c	Concentration of sediment	[g/L]
c_C	Coriolis concentration	[g/L]
c_F	Vibrating fork concentration	[g/L]
c_M	Manual sample concentration	[g/L]
c_s	Spring constant	[N/m]
C_T	Theoretical concentration	[g/L]
c_U	U-loop concentration	[g/L]
C_{vi}	In-situ concentration	[%]
d_p	Particle diameter	[m]
D	Pipe diameter	[m]
$DP1$	Differential pressure (Sensor 1)	[Pa]
$DP2$	Differential pressure (Sensor 2)	[Pa]

Symbol	Definition	Unit
f	Sensor's vibration frequency	[Hz]
$f_{Nyquist}$	Nyquist frequency	[Hz]
g	Gravitational constant	[m/s²]
h	Height between pressure sensors	[m]
ID	Inner Diameter (of a pipe)	[m]
k	Constant characteristics of the gauge	[-]
L	Characteristic length ($L = 2A$)	[m]
m	Total mass	[kg]
m_{add}	Added sediment mass per liter of water	[g/L]
M	Mass vibrating element	[kg]
N	Number of photons measured by the detector	[Bq]
No	Number of photons measured in pure water	[Bq]
P	Period	[Hz]
Q	Flow rate	[m³/s]
Re	Reynolds number	[-]
S_{mi}	Relative mixture density	[-]
S_s	Relative solids density	[-]
St	Stokes number	[-]
T	Water temperature	[°C]
τ_f	Fluid timescale	[s]
τ_p	Particle relaxation time	[s]
V	Volume of fluid oscillating	[m³]
V_s	Volume fraction of sediment	[-]
V_c	Volume fraction of clay	[-]
V_n	Volume fraction of nodules	[-]
V_w	Volume fraction of water	[-]
v	Flow velocity	[m/s]
v_{max}	Maximum velocity of the sensor's vibrations	[m/s]
w_0	Terminal settling velocity	[m/s]
w_s	Settling velocity with sediment concentration	[m/s]
Δ	Relative density, difference between sediment and water	[-]
Δ	Relative density, difference between sediment and water	[-]
Δp_{man}	Manometric pressure difference	[Pa]
Δz	Height difference	[m]
μ	Dynamic viscosity (assumed similar to water)	[Pa·s]
ν	Kinematic viscosity	[m²/s]
ρ_c	Clay grain density	[kg/m³]
ρ_m	Mixture density	[kg/m³]
ρ_n	Nodule grain density	[kg/m³]
ρ_p	Particle grain density	[kg/m³]
ρ_s	Sediment grain density	[kg/m³]
ρ_w	Water density	[kg/m³]
ε	Pipe roughness	[m]

1

Introduction

1.1. Green Transition and the Need for Metals

As the global population grows and living standards improve worldwide, the overall consumption of metals is expected to increase significantly. Since recycling rates for most metals remain low, this growing demand is predominantly met through the extraction of primary raw materials via mining. Additionally, the transition from fossil fuels to low-carbon alternatives further escalates the demand for rare earth metals, which are essential for manufacturing solar panels, electric motors, and batteries. With declining ore quality on land and an increasing number of natural areas being protected for environmental reasons, interest has shifted towards the deep sea as a potential source of natural resources.

Metals have been known to exist in the deep sea since the late 1800s, and their potential to serve as a supply source has been a topic of consideration ever since. These minerals, located in international waters, fall under the jurisdiction of the International Seabed Authority (ISA), which enforces the Convention on the Law of the Sea. By 2023, the ISA had signed 19 contracts for nodule exploration, primarily in the Clarion Clipperton Zone (CCZ), making exploitation mining activities increasingly likely [25].

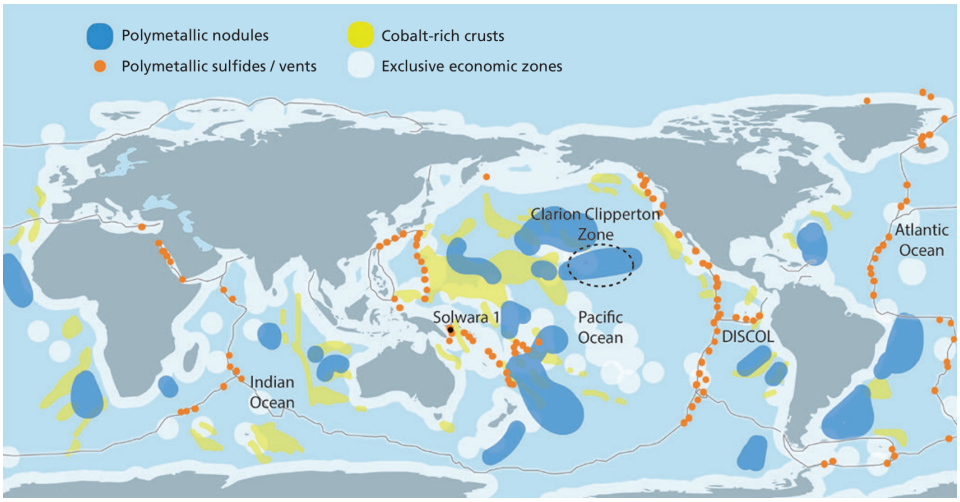

Figure 1.1: Deep sea mining world map [25].

Polymetallic nodules are currently the most advanced in terms of readiness for exploitation. These nodules, which resemble potatoes in shape and size, are located on the surface of the seafloor and distributed in a two-dimensional manner [24]. The CCZ contains an estimated 21 billion tons of polymetallic nodules, highlighting its significant potential. With an average abundance of 15 kg/m^2 and a maximum reaching 30 kg/m^2, the CCZ is the region with the highest-grade nodules. This area, nearly the size of the European Union, is situated in the central Pacific Ocean between Hawaii and Mexico,

see figure 1.1 [39]. In addition to manganese, the nodules contain substantial quantities of metals crucial for the green transition, such as nickel, copper, and cobalt [50]. The complete composition of analysed nodules is detailed in Table 1.1, but nodule composition greatly varies per field and also within fields.

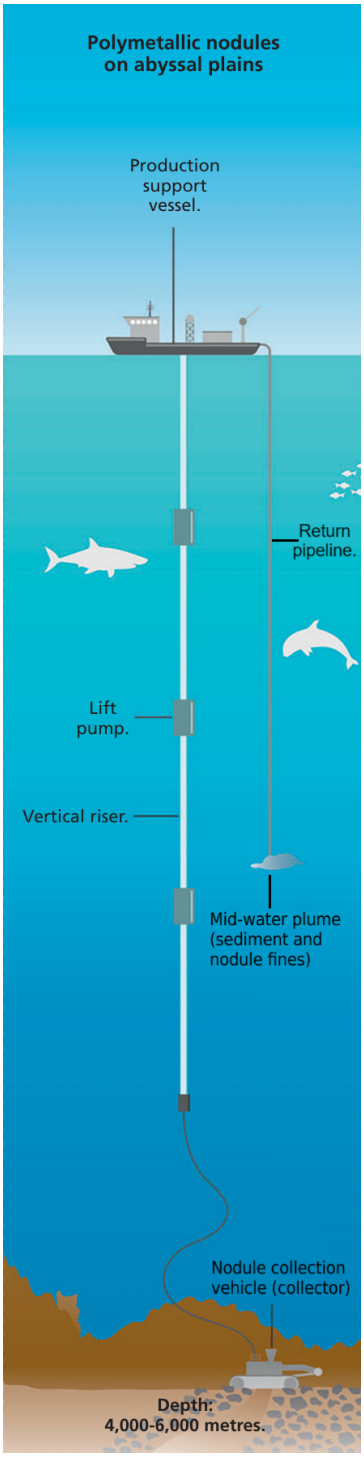

Figure 1.2: Deep sea nodule collection system [38].

Table 1.1: Chemical composition of polymetallic nodules [1].

Element	Composition (%)
Manganese (Mn)	29.4
Iron (Fe)	6
Nickel (Ni)	1.4
Copper (Cu)	1.3
Cobalt (Co)	0.25
Titanium (Ti)	0.2
Aluminium (Al)	3
Sodium (Na)	1.5
Silicon (Si)	5
Oxygen (O)	1.5
Hydrogen (H)	1.5
Calcium (Ca)	1.5
Magnesium (Mg)	0.5
Potassium (K)	0.5
Barium (Ba)	0.2

1.2. Nodule collection

The process of deep-sea nodule collection involves several stages, beginning with the use of a specialized nodule collection vehicle which traverses the seabed and collects nodules. These vehicles are equipped with harvesting tools, such as suction systems or mechanical arms, to gather nodules unavoidably with surrounding sediment. Nodules are often separated from most of the sediment in the nodule collection vehicle. Once collected, the nodules and sediment mixture is transported to the surface via a vertical riser system, which carries the material to a production support vessel. On board the vessel, the nodules are separated from the sediment and water, with the nodules stored for further processing. The sediment and water are then returned to the ocean through a return pipe at a specific depth below the photic zone to minimize environmental impact. This discharge depth is chosen to prevent direct interaction with surface ecosystems and to limit sediment plumes in biologically sensitive areas. Where the mixture re-enters the sea a mid-water plume is created [74].

1.3. Environmental Impact

The mining of polymetallic nodules will inevitably cause environmental stresses in the deep-sea environment, both within and around the mining areas. Environmental impacts include, but are not limited to: the mobilisation and compaction of seabed sediment, the removal of hard substrates essential for marine life, the displacement of fauna from the seafloor, and the deposition of suspended sediment in and around the mining zone. Sediment plumes are generated through the following activities:

- Tracks movement from the nodule collection vehicle
- The nodule collection system
- Discharge of residual sediment at the nodule collection vehicle (diffuser)
- Discharge of residual nodule fines and sediment from the vessel (mid-water plume)

Most suspended sediment is expected to settle near the mining area. However, sediment plumes in these regions may deposit sediment that buries much of the underlying marine life [39]. Further afield, spreading plumes may still contain enough sediment to obstruct the feeding and respiratory systems of filter-feeding organisms [23]. Depending on ocean currents, sediment plumes have the potential to spread up to 9 km [31].

Deep-sea organisms rely on micro-zooplankton and other organic matter descending from the sea surface, which forms a crucial food source when it settles on the seafloor. Sediment plumes may result in a layer of inorganic material covering this organic matter reducing the amount of organic matter available, disrupting the food supply for deep-sea ecosystems [25].

Currently, the tolerance levels of deep-sea fauna to suspended sediment remain unknown. It is therefore vital to predict the environmental effects of spreading plumes accurately. Moreover, a system capable of monitoring the amount of suspended sediment in real-time during mining operations is essential [39]. Measuring sediment concentrations is also critical for ensuring compliance with mining regulations.

1.4. Problem Statement

Extensive research has been conducted on environmental impacts, diffuser design, and plume dispersion. However, to effectively monitor environmental stresses and sediment plume dispersion, it is necessary to quantify the amount of sediment and nodule fines discharged into the ocean via the mid-water plume (discharge water).

The current method for monitoring sediment and nodule fines in the return flow involves sampling the pipeline and analysing the samples to determine concentration levels, further explained in section 3.1. While this approach provides accurate concentration values at specific moments, it involves multiple steps, increasing the likelihood of errors. Additionally, this method is not continuous, offering only discrete concentration values, which creates uncertainty about sediment levels between measurements.

This approach is also time-consuming, resulting in significant delays in obtaining test results. Consequently, there is limited opportunity to adapt processes to manage concentration levels. Furthermore, the methodology is labour-intensive, which is a disadvantage due to the high cost of offshore personnel. A continuous concentration measurement system would address these challenges by enabling real-time data logging, simplifying compliance with regulatory requirements, and reducing reliance on manual labour.

The suspended sediment concentration in the return flow is expected to range between 10-75 g/l. Existing suspended sediment concentration sensors are primarily designed for two applications:

1. Sediment transport in rivers and coastal areas for civil engineering purposes, where sediment concentrations are generally lower.
2. Sediment transport in pipelines for dredging operations, where sediment concentrations are significantly higher.

To measure concentrations in our specific application, a different measurement methodology must be found.

1.5. Research Questions

Main Research Question

How can sediment concentrations of 10–75 g/l, across a range of sediment types (7.2–150 µm), in pipe flow conditions be measured with the highest accuracy?

Sub-Questions

- What are the material properties of the sediment and the flow conditions for deep-sea mining operations?
- What are the existing concentration measurement methodologies, and what are their limitations?
  - What types of methodologies are available for measuring suspended sediment concentrations?
  - What is the achievable accuracy of each method under deep-sea mining flow and sediment conditions?
- How do sediment properties (e.g., size, adhesion, and cohesion) affect the performance of the concentration measurement methodologies?
- How do flow and mixture properties (e.g., velocity, concentration, temperature) influence the performance of the concentration measurement methodologies?
- Which concentration measurement methodologies are most robust to inaccuracies caused by changes in sediment, flow, and mixture properties?

2

Material properties and flow regime

This chapter outlines the key material properties and flow regime relevant to deep-sea mining return flows. It begins by defining and distinguishing between suspended particulate matter (SPM) and suspended sediment concentration (SSC), and explains how these affect the slurry density. Then covering the physical characteristics of the solids and their influence on flow behaviour in pipelines. Fundamental calculations, such as the Reynolds and the deposited limit velocity.

2.1. Concentration and mixture density

SPM includes all suspended particles, both mineral and biological [10], whereas SSC refers solely to suspended sediment [58]. This thesis assumes biological components are negligible, thus using SSC which will be referred to as concentration.

Density is always expressed in kg/m^3 and applies to solids, liquids, and mixtures. In contrast, concentration pertains to the mixture and is expressed in g/L, representing mass concentration. The concentration in return flows from deep-sea mining vessels has been reported as 21.3 g/L in a collector test [63], 25–75 g/L in NORI-D scenarios [43], and 10–50 g/L in pilot tests by The Metals Company and Allseas [34]. This thesis assumes an SSC range of 10–75 g/L.

Return flows contain both clay and nodule fines. Nodule fines persist due to incomplete separation and degradation during the airlift process. A dewatering plant with 98% efficiency leaves 2% of nodules in the return flow [63], resulting in a 50/50 clay-nodule mixture [34]. Polymetallic manganese nodules have a mean grain density of 3460 kg/m^3 [24], while siliceous clay-ooze sediment in the CCZ has a grain density of 2500 kg/m^3 [65, 57, 43]. When converting the suspended sediment concentration to a density, the following formula are used:

$$V_c = \frac{SSC}{2 * \rho_c}, \quad V_n = \frac{SSC}{2 * \rho_n}, \quad V_w = 1 - V_c - V_n \tag{2.1}$$

$$\rho_m = V_c\rho_c + V_n\rho_n + V_w\rho_w \tag{2.2}$$

Where:

- V_c (-): Volume fraction of clay.
- V_n (-): Volume fraction of nodule fines.
- V_w (-): Volume fraction of water.
- SSC (g/L): Suspended solids concentration.
- ρ_c = 2500 (kg/m^3): Density of clay.
- ρ_m (kg/m^3): Density of the mixture.
- ρ_n = 3460 (kg/m^3): Density of nodules.
- ρ_w = 1025 (kg/m^3): Density of nodules.

Table 2.1: SSC and corresponding mixture density

Parameter			Difference
SSC (g/L)	10	75	65
ρ_w (kg/m³)	1031.55	1074.11	42.56

As shown in Table 2.1, the SSC difference exceeds that of ρ_m, reducing density sensor accuracy for SSC measurements. Dividing the SSC difference by the density difference gives a correction factor of 1.53, meaning a 53% increase in error when converting to SSC.

2.2. Grain Size

Clay grain size varies by location. Jones [46] reported 58–68% of clay (0–5 cm depth) is smaller than 7.8 µm, with 28–39% between 7.8–63 µm. The EIS [43] gives an average clay particle size of 11$\pm$3 µm, without a full distribution. Fugro's study [63] shows 13–88% of clay is smaller than 2 µm, 73–99% smaller than 32 µm, and 100% smaller than 250 µm. Abram [40] found 88.6% of eastern CCZ clay is under 4 µm. A clay grain size range of 1–75 µm is assumed for this thesis.

Nodule fines from pilot tests have a grain size of $\leq$1000 µm. Industrial operations aim to separate nodules down to 150 µm, reducing fines in the return flow [34].

2.3. Flow Properties

The collector test discharge volume flow was 353 m³/h at 3.9 m/s [63]. In slurries, solids settle under gravity, creating concentration gradients in horizontal pipes. Higher flow velocity increases turbulence, reducing sediment settling. Particle size and density influence flow regime; larger and denser particles require more turbulence to remain suspended. Four flow regimes are possible: sliding bed, saltation, heterogeneous suspension, and homogeneous suspension (Figure 2.1) [48]. To calculate the Reynolds number for flow in a pipe, the following formula is used:

$$Re = \frac{vD}{\nu} \tag{2.3}$$

Where:

- Re is the Reynolds number.
- $v = 3.9m/s$ is the flow velocity.
- $D = 0.2m$ is the pipe diameter.
- $\nu = 1.41 \cdot 10^{-6} m^2/s$ is the kinematic viscosity of the fluid ([89], the water temperature in the return flow is 7.5°C[63]).

Which gives a Reynolds number of around $4.4 \cdot 10^5$, which means it is turbulent flow [37]. The flow also contains relatively small particles from 1-150 µm, which means the flow will probably be a homogeneous suspension.

The concentration in vertical pipes differs from horizontal pipes due to the settling velocity of solids, which aligns or opposes the flow. This results in higher concentrations in upward flows and lower concentrations in downward flows [48, 90]. Methods without full spatial resolution must ensure sampling locations are representative of the entire flow.

The Durand Froude number, a dimensionless parameter, determines the critical velocity needed to keep solids in suspension. To calculate the deposit limit velocity in a horizontal pipe, slurry properties prone to stratification are used. Graf and Robinson noted that curves for uniform sands (Figure 2.2) are overestimated, while those for non-uniform sands are more accurate [59, 32].
Properties:

- $C_{vt} = 15\%$ (volumetric transport)
- $d = 200\mu m$ (particle size diameter)

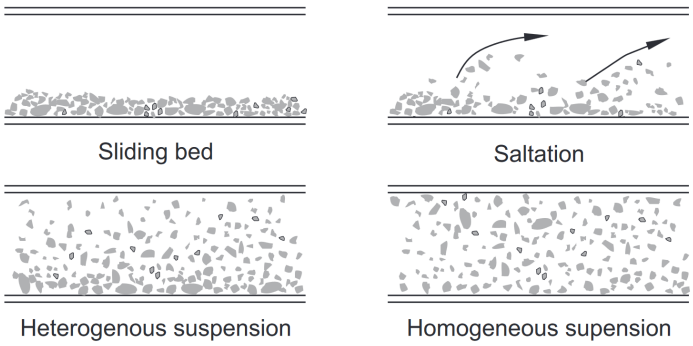

Figure 2.1: The four regimes of flow for settling slurries in horizontal pipelines [48].

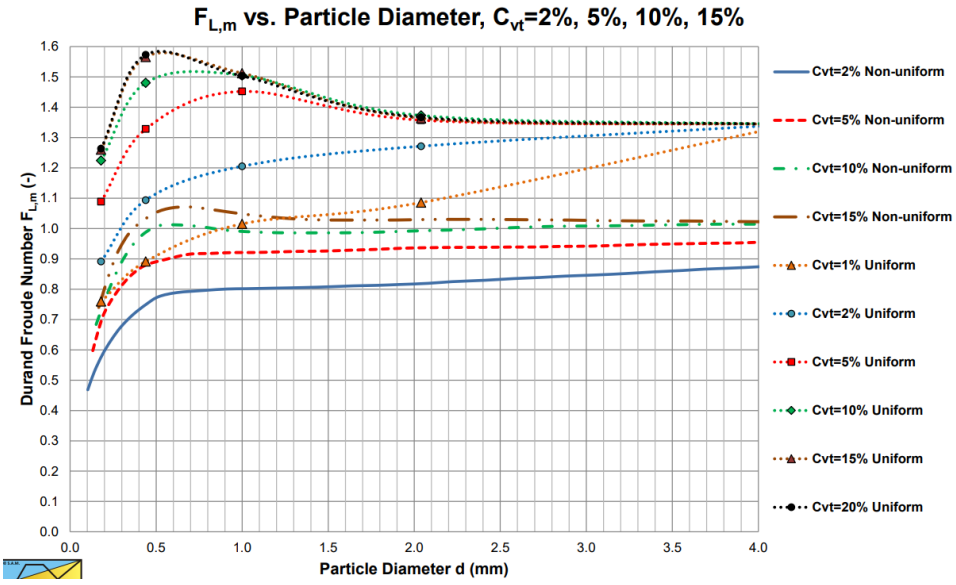

Figure 2.2: The Durand & Condolios F_L curves[59]

The Durand Froude number formula can be rewritten in the following form to determine the deposit limit velocity.

$$v_{ldv} = F_L \cdot \sqrt{2 \cdot g \cdot R_{sd} \cdot D_p} \tag{2.4}$$

Where:

- $F_L = 0.8\,(-)$ is the Durant Froude number, a dimensionless number used to characterize the flow.
- $v_{ldv}\,(m/s)$ is the critical velocity of the slurry flow required to keep the particles in suspension.
- $g = 9.81 m/s^2$ is the acceleration due to gravity.
- $R_{sd}\,(-)$ is the relative density of the solid particles, defined as follows:

$$R_{sd} = \frac{\rho_s - \rho_1}{\rho_1} \tag{2.5}$$

- $\rho_s = 2650 kg/m$ density of the test sediment.
- ρ_w = 998.21 kg/m³ (at 20 °C, [6]): Density of water.

This calculation gives a value of $v_{ldv} = 0.93 m/s$, which is not close to the 2 m/s which will be the lowest operating speed of the test setup for this thesis. The operating speed is higher than the deposited limit velocity such that the flow regime is probably going to be a homogeneous suspension.

3

Measurement methodologies

In this chapter different measurement technologies are evaluated on how suited the methodologies are for the application of this thesis. That is why all methodologies are rated for different criteria to better compare them to each other. The criteria are:

- **Accuracy**, in how many digits g/L can be determined the concentration level in the flow. The accuracy is stated as one standard deviation.
- **Operating range**, what is the range the methodology is able to measure concentration and how well does it fit the application range of this thesis? The operating range should be from 10-75 g/L in suspended sediment concentration. A greater operating range from 5-100 g/L would be desirable, so it would be possible to also detect outliers of concentration.
- **Temporal resolution**, this tells how often a measurement is being taken also called the sampling frequency. The aim for temporal resolution is 1 Hz, but higher sampling frequencies are appreciated.
- **Spatial resolution**, how large is the volume being measured, is it only a small volume or is the whole flow tested? Suspended sediment concentration throughout the flow could differ. Depending on the flow conditions, a small sample could be representative of the full flow, but taking the measurement from a small volume and extrapolating it to the full flow always brings inaccuracies. This makes methodologies that measure a larger volume more desirable.
- **Pressure drop/interference with the flow**, how much does the measurement methodology affect the flow? For example, does it result in a pressure drop? When a pressure drop becomes high, more pumping power needs to be installed which will result in more energy consumption, this will increase operation costs for the sensor especially because it is at a location where energy is scares. This makes methodologies that do not affect the flow more desirable.
- **Safety**, safety is a fundamental requirement, so it might seem like an unusual criterion. However, in this context, safety refers not to how inherently safe the item is, but to how easy it is to use safely.
- **Cost**, this consists of the purchasing and the operating costs, both are hard to find but an estimation will be made about the two costs.

3.1. Manual sampling

Manual sampling is one of the most basic techniques to measure SSC concentration, but getting a representative sample is to the contrary often a challenge. There are two types of manual sampling, trap-type and pump-type sampling. Manual sampling is often regarded as giving a highly accurate measurement of SSC and it is commonly regarded as a benchmark for other measurement devices. While this is true when performed properly, the potential of producing highly inaccurate measurements does exist. In this section, elaboration on these errors and how to prevent them from occurring [20].

Concentration

Comparing the results of 9 different laboratories using the ASTM method D3977-97 B, shown in table 3.1. It shows that concentration measurement by using a filtration method shows a high sensitivity for concentration, resulting in relatively large errors for low concentrations [20].

Table 3.1: Precision and bias for ASTM method D3977-97 B, [3].

Concentration Added, mg/L	Concentration Recovered, mg/L	Standard Deviation of Test Method (St)	Standard Deviation of Single Operator (So)	Bias, %
10	8	2.6	2	-20
100	91	5.3	5.1	-9
1000	961	20.4	14.1	-3.9

Drying Temperature

One of the parameters in which methodologies vary from each other is the temperature at which drying takes place. Both the ASTM and APHA methods use a drying temperature of 103-105 °C for the sampled material. However there are several methodologies which suggest that a drying temperature below 100°C would be better [86].

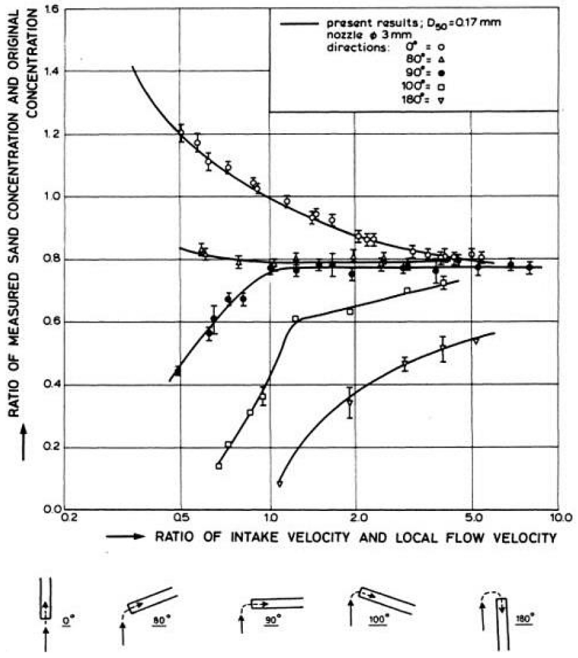

Figure 3.1: Effect of flow rate and intake orientation on sampling accuracy [9].

Sampling

The representativeness of a sample depends on the orientation of the intake nozzle and the flow velocity within the sampling hose [20]. Misalignment with the ambient flow direction or mismatched velocities between the sampling and ambient flow can introduce concentration errors. Lower sampling velocities result in a higher sampled concentration compared to the ambient concentration, while a higher sampling velocity leads to a lower sampled concentration. As the mass of the particle increases, with a corresponding increase in diameter and density, the concentration error also increases [87].

Isokinetic sampling is employed to minimise such errors. This method ensures that the fluid velocity entering the sampling nozzle matches the ambient flow velocity, allowing the sampled sediment concentration (SSC) to accurately reflect the ambient SSC. Proper alignment of the sampling nozzle with the flow direction and adherence to isokinetic conditions are essential for representative sampling [9].

3.2. Optical Sensor

Optical sensors consist of a light source and a detector. Turbidity is determined by the scattering and transmission of light by suspended sediment, which is detected and converted into Nephelometric Turbidity Units (NTU). NTU values can be calibrated to estimate suspended sediment concentration (SSC), but calibration is required for specific materials and particle sizes [22]. Turbidity measures the cloudiness of a mixture, ranging from 0 NTU (distilled water) to 4000-5000 NTU (high turbidity). Beyond 5000 NTU, sensors saturate and fail to detect higher SSC [84].

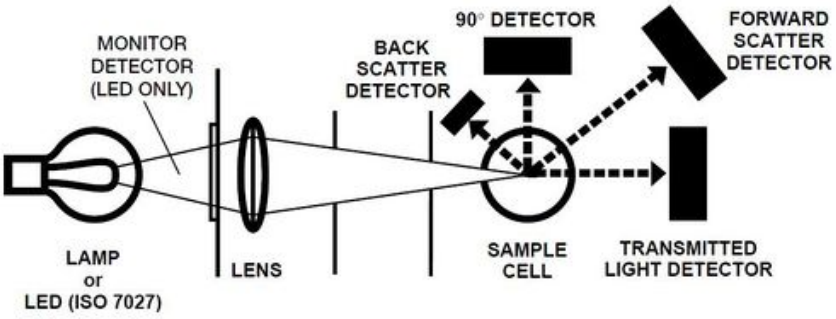

Figure 3.2: Optical sensor [30].

There are two types of optical sensors: nephelometric sensors (OBS) and absorption sensors. OBS sensors detect scattered light and are suited for higher concentrations, while absorption sensors measure transmitted light. OBS sensors are more common, and this study focuses on them [68].

Working Range and Accuracy

A turbidity of 3000 NTU corresponds to approximately 3 g/L SSC, though values depend on sediment properties. Specialised sensors can measure up to 30,000 NTU with a relative error of around 2% [84]. OBS sensors are linear up to about 10 g/L; beyond this, readings become nonlinear (saturation) [10].

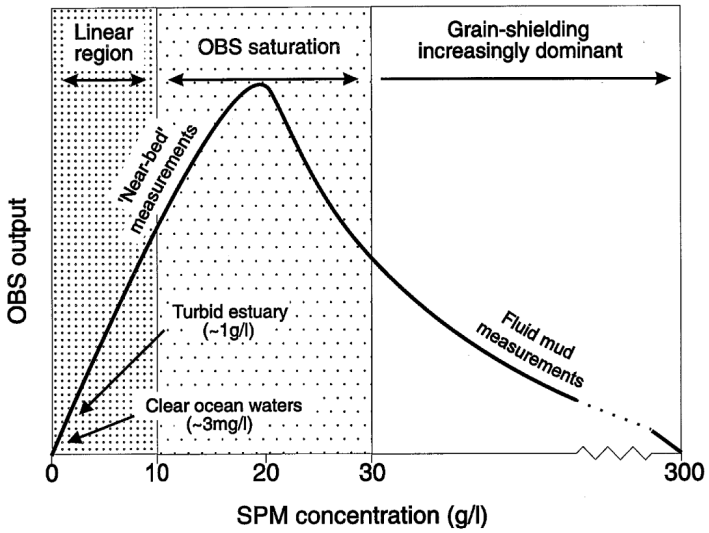

Figure 3.3: OBS output at different concentrations [10].

OBS sensors use infrared light to minimise ambient light interference, but work best in dark conditions. They are relatively insensitive to temperature changes ($< 0.05\% \, ^\circ\mathrm{C}^{-1}$) but can be affected by marine growth on lenses and bubbles, which scatter light similarly to sediment [22, 33].

These sensors are more sensitive to fine particles like clay than coarser sediment, as larger particles scatter less light due to a smaller surface area-to-mass ratio [29]. Clay-rich sediments may form flocs, altering particle size distributions and affecting measurements [10].

The OBS-5 sensor extends traditional OBS ranges with a 3 mW laser diode, dual detectors, and a microcontroller, measuring up to 50 g/L for mud and 500 g/L for sand. However, it is discontinued, likely due to performance issues [22, 11].

Temporal resolution
Optical sensors have a great temporal resolution, every second there is a reading from the sensor, thus 1 Hz [28].

Spatial resolution
One of the drawbacks of optical sensors is that they have poor spatial resolution. The size that is being sampled is around 3 cm^3 and is located next to the sensor [10].

Pressure drop
The pressure drop of an OBS sensor is measurable because the sensor itself is located in the flow. The flow is influenced by the sensor located in the flow.

Safety
There is little risk with this sensor and no special training is needed to work safely with this type of sensor.

Cost
The cost of a commercial OBS sensor is around 1000-3000 dollars [26]. With operating cost afterwards being low [58].

3.3. Acoustic
Acoustic sensors use high-frequency sound waves, typically in the megahertz range, to measure sediment concentration. A transducer emits sound waves, which interact with suspended sediment. The backscattered sound, received by the transducer, is converted into an electronic signal. The amplitude of this backscatter provides information about concentration. If particle size is known, SSC can be estimated over the propagation range [28].

Figure 3.4: Acoustic backscatter sensor [42].

Working Range and Accuracy
The working range of a single-frequency acoustic backscatter sensor (ABS) depends on signal amplitude and frequency, typically 1 MHz. ABS sensors have an accuracy of 20%, resulting in an error of 2-15 g/L [82]. The Rayleigh scattering model, valid when the wavelength is smaller than particle circumference, is often used. Calibration involves measuring a known sample while operating the sensor. A limitation arises when changes in particle size distribution affect backscatter signals, leading to errors. ABS sensors typically operate within 0.1-20 g/L [81].

Acoustic Doppler velocimeters (ADV) can also measure concentrations, tested in the range of 0.01-50 g/L. Signal-to-noise ratio (SNR) is used to estimate concentration by subtracting background noise. SNR behaviour divides into three regions: a linear zone up to 1 g/L, where SNR correlates with concentration; a muffling zone (1-20 g/L), where SNR changes are minimal, making concentration determination difficult; and a saturation zone, unsuitable for precise measurements [13].

Temporal resolution
The acoustic sensors have a high temporary resolution, with sampling rates up to several readings per second [28]. The sampling frequency can go up to 25 Hz [13].

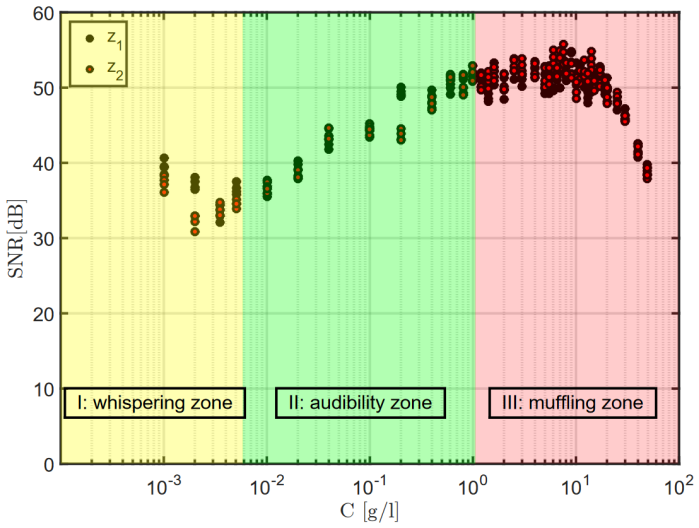

Figure 3.5: SNR results [13].

Spatial resolution

The acoustic backscatter sensor provides high spatial resolution, covering the full flow. It determines concentration at different depths by calculating the time for the signal to return using the speed of sound, offering a spatial concentration profile across the pipeline [28].

ADV sensors measure a smaller volume of approximately 0.4 cm^3, in a cylindrical sampling area 6 mm in diameter and 3-15 mm in depth, located 0.05 m below the sound emitter.

Pressure

These sensors are not located in the flow and the flow is not diverted for measurement. The flow is not affected so there are no pressure drops because of the sensor.

Safety

The sensor does not come with specific safety risks, and no safety training is needed.

Cost

ADV sensors can be found secondhand online for around 2500 dollars, assuming secondhand would be half the price of a new one, a new ADV sensor amounts to 5000 dollars [73].

3.4. Conductivity

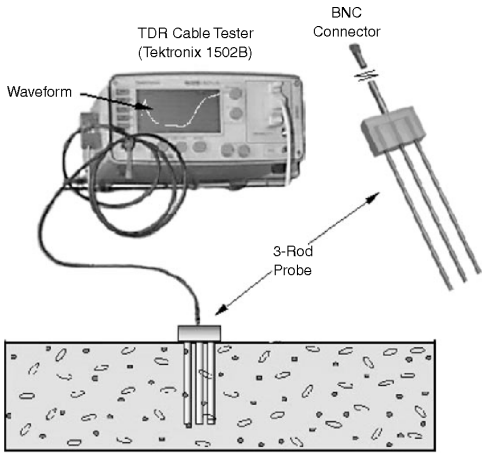

Figure 3.6: Time domain reflectometry sensor [47]

The electrical conductivity of water depends on its electrolytic constituents and temperature. Adding sediment, which has different conductivity, alters the mixture's conductivity. If salinity and temperature remain constant, conductivity becomes a function of sediment concentration [70]. Seawater has higher conductivity than tap water, which must be considered when measuring suspended sediment.

As shown in Figure 3.6, the sensor uses parallel plates to measure conductivity via an electrical resistance meter. This method determines sediment concentration. Advanced configurations include time domain reflectometry (TDR) [14], conductivity concentration profiler (CCP) [54], and electrical impedance tomography (EIT) [79].

Working Range and Accuracy

Conductivity sensors are influenced by concentration, temperature, and salinity, so these variables must remain constant [70]. This thesis focuses on TDR due to its alignment with the study's requirements.

- **CCP:** Operational range is 100–1161 g/L, which is outside the scope of this thesis [54].
- **EIT:** Operates within 10–400 g/L, making it suitable for this study [79].
- **TDR:** Theoretical range is 2–300 g/L, with an accuracy of $\pm$2 g/L. However, below 3 g/L, readings fluctuate, making it more suitable for high concentrations [14, 8].

Temporal resolution

The sampling rate is at least 4 GHz for a TDR, which makes it more than sufficient [92].

Spatial resolution

Depending on the size of the probes the volume being sampled is different but will be around 1000 cm³ for TDR [14].

Pressure drop

The TDR need to be present in the flow. This means the flow will be hindered a bit, thus resulting in some pressure drop.

Safety

If the voltage of the system is high there could be a danger of electrocution, but the voltage used is 1 V [54]. This means there are no significant safety risks present for the conductive sensor.

Cost

TDR sensor purchase prices range from 4500 to 6500 dollars.

3.5. Radioactive source

Radioactive source sensors use radiation to measure mixture concentration. High-energy photons from a radioactive source or X-ray machine determine slurry flow density. The principle is the same regardless of photon source: attenuation is measured between the source and detector (Figure 3.7). Collimators shape the beam and shield radiation. Attenuation depends on photon energy, sediment properties, and mixture density. Gamma rays have higher energy, while X-rays require low-density pipe materials like titanium for transmission [83].

Calibration involves measuring photon counts in clear water. The relation between transmitted and received photons is expressed as [28]:

$$N/No = (k * \rho_m)^n * exp(-k * \rho_m) \tag{3.1}$$

Working Range and Accuracy

Sensitivity increases with lower radiation energy but depends on sediment properties. Sensors must be calibrated for specific sediment types. Gamma-ray densitometers operate from 1010 to 1500 g/L, with an accuracy of 5 g/L [83]. X-ray sensors operate from 1000.25 to 1250 g/L, with an accuracy of 1% (around 10 g/L) [7, 76].

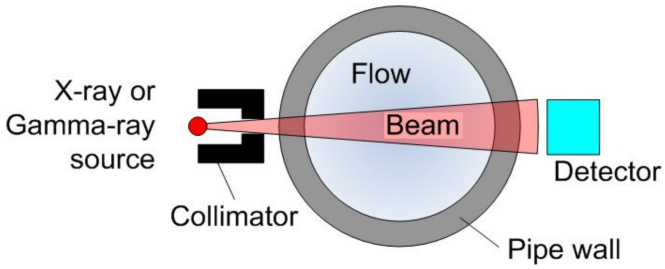

Figure 3.7: Gamma and X-ray sensor [83].

Temporal Resolution
The temporal resolution is relatively low, a ^{137}Cs source has a measurement frequency of 10 seconds, which means 0.1 Hz. But in practice, the measurement frequency could be changed from 1 to 0.001 Hz [28].

Spatial Resolution
Gamma-ray sensors measure a volume of 700 cm^3 (beam: 70 cm length, 10 cm diameter). X-ray sensors measure around 175 cm^3 (beam: 5–50 cm length, 1–5 cm diameter) [28].

Pressure Drop
Radioactive source sensors are external, causing minimal pressure loss.

Safety
Safety is critical due to radioactive emissions. Operators require special training, and regulations vary across countries. Gamma-ray sources emit continuously, posing hazards during storage, transport, and use. In contrast, X-ray sensors emit only when active, reducing safety concerns when turned off.

Cost
A radiation density sensor cost for a 6 inch pipe is 7000-8000 dollars. For a 20 inch pipe a sensor costs 12000-14000 dollars [55].

3.6. U Loop
A U-loop utilises an inverted U-shaped pipe to divert flow, as shown in Figure 3.8a. The sediment concentration differs between the upward and downward pipes due to settling velocity. Settling velocities for different sediment types are calculated in Appendix G. These settling velocities are significantly small, that the mean velocity and wall shear stress in both pipes remain similar.

Pressure differences in the vertical sections are measured by differential pressure transducers, recording manometric pressure. The hydrostatic pressure depends on the mixture density, which is influenced by concentration [90].

$$C_{\mathrm{vi}} = \frac{\Delta p_{12,\,\mathrm{man}} + \Delta p_{43,\,\mathrm{man}}}{2\left(S_{\mathrm{s}} - S_{\mathrm{f}}\right)\rho_{\mathrm{w}} g \Delta z} \tag{3.2}$$

While C_{vi} is close to the delivered volumetric solids concentration, they are not identical, but the difference is negligible in most cases. The mixture density S_{mi} can be calculated as [90]:

$$S_{\mathrm{mi}} = \frac{\Delta p_{12,\,\mathrm{man}} + \Delta p_{43,\,\mathrm{man}}}{2\rho_{\mathrm{w}} g \Delta z} + S_{\mathrm{f}} \tag{3.3}$$

Working Range and Accuracy
The U loop's accuracy depends on the pressure sensors used. A Rosemount 1151DP-4 S22 Pressure Transmitter has an operational range of 0–25/370 mbar and a stability of 0.1% [77]. Using Equation 3.3, the accuracy is 0.084 g/L for 25 mbar and 1.26 g/L for 370 mbar. The density range is 1025–1083 g/L for 25 mbar and 1025–2227 g/L for 370 mbar.

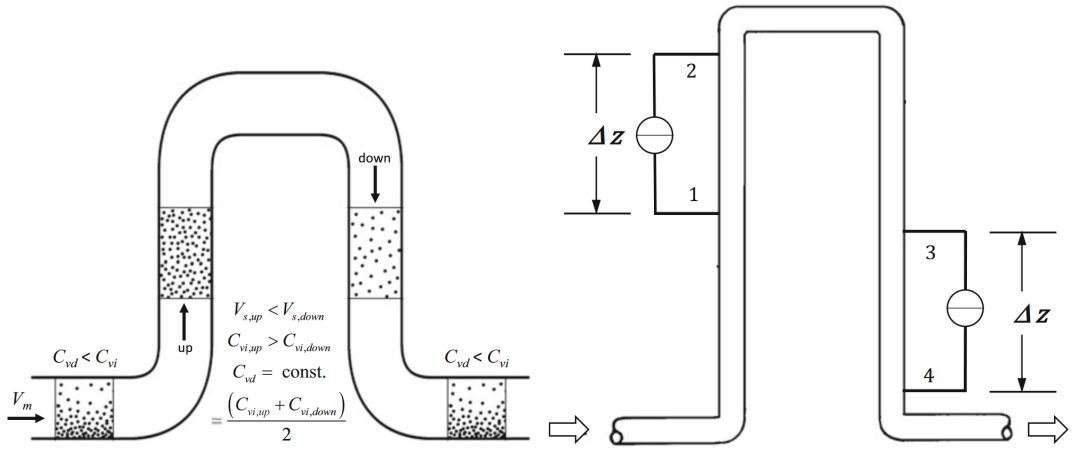

(a) Flow in U loop. **(b)** U loop pressure sensor locations.

Figure 3.8: U loop design [90].

Turbulence causes unequal pressure distributions, increasing error. Studies suggest 1% accuracy for pressure sensors is realistic, resulting in 0.84–12.6 g/L [35]. Other research reports standard deviations of 1.5% (15–16 g/L) [36], while concentration accuracy of 0.5% corresponds to 0.050–0.375 g/L [49]. Errors increase with particle size and density but decrease with higher concentrations [15].

U-loop meters require frequent cleaning due to settling and are mainly used in laboratories. This thesis assumes an accuracy of 1% for further calculations.

Temporal resolution
Most pressure sensors used for this purpose have a logging rate of around 4 Hz.

Spatial resolution
The spatial resolution of this kind of sensor is great because the full diameter of the pipe is being measured.

Pressure drop
The flow needs to be differed through this U shaped tube, resulting in significant pressure drops added to the flow. The size of the pressure drop depends mostly on the velocity of the flow, the height of the U loop and the radius of the corners.

Safety
The U loop is a high structure that could take quite some force on the sea so it needs to be properly supported.

Cost
The main cost of the U loop consists of the two pressure sensors. A Rosemount pressure transmitter will cost 2000-4000 dollars [45]. This means the test setup will cost 4000-8000 dollars.

3.7. Coriolis
Coriolis meters measure mass flow and density by vibrating a curved tube through which the mixture flows. The natural frequency of the tube depends on its stiffness and the fluid mass. As the tube's volume is constant, changes in frequency directly correlate with changes in fluid density [64]. Typical operating frequencies range from 50–1000 Hz, depending on tube geometry [41]. Temperature affects the tube's stiffness, altering the natural frequency, so most meters include a temperature sensor for compensation [64]. (Vibrating U-tube sensors operate on a similar principle, using a U-shaped tube [55].)

Working Range and Accuracy
Coriolis meters have a wide operating range, measuring fluid densities from 300 to 2000 g/L [19]. Their accuracy is typically 0.10% (1 g/L), with newer models achieving up to 0.2 g/L [64]. (Vibrating U-tube

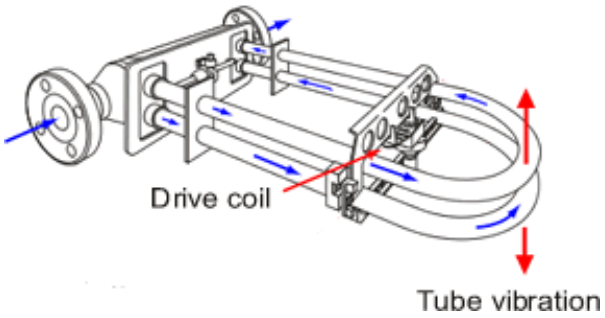

Figure 3.9: Coriolis sensor [85].

sensors have accuracy ranging from 5 g/L to 0.05 g/L [55].)

Temperature and pressure affect tube elasticity, influencing density measurements. Higher temperatures reduce tube stiffness [12, 66]. Sediment settling in downward bends can cause inaccurate density readings due to higher sediment density. This issue can be minimised by avoiding flat sections and sharp bends [94].

Temporal resolution
The temporal resolution is good for the sensor, it is around 170 Hz [41].

Spatial resolution
The spatial resolution depends on the measurement method. A large Coriolis meter measuring the full flow provides complete spatial resolution [56]. With a smaller Coriolis meter, only a sample flow passes through the sensor, making the spatial resolution dependent on the representativeness of the sampled fluid.

Pressure drop
The pressure drop varies with the measurement method. A large Coriolis meter handling the full flow causes a significant pressure drop, while a smaller meter sampling the flow results in a relatively small pressure drop.

Safety
There are no significant safety risks present for coriolis sensors, or special safety training is needed.

Cost
It is found that a coriolis sensor will cost around 7000-10000 dollars to purchases and install. After installing, sensor maintenance will cost around a 100 dollars a year (over 10 years) [64].

3.8. Vibrating Fork
The vibrating fork densitometer operates like a tuning fork immersed in a liquid. Piezo-ceramic elements and a feedback amplifier drive its oscillation. The fork's natural frequency depends on the liquid's density and viscosity. For Newtonian fluids influence of viscosity is compensated by measuring both the natural frequency and the damping effect. Temperature effects are also accounted for, as higher temperatures reduce the fork's stiffness and lower its oscillating frequency [55].

Working Range and Accuracy
Abrasion from solid particles in slurries is the main challenge for vibrating fork sensors, as it alters the fork's mass and frequency. Fine particles and low concentrations reduce abrasion [88]. The measurement range is 0–3000 g/L with an accuracy of 1 g/L [60].

Temporal resolution
The vibrating frequency in a liquid has shown to be around 975 Hz, but will widely vary with design parameters like length, width, thickness and material properties of the vibrating fork [93]. The sampling frequency is typically around 2 Hz, which is sufficient for the application of this thesis [21].

Figure 3.10: Vibrating fork densitometer, drawing [4].

Spatial resolution
Assuming that the volume of liquid being moved by the tuning fork is similar to that of the fork itself, the spatial resolution of the sensor would be around 2 cm³ [93].

Pressure drop
Because the vibrating fork needs to be present in the flow there will be interaction with the flow, but the pressure drop will be small.

Safety
There are no significant safety concerns for vibrating fork sensors.

Cost
It is found that a vibrating fork sensor will cost around 3000-10000 dollars to purchase depending on the accuracy [4][44].

3.9. Comparing the different sensing methodologies
In this section, the different methodologies will be discussed and the pros and cons will be compared, eventually leading to a conclusion about which sensor would be best suited for the application of this thesis. There is a table to better compare the different methodologies with each other, see table 3.2. The accuracy indicated in the table is the accuracy in concentration, meaning the density measurements are already converted to concentration by multiplying with the correction factor, calculated in subsection 2.1.

Table 3.2: Comparison of the different methodologies for concentration measurement.

Concentration measurement	Concentration accuracy	operating range	temporal resolution	spatial resolution	pressure drop	safety risk	cost ($)
Optical	2%->0.2-1.5 g/L	<3 g/L	1 Hz	3 cm³	medium	low	1000-3000
Acoustic	20%->2-15 g/L	0.1-20 g/L	25 Hz	full pipe	small	low	5000
Conductivity (TDR)	2 g/L	2 - 300 g/L	8 GHz	1000 cm³	small	low	4500-6500
Density measurement							
Radioactive source	10 g/L	1010 - 1500 kg/m³	0.1 Hz	700 cm³	small	high	7000-14000
U loop	1% ->1.7 g/L	1025 - 1083 kg/m³	4 Hz	full pipe	large	low	4000-8000
Coriolis and vibration U tube	2.1 to 0.1 g/L	300-2000 kg/m³	170 Hz	sampled volume	medium	low	7000-10000
Vibrating fork	2.1 g/L	0 - 3000 kg/m³	2 Hz	2 cm³	medium	low	3000-10000

3.9.1. Denied sensors

Optical

A optical sensor stands out for its impressive accuracy. However accuracy can be influenced by changing particle sizes, although this is not problematic when the particle size remains constant. Its performance is limited by its operating range, which does not cover the application range required for this thesis. While controlled dilution could bring the sample within range, it introduces additional inaccuracies. Furthermore, the sensor lacks spatial resolution.

Acoustic

The acoustic sensor is not applicable due to its low accuracy, susceptibility to variations in particle size, and limited operating range. The low accuracy of the sensor makes the data unreliable to use. The error that is possible to be produced by the variation in particle size adds to this unreliability. Lastly, its range is not sufficient for the specific application requirements.

Conductivity

The conductivity sensor is lacking in the accuracy department. The sensor does not possess the accuracy needed for the application of the thesis, it is important to use a sensor that can provide more accurate readings.

Radioactive source

The radioactive source sensor is not suitable for a few key reasons. Firstly, the accuracy of the sensor is lacking for the application of this thesis. Secondly, using a radioactive source sensor involves handling radiation, which poses a significant safety risk. This necessitates extensive safety protocols, specific safety training for personnel, leading to increased paperwork and additional personnel costs.

3.9.2. Approved sensors

U loop

The U loop presents itself as a good option for the specific application of the thesis due to its sufficient accuracy and operating range, which are the most important criteria. Its ability to provide precise readings across varying concentration levels is highly valued. Despite these advantages, a notable drawback is the substantial pressure drops associated with its operation.

Coriolis

The coriolis sensor is well-suited for the application of the thesis, primarily due to its exceptional accuracy and broad operating range, allowing for precise measurements across a wide range of concentrations. However, one significant concern is ensuring representative sampling, as it directly affects the measurement accuracy of the sensor.

Vibrating fork

The applicability of the vibrating fork is subject to debate due to several factors. While it offers a good operating range and simplicity in its design, concerns arise regarding its accuracy and spatial resolution. The reliability of its measurements may be questioned due to the low accuracy. Moreover, its small spatial resolution raises doubts about the representativeness of the measurements, as it may not capture the full fluid characteristics. Despite these uncertainties, its simplicity remains a notable advantage.

4

Methodology

This chapter outlines the experimental methodology employed in this thesis. It includes the selection of sensors, design of the setup, detailed installation procedures, calibration steps, testing protocols, parameter variations, data collection, and sample processing methods.

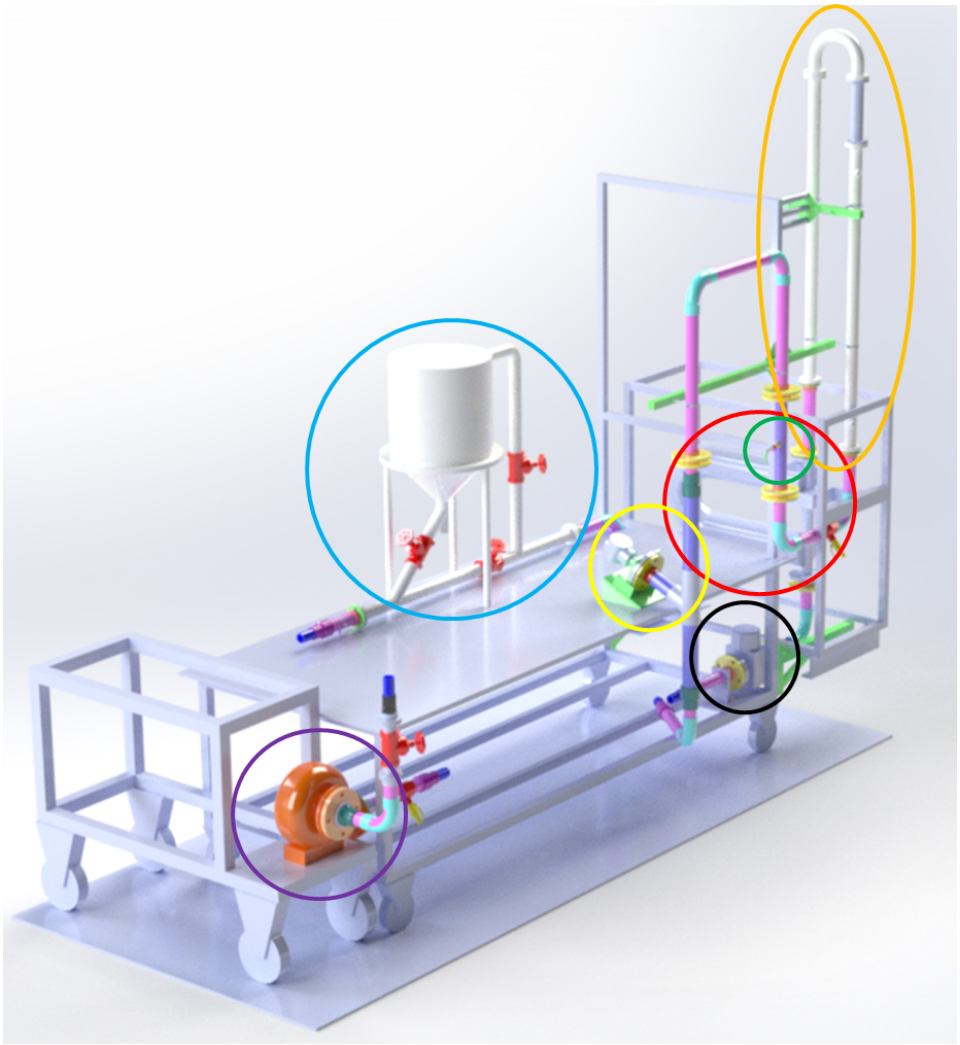

Figure 4.1: Overview of the experimental setup

4.1. Experimental Setup and Sensor Overview

The experimental setup is shown in Figure 4.1, which is explained step by step. The process begins in the hopper (light blue circle), where water and sediment are continuously mixed. The mixture is then drawn into the pump (purple circle) and flows through the flow velocity sensor (black circle). It then proceeds upward through the Coriolis sensor (red circle, positioned toward the back), before travelling through the U-loop (orange oval). Finally, the mixture passes through the manual sampling section (yellow circle) and returns to the hopper, completing the loop. At the hopper, there are three red components, which are valves. These valves are used to control the flow through the hopper. By adjusting the valves, the amount of flow through the hopper and the pipe below it can be regulated.

For the test setup, a 40 mm inner diameter flow loop is used. This diameter was selected because a setup with this pipe size was already available at the TU Delft dredging lab. The existing setup was modified to meet the specific requirements of this study. No scaling effects were anticipated, as this thesis focuses on concentration measurement, which is independent of size. Additionally, the setup operates within the same flow regime as the full-scale system. The relatively small pipe size also ensured that the pipes, connection pieces, and sensors were relatively inexpensive.

4.1.1. Pipe Diameter and Velocity Changes

The test setup incorporates different pipe sections, each with its own diameter. However, the majority of the pipes have an inner diameter (ID) of approximately 40 mm. For the purposes of this report, the flow velocity measured in the flow velocity sensor is considered the reference velocity. The flow velocity sensor itself has an inner diameter of 38 mm.

$$Q = v \cdot A \tag{4.1}$$

$$A = \pi \left(\frac{D}{2} \right)^2 \tag{4.2}$$

$$Q_1 = Q_2 \tag{4.3}$$

$$\frac{v_2}{v_1} = \frac{D_1^2}{D_2^2} \tag{4.4}$$

where:

- $Q\,(\mathrm{m}^3/\mathrm{s})$: Flow rate.
- $v\,(\mathrm{m/s})$: Flow velocity.
- $A\,(\mathrm{m}^2)$: Cross-sectional area of the pipe.
- $D\,(\mathrm{m})$: Pipe diameter.
- $Q_1, Q_2\,(\mathrm{m}^3/\mathrm{s})$: Flow rates at different sections.
- $v_1, v_2\,(\mathrm{m/s})$: Flow velocities at different sections.
- $D_1, D_2\,(\mathrm{m})$: Pipe diameters at different sections.

This velocity ratio indicates the relative change in flow velocity between different pipe sections. For instance, a pipe section with a 42 mm ID will have a velocity ratio of 0.819. This means that the flow velocity in this section is 81.9% of the velocity in the flow velocity sensor.

Table 4.1: Velocity Fraction vs. Inner Diameter (ID)

	Flow Velocity Sensor	U-Loop Section	Rest	Vibrating Fork Section
Inner Diameter (mm)	38	40	45	57
Velocity Fraction (%)	100.00	90.25	71.31	44.44

4.1.2. Temperature Monitoring

Temperature has a significant impact on the density of water, and consequently on the overall density of the mixture. Accurate temperature monitoring is therefore essential for precise concentration measurements. In this setup, the temperature is measured using the Coriolis sensor's built-in temperature sensor. The process of converting density to concentration is further explained in subsection 5.2.4. The density of water is calculated using the following equation [6]:

$$\begin{aligned}\rho_w =& 9.99864928 \cdot 10^{2} + 5.72357369 \cdot 10^{-2} \cdot T - 7.96007024 \cdot 10^{-3} \cdot T^{2} \\ &+ 5.32777547 \cdot 10^{-5} \cdot T^{3} - 2.60322680 \cdot 10^{-7} \cdot T^{4} + 5.11178237 \cdot 10^{-10} \cdot T^{5}\end{aligned} \tag{4.5}$$

where:

- ρ_w (kg/m^3): Water density.
- T (°C): Water temperature.

4.2. Installation Procedures

4.2.1. Installation: Vibrating Fork Sensor

The Sentec SPX504 Flange Tuning Fork Liquid Density Meter is utilised in this thesis. With a measurement accuracy of $\pm$ 2 kg/m³ and a measurement range of 0-2500 kg/m³. However, the manual provided with the sensor contains extremely limited information [80]. Due to this lack of detail, the installation manual for a similar sensor by the Emerson brand has been referenced for additional information [27].

If the sensor's flow velocity is:

- Below 0.5 m/s, it is recommended to install the sensor as a free-stream application.
- Above 0.5 m/s, the sensor should be installed as either a T-piece or a flow chamber application.
- Alternatively, if the pipework can be expanded to reduce the flow velocity to between 0.3 and 0.5 m/s, a free-stream application installation is recommended.

For the purposes of this thesis, the T-section configuration was selected due to its ease of construction and compatibility with the existing setup [27].

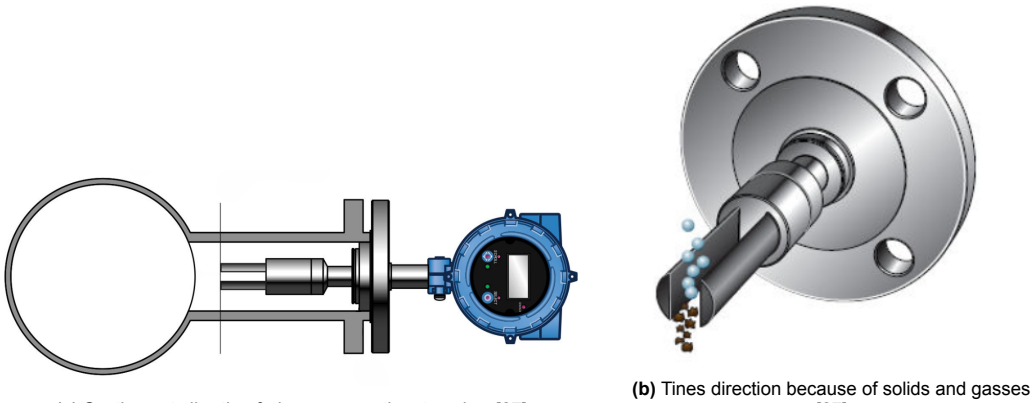

(a) Section cut vibrating fork sensor section, top view [27]

(b) Tines direction because of solids and gasses [27]

Figure 4.2: Section cut vibrating fork sensor section and Tines direction

T-section Installation

- For horizontal or vertical installations, use a pipe with an inner diameter (ID) of at least 51 mm. In this setup, the pipe size was increased to an outer diameter of 63 mm to meet the ID requirement.
- For both vertical and horizontal pipes, the sensor must always be installed on the side of the pipe. For horizontal pipes, never mount the sensor on the top.
- The sensor should be oriented in such away that the gap between the tines is vertical. This positioning prevents bubbles or solids from becoming trapped in the sensor, allowing solids to sink and bubbles to rise [27]. This configuration is shown in Figure 4.2b.

The T-piece must be dimensioned such that the sensor tines are sufficiently retracted from the main pipe wall. The distance is determined by the maximum flow velocity in the system.

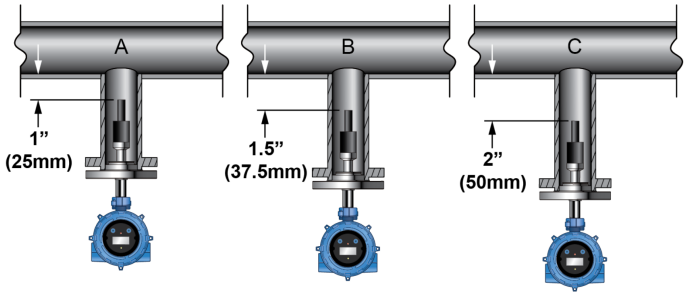

Figure 4.3: Installation depth vibrating fork sensor T-section [27]

A. Velocity ≤ 3 m/s
B. 3 m/s < velocity ≤ 4 m/s
C. 4 m/s < velocity ≤ 5 m/s

For this experiment, the ID is 57 mm, and the maximum flow velocity is 4 m/s. This results in a flow velocity of 1.78 m/s in the vibrating fork section. Thus, condition A applies, requiring the tines to be positioned 25 mm from the main pipe wall.

Flow velocity near the pipe wall and fluid viscosity must remain within specified limits to ensure proper refreshment of the fluid in the pocket [27].

Y-section Installation

During pre-experimental testing, it was observed that solids tend to settle in the lower part of the T-section, potentially affecting the vibrating fork sensor’s performance. This sediment accumulation results in an unrepresentative mixture in the pocket, leading to a higher measured density than in the rest of the system.

To mitigate this issue, the configuration was modified to a Y-section. The Y-section has a slanted angle towards the main flow pipe, allowing heavier solids to migrate back into the main flow and rejoin the system [27]. Additionally, a flow catcher was introduced at the top of the Y-section to direct a portion of the main flow into the pocket, increasing turbulence. This reduces sediment settling and ensures a more representative mixture in the pocket.

An issue introduced by switching from a T-section to a Y-section is the accumulation of air at the highest point in the Y-section. This air needs to be removed because it can influence the density measurement. The air is removed by loosening the seal and allowing the air to escape.

Both the T-section and Y-section configurations were subjected to CFD simulations using SOLIDWORKS Flow Simulation, with the highest system flow velocity of 4 m/s. The simulations, detailed in Appendix E, demonstrate improved flow velocity and fluid refreshment in the pocket of the Y-section compared to the T-section.

Thin-Walled Pipes

The manufacturer’s manual states: “For hygienic applications, a normal 2 in (51 mm) hygienic tube is too thin for this application; it can vibrate in sympathy with the fork, causing measurement errors.” Since

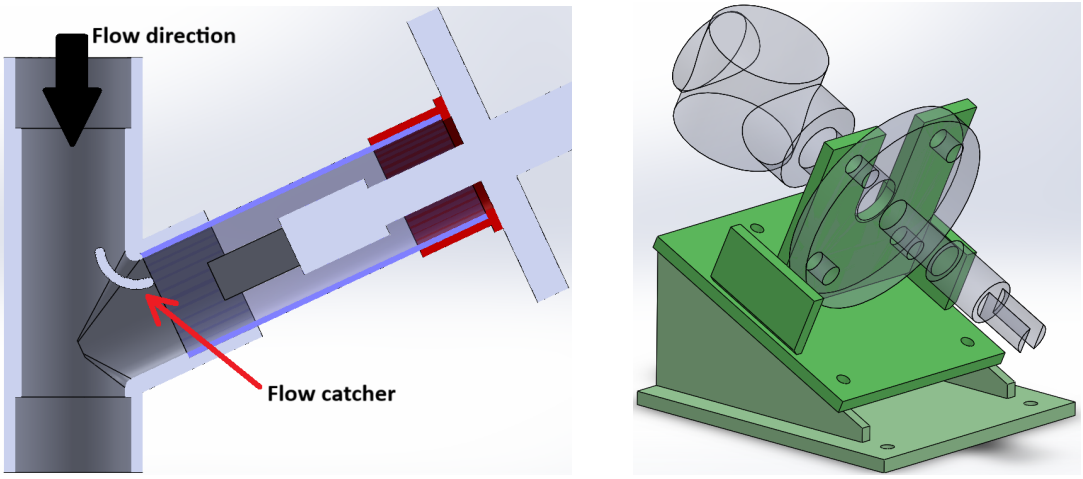

(a) Section view Y-section, vibrating fork **(b)** Frame vibrating fork

Figure 4.4: Section view Y-section and Frame vibrating fork

this thesis uses transparent PVC, which is weaker than steel, reinforcements were added to prevent such errors. A steel frame was constructed to secure the sensor to the table, eliminating unwanted vibrations. The frame is made of 8 mm thick steel to ensure stability and reduce vibrations.

4.2.2. Installation: Coriolis Sensor

This thesis uses the Micro Motion ELITE CMF200M Coriolis Meter from Emerson. With a measurement accuracy of $\pm$ 0.5 kg/m³ and a measurement range of 0-5000 kg/m³ [61]. For optimal performance, the Coriolis sensor should be installed in the recommended orientation. Since this thesis involves testing a slurry fluid, which may also contain air bubbles, the orientation labelled as (a1) in the manufacturer's installation manual is recommended [16].

Process	Primary preferred orientation	Secondary preferred orientation	Alternate suitable orientation
Liquids && slurries	a1	a2	a3
Gases	b1	b2	b3

Figure 4.5: Preferred sensor orientation

4.2.3. Installation: U-loop

The U-loop uses a differential pressure sensor to measure the liquid's density. Sediment catchers are included in the U-loop and are positioned between the tubes connecting to the differential pressure

sensors. These catchers prevent sediment from entering the tubes and causing blockages by capturing sediment as it settles from the mixture.

Pressure drops may occur in the U-loop if bends or diameter changes are located too close to the pressure measuring points. To minimize these drops, the pressure measurement points should be positioned at least five pipe diameters in distance from any bends or diameter changes.

To ensure proper functioning of the differential pressure sensors, the connection tubes must be completely filled with an incompressible liquid, such as water. Air must be removed, as its compressibility can absorb some of the system's pressure, leading to inaccurate measurements. As a pressure differential sensor, the Rosemount 1151DP-4 S22 Pressure Transmitter is used. These sensors have a variable measurement range of $0\text{-}2500/37000\,\text{Pa}$ [69].

4.2.4. Installation: Flow Velocity Sensor

The Proline Promag 55s sensor from Endress+Hauser is used to measure the velocity of the mixture. With a measurement accuracy of $\pm$ 0.2% or $\pm$ 2 mm/s and a measurement range of 0.01 - 10 m/s. 0.01 to 10 m/s. This sensor is specifically designed for slurries containing abrasive materials, such as sand or stone, which are common in ore slurry [5].

To avoid damage to the sensor, it must not be installed on the pump's outlet side. Low-pressure conditions on the intake side can create a partial vacuum, potentially damaging the lining of the measuring tube.

Although a vertical orientation is recommended for slurries with high sedimentation potential (e.g., containing sand or stones), sedimentation is not expected during these tests because the critical velocity will not be reached, as calculated in Section 2.3. A horizontal orientation was chosen instead, as it better suits the overall design.

Proper support is crucial to prevent excessive vibrations of the sensor. Figure 4.6 shows the support structure used for the velocity sensor.

Figure 4.6: Velocity sensor support

To ensure accurate measurements, the sensor should be installed away from fittings such as valves, T-pieces, or elbows, for at least the requirement distance mentioned below [5]:

- Inlet run: $\geq 5 \times \text{DN}$
- Outlet run: $\geq 2 \times \text{DN}$

4.2.5. Installation: Manual Sample Section

The manual sampling section is inspired by the design of a pitot tube. The tube's opening faces the flow direction, ensuring that the mixture enters the sample tube when the valve is opened. The tube opening faces downward to prevent sediment from settling inside the sample tube.

It is assumed that the pressure in the system and the friction forces in the sample tube cancel out, enabling isokinetic sampling. Isokinetic sampling is discussed further in Section 3.1.

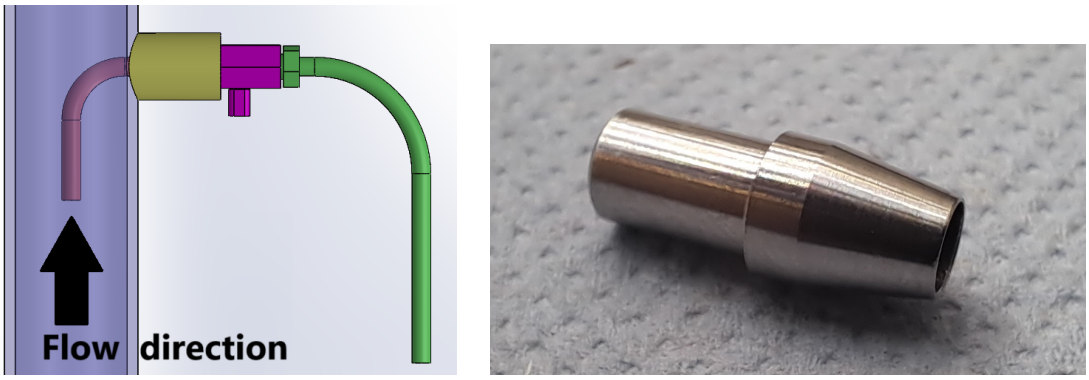

(a) Manual sample section view

(b) New sample nozzle, reducing intake hole

Figure 4.7: Manual sample section view and New sample nozzle

During early testing, it was discovered that isokinetic sampling was likely not achieved because the diameter of the sample tubes was too large, an inner diameter of 5 mm. To address this issue, a custom transition piece was machined to reduce the intake diameter. This transition piece, shown in Figure 4.7b, has an inner diameter of 3.5 mm, reducing the intake area from 19.6 mm^2 to 9.62 mm^2. After implementing this modification, no further issues with isokinetic sampling were observed in subsequent tests.

4.3. Calibration

4.3.1. Calibration: Vibrating Fork

The operating range of the vibrating fork sensor for density measurement is 0–2500 kg/m^3. Calibration requires a wide range of densities to minimize errors caused by random noise or measurement inaccuracies. Using a broad range ensures a reliable calibration curve.

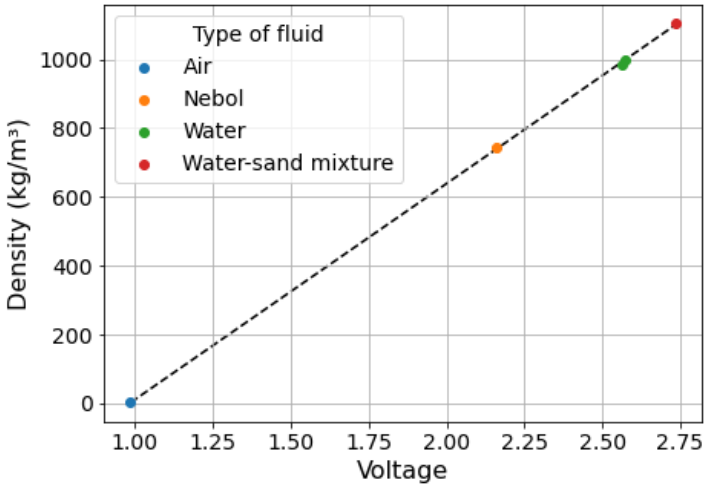

Figure 4.8: Calibration curve for vibrating fork, y = 628.4x + 618.53, R^2 = 0.9999.

For Nebol, the vibrating fork and probes are secured in a container filled with Nebol. For the air, water, and water-sand mixture, the sensor is fixed in the test setup, which is filled with the specified fluid.

To calibrate the sensor, the voltage output is recorded using a data acquisition system while monitoring the display on the vibrating fork sensor. Between 700 and 1000 data points are collected. These data points are compiled into a spreadsheet, resulting in the graph shown in Figure 4.8. Statistical analysis

is performed, producing a trend line $y = 628.4x - 618.53$. The R^2 value for this trend line is 0.9999, indicating an excellent correlation between the trend line and the data points.

4.3.2. Calibration: Coriolis

The Coriolis sensor is equipped with its own data acquisition system that supports calibration. Calibration can be performed using either air or water. In this thesis, water calibration was selected. The density of water is calculated using the measured temperature and Equation 4.5. The calculated density is then entered into the Coriolis sensor's software to complete the calibration process. It is crucial to ensure that the system contains only tap water (free of sediment) during calibration.

4.3.3. Pressure Sensor Calibration (U-loop)

The U-loop uses differential pressure sensors (Rosemount 1151DP-4 S22) to measure pressure. These sensors have a variable measurement range. To reduce errors during testing, the smallest possible measurement range is selected [77]. In this subsection the pressure range for the pressure differential sensors is calculated.

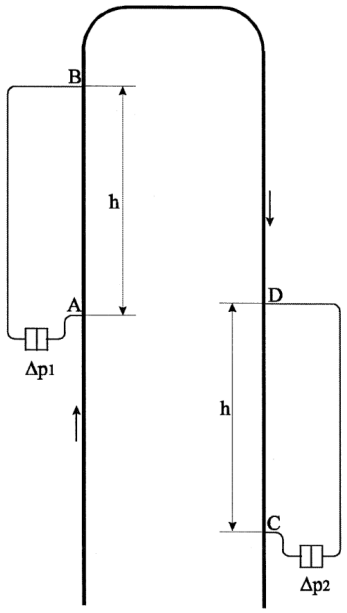

Figure 4.9: U-loop schematic drawing [77].

It is assumed that Δp_r (pressure loss due to friction) is equal in the upward and downward pipelines. While there may be small differences in mixture density (ρ_{m}) between the upward and downward pipelines due to sediment settling, summing the measurements provides an accurate average transport density. The term $(\rho_m - \rho_w)$ accounts for the tubes between the measuring points and the sensor being filled with water [77].

The pressure differences at the measurement points are calculated using the following equations:

$$\Delta p_1 = (\rho_m - \rho_w)\, g\, h + \Delta p_r \tag{4.6}$$

$$\Delta p_2 = (\rho_m - \rho_w)\, g\, h - \Delta p_r \tag{4.7}$$

Where:

- Δp_1 (Pa): Pressure difference in the upward pipe.
- Δp_2 (Pa): Pressure difference in the downward pipe.
- $\rho_m = 1097.94$ kg/m^3: Mixture density.
- $\rho_w = 998.21$ kg/m³ (at 20 °C, [6]): Density of water.

- $g = 9.81\,\text{m/s}^2$: Gravitational constant.
- $h = 1.02\,\text{m}$: Distance between pressure measurement points.
- $\Delta p_r\,(\text{Pa})$: Pressure difference due to wall friction.

Friction Loss Calculation Using Darcy-Weisbach and Colebrook-White Equations

Pressure loss in the pipe section is calculated using the Darcy-Weisbach and Colebrook-White equations [95].

Step 1: Calculate Reynolds Number

$$Re = \frac{\rho_m\, v\, D}{\mu} \tag{4.8}$$

Where:

- $v\,(\text{m/s})$: Fluid velocity.
- $D = 0.04\,\text{m}$: Pipe diameter.
- $\mu = 0.001\,\text{Pa} \cdot \text{s}$: Dynamic viscosity (assumed to be similar to water).

Step 2: Solve the Colebrook-White Equation

For turbulent flow, the friction factor f is calculated using the Colebrook-White equation [18]:

$$\frac{1}{\sqrt{f}} = -2\log\left(\frac{\varepsilon/D}{3.7} + \frac{2.51}{Re\sqrt{f}}\right) \tag{4.9}$$

Where:

- $\varepsilon = 0.0000015\,\text{m}$: Pipe roughness [67].
- Re: Reynolds number (from Step 1).

This equation requires an iterative or numerical method to solve for f. A Python script was used for this calculation (see Appendix F).

Step 3: Calculate Friction Loss Using the Darcy-Weisbach Equation

$$\Delta P = f \cdot \frac{L}{D} \cdot \frac{\rho_m v^2}{2} \tag{4.10}$$

Where:

- $f = 0.0163$: Friction factor (from Colebrook-White).
- $L = h = 1.02\,\text{m}$: Pipe length.

Table 4.2: Pressure differential and friction losses

ρ_m (kg/m^3)	v (m/s)	Re	f	ΔP (Pa)	Δp_1 (Pa)	Δp_2 (Pa)
998.21	0	0	0	0	0	0
998.21	4	160000	0.016608	3387.94	3387.94	-3387.94
1097.94	0	0	0	0	990.61	990.61
1097.94	4	175840	0.016318	3658.54	4649.15	-2667.93

The pressure differences and friction losses for extreme conditions were calculated using a Python script. Table 4.2 summarizes the results. The sensors are calibrated by using the Druck DPI 615 Pressure Calibrator, with an accuracy of 0.025% and a range of 0 - 20 bar. To provide a safety margin, the following pressure range is used:

- $\Delta p_1\,(0, 6000)\,\text{Pa}$
- $\Delta p_2\,(-4500, 1500)\,\text{Pa}$

4.4. Test Conditions

4.4.1. Concentration Variation

Concentration is the primary parameter being varied in this study to evaluate how differences in concentration affect the accuracy of each methodology. As concluded in Chapter 2.1, a concentration range of 10–75 g/L in seawater (density 1025 kg/m^3) results in a mixture density range of 1031.5–1074.1 kg/m^3. It is crucial to select measurement intervals that fully cover this range.

For this experiment, density sensors are used, meaning the density of the fluid is the key parameter rather than the concentration. Smaller steps are used in the lower density range (where relative changes are higher), while larger steps are applied in the upper range, reaching a maximum mixture density of 1071.7 kg/m^3.

Table 4.3: Concentration conversions

c (g/L)	ρ_m (kg/m^3)	V_s (volume fraction of sediment)	m_{add} (added mass per liter of water)
5	1001.33	0.002	5.01
10	1004.44	0.004	10.04
20	1010.68	0.008	20.15
40	1023.14	0.015	40.61
80	1048.08	0.03	82.49
160	1097.94	0.06	170.28

The following equations are used to calculate the mixture density and the added mass per liter of water. The concentration and the added mass per liter of water differ because part of the water is replaced by sediment, which is reflected in the increasing volume fraction:

$$V_s = \frac{c}{\rho_s}, \quad V_w = 1 - V_s \tag{4.11}$$

$$\rho_m = V_s \cdot \rho_s + V_w \cdot \rho_w \tag{4.12}$$

$$m_{add} = \frac{c}{V_w} \tag{4.13}$$

Where:

- c (g/L): Concentration of sediment in the mixture.
- m_{add} (kg/m³): Added mass of sediment per liter of water.
- V_w (-): Volume fraction of water.
- V_s (-): Volume fraction of sediment.
- ρ_m (kg/m³): Density of the mixture.
- ρ_w = 998.21 kg/m³ (at 20 °C, [6]): Density of water.
- ρ_s = 2650 kg/m³ [17]: Density of sediment.

At the start of each test series, a calibration run with clean tap water is performed to verify sensor accuracy. Changes in concentration can also alter the flow regime, potentially creating a concentration gradient in the flow.

4.4.2. Sediment Type Variation (Grain Size)

The sediment mixture in real-life applications consists of clay with a grain size of 11$\pm$3 µm and nodule fines smaller than 150 µm, further information in section 2.2. Changing sediment type affects two key parameters: grain size and adhesive/cohesive properties. Grain size influences settling velocity, which can alter the flow regime and create concentration gradients, as explained in Subsection 2.3.

For the B and C-series, non-cohesive sediment with 99 % silica is used due to its consistent grain size and low adhesion, minimizing measurement drift. For the D and F-series, clay is used to study cohesive sediments, which can form flocs and adhere to sensors, impacting settling behaviour and measurement accuracy. The sieve analysis of different sediments are represented in Appendix H.

The sediments for the first three measurement series are chosen to represent the entire range of applications, with each sediment covering approximately one-third of the range:

Table 4.4: Sediment properties ($\approx$ indicates interpolated values)

Series, Reference	Type	Name	D_{10} (µm)	D_{50} (µm)	D_{90} (µm)	Grain density (kg/m^3)
B, Coarse	Sand	Multiquartz HN 0.1–0.3 mm [62]	≈ 117	168	≈ 254	2650 [17, 62]
C, Medium	Silt	Sibelco Millisil M10 [75]	4	23	60	2650
D, Fine	Clay	KAOLIN ZETTLITZ Ia [2]		1.3	≈ 7.5	2620
F, Deep sea	Clay	NORI's sediment [43]	≈ 7.2	11	≈ 14.8	2500

Stokes Number

The purpose of calculating the Stokes number (St) for sediment particles in a water mixture is to understand how well the particles follow the vibrations caused by sensors (such as Coriolis and vibrating fork sensors). These sensors measure the concentration of the mixture by vibrating the fluid, and the particles ability to follow these vibrations affects the accuracy of the measurements [71].

The Stokes number provides an indication of whether the particles can keep up with the oscillating motion of the fluid caused by the sensors. In this context:

- Maximum Velocity: Instead of using the flow velocity, the *maximum velocity* of the sensor's vibrations is used in the Stokes number formula. This is because the motion affecting the sediment particles is induced by the sensor's vibrations. The maximum velocity depends on the amplitude and frequency of these vibrations.
- Characteristic Length: The *characteristic length* is defined as twice the amplitude of the sensor's vibrations. This describes the extent of the oscillating motion of the sensor and, consequently, the sediment particles.

$$v_{\text{max}} = 2\pi f A \tag{4.14}$$

$$\tau_p = \frac{\rho_p d_p^2}{18\mu} \quad , \quad \tau_f = \frac{L}{v_{\text{max}}} \tag{4.15}$$

$$St = \frac{\tau_p}{\tau_f} \tag{4.16}$$

Where:

- v_{max} $(\mathrm{m/s})$: Maximum velocity of the sensor's vibrations.
- f (Hz): Sensor's vibration frequency.
- A (m): Sensor's vibration amplitude.
- τ_p (s): Particle relaxation time.
- ρ_p $(\mathrm{kg/m^3})$: Particle grain density.
- d_p (m): Particle diameter.
- $\mu = 0.001$ Pa · s: Dynamic viscosity (assumed to be similar to water).
- St: Stokes number (dimensionless).
- τ_f (s): Fluid timescale.
- L (m): Characteristic length ($L = 2A$).

Purpose of the Stokes Number Analysis

By calculating the Stokes number with these parameters, we can determine if the sediment particles follow the sensor-induced vibrations. A small Stokes number ($St \ll 1$) indicates that particles closely follow the fluid motion, ensuring accurate sensor readings. In contrast, a large Stokes number ($St \gg 1$) suggests that particles deviate from the fluid motion, potentially affecting the sensor's ability to measure the concentration accurately [71].

Table 4.5: Stokes Number Calculations for Various Particles and Sensors

Series	D_{50} (μm)	ρ_p (kg/m^3)	Sensor	f (Hz)	A (mm)	v_{max} (m/s)	St
B, Coarse	168	2650	Coriolis	71	10	4.461062	0.92683
B, Coarse	168	2650	Vibrating fork	975	1	6.126106	12.727597
C, Medium	23	2650	Coriolis	71	10	4.461062	0.017371
C, Medium	23	2650	Vibrating fork	975	1	6.126106	0.238552
D, Fine	1.3	2620	Coriolis	71	10	4.461062	0.000055
D, Fine	1.3	2620	Vibrating fork	975	1	6.126106	0.000753
F, Deep sea	11	2500	Coriolis	71	10	4.461062	0.003749
F, Deep sea	11	2500	Vibrating fork	975	1	6.126106	0.051476
Nodule fines	≈150	3460	Coriolis	71	10	4.461062	0.964705
Nodule fines	≈150	3460	Vibrating fork	975	1	6.126106	13.247704

For coarse sediment, the Stokes number is significantly high, indicating that it will start to affect the performance of the sensor. The Stokes number for nodule fines is similar to that of coarse sediment, suggesting that these two types of sediment will respond in a similar manner to the vibrations of the sensor. For the vibrating fork sensor, the Stokes number for medium sediment is also substantially high, which implies that it might influence the sensor's performance.

4.4.3. Flow Velocity Variation

In full-scale mining tests, the typical flow velocity is 3.9 m/s. To evaluate the robustness of the methodologies, velocities of 2, 3, and 4 m/s are tested. Speeds above 5 m/s result in excessive friction losses and are excluded, while speeds below 2 m/s are not economical which is why this is beyond the scope of this study.

4.5. Mixture Creation

4.5.1. Measuring the Volume of the Test Setup

To accurately prepare the desired mixture concentration, the volume of water in the setup must be measured precisely. A rough estimate is first obtained by summing the lengths of all pipe sections (l) and calculating the volume using the radius ($r = 0.042\,\text{m}$):

$$V = \pi r^2 l \tag{4.17}$$

After including estimated volumes for the pump and slurry tank, the rough estimate is 75 L.

To refine this, buckets are filled and weighed accurately. The water is then added into the setup until the desired level is reached. The empty buckets are weighed again, and the difference gives the water mass in the setup. This mass is converted into volume using the water density, calculated based on its temperature using Equation 4.5.

4.5.2. Adding Sediment to the Test Setup

Once the water volume is determined, the required sediment mass for each concentration level can be calculated by multiplying m_{add} by the water volume. Based on the 75 L rough volume estimate, approximately 9.5 kg of sediment is needed per test:

$$m_{\text{total\_add}} = V_{\text{setup}} \cdot m_{\text{add}} \tag{4.18}$$

Where:

- $m_{\text{total\_add}}$ (kg): Total sediment mass added to the setup.
- V_{setup} (l): Water volume in the system, as calculated in Subsection 4.5.1.
- m_{add} (g/L): Sediment mass per liter of water.

4.6. Quality Control

4.6.1. Setup Support

Since several measurement techniques utilized in this thesis rely on vibrations to obtain data, it is essential to minimize any unintended vibrations in the setup. Vibrations can introduce errors due to resonance, either from the sensors themselves or from nearby components. To mitigate this, the entire setup is securely mounted to the floor using props, eliminating any instability caused by wheels. This approach ensures a solid and stable connection to the ground.

4.6.2. Plugs to Fill Pockets

The system contains pockets with low flow velocities. These pockets can allow sediment to settle. When sediment settles, it is no longer part of the system, which reduces the true concentration. To improve the accuracy of the theoretical concentration, plugs are placed in these pockets to prevent sediment from settling.

4.7. Data Acquisition of Continuous Methodologies

The signals from each continuous sensor are connected to a data acquisition system (DAS) that converts them into density (or concentration) values. The DAS also logs these values for analysis and comparison across sensors.

Two different data acquisition systems are used:

1. **LabVIEW (National Instruments):** Connected to the differential pressure sensors of the U-loop, the vibrating fork sensor, and the flow velocity sensor. It uses a 4-20 mA analog signal for communication.
2. **ProLink III (Emerson):** Connected to the Coriolis sensor (Coriolis density and temperature signal). It uses a digital signal (RS 485) for communication.

Both systems record timestamps in the format: day/month/year hour:minute:second. The LabVIEW system has a sampling interval of 0.05 ms, while the ProLink system samples at 0.5 ms. This results in the LabVIEW system producing 10 times more data points. For a 5-minute test, the LabVIEW system generates 6000 data points, while the ProLink III system generates 600 data points. Data handling is explained in Section 5.2.

4.8. Manual Sample Processing

4.8.1. Taking the Sample

To measure the sample volume accurately, a 100 mL volumetric flask with an accuracy of ± 0.1 mL [91] is used. A larger flask would remove too much volume from the system, while a smaller flask might make obtaining a representative sample difficult. Initially, 3 samples were taken, but due to high variability, 5 samples are now taken to improve statistical consistency.

Sampling is performed using the specialized section described in Section 4.2.5. The valve is fully opened for isokinetic sampling, with the flow rate reduced as the flask fills to precisely reach the 100 mL mark.

The sample is then transferred to a sample container, and a squirt bottle is used to remove all sediment from the flask. The flask is cleaned quickly for the next sample. This process is repeated 5 times, with each sample taking about 1 minute.

(a) Samples into the oven.

(b) Scale for 100g, with an accuracy of $\pm$ 0.001g.

Figure 4.10: Comparison of sample preparation and weighing.

4.8.2. Filter Paper Usage and Drying

Samples are processed using filter papers, which are folded, marked, and weighed beforehand. Different filters are used depending on the sediment type, as shown in Table 4.6. The initial filter weights are recorded in an Excel file. The sample is poured through the filter, and a squirt bottle ensures all sediment is transferred. The filters are dried in an oven at 98 °C for 4 hours, as recommended in [20], to ensure complete drying. The oven is shown in Figure 4.10a.

Table 4.6: Filter paper types

Series, Reference	D_{10} (µm)	D_{50} (µm)	D_{90} (µm)	Name filter paper	Pore size (µm)
B, Coarse	≈ 117	168	≈ 254	MN-617 [52]	7–12
C, Medium	4	23	60	MN-616 [51]	4–7
D, Fine		1.3	≈ 7.5	MN-619 [53]	1–2
F, Deep sea	≈ 7.2	11	≈ 14.8	MN-619 [53]	1–2

After drying, the filter plus sediment is weighed, using the scale seen in Figure 4.10b. The sediment mass is calculated by subtracting the filter's initial weight. The data is logged in Excel, and is used for statistical analysis.

4.8.3. Collection of Manual Samples (Weigh Measurement)

Samples are collected as follows:

1. Open the valve for 2 seconds to remove residue.
2. Collect a 100 mL sample.
3. Measure the water volume in the sample.
4. Weigh the filter and record its weight.
5. Filter the sample.
6. Dry the sample in the oven at 97 °C.
7. Weigh the dried sample and record the weight.
8. Save the sample for size analysis.
9. Repeat 5 times, with 1-minute intervals between samples.

4.9. Experiment Checklists

1. Add the appropriate amount of sediment to the hopper.
2. Ensure no air remains in the tubes by using a venting cap.
3. Start the pump and adjust to the correct flow velocity (no flow through the hopper yet).
4. Open the valve from the hopper, followed by the valve to the hopper.
5. Allow the system to reach equilibrium (10 minutes).
6. Verify all sensors are operational.
7. Start the test by activating the data acquisition systems and taking the first manual sample.
8. Take the last manual sample and stop the data acquisition systems.
9. Collect the sediment from the hopper using a funnel.

4.10. Uncertainty Budget

In any experiment, errors occur at various stages of the process. These errors are estimated and summarized in an error propagation chart, shown in Figure 4.11. This chart illustrates how individual errors accumulate and impact the overall accuracy of the mixture concentration measurements. The orange blocks represent sources of error, while the green blocks denote calculated errors for certain concentrations.

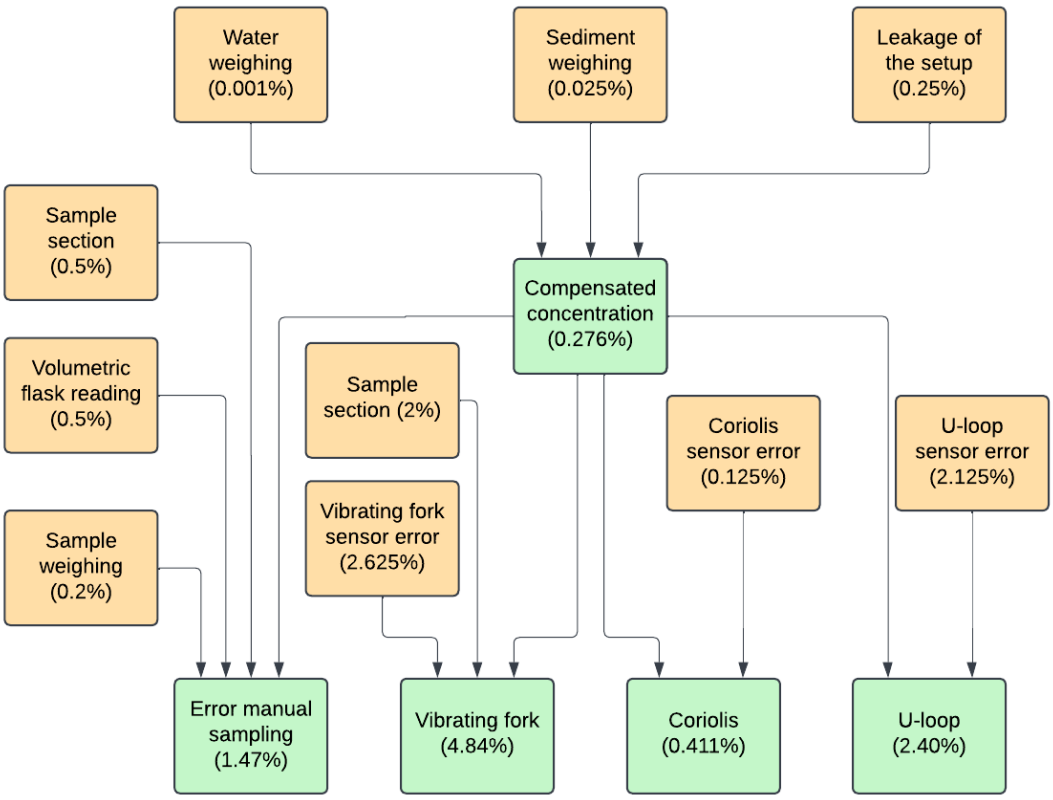

Figure 4.11: Error propagation chart

- The water weighing error is estimated by dividing the scale's accuracy ($\pm$ 0.1 g) [72] by the weight of water in one bucket (10 kg).
- The sediment weighing error is estimated using the scale's accuracy ($\pm$ 0.1 g) and the sediment added for the first test (370 g).
- Leakage and manual sampling errors are based on educated guesses.

- The volumetric flask error is estimated as 10 droplets (0.5 mL) overshooting or undershooting during sampling, relative to a sample volume of 100 mL.
- Sample weighing error is based on the scale accuracy ($\pm$ 0.001 g) and the smallest sample weight (0.5 g).
- Vibrating fork section error is based on an educated guess.
- Vibrating fork sensor error is estimated at 2.1 g/L 3.2 for a mid-range concentration (80 g/L).
- Coriolis sensor error is estimated at 0.1 g/L 3.2 for a mid-range concentration (80 g/L).

5

Results and Analyses

This chapter presents and analyses the experimental data collected from various test series. It examines sensor performance under different operating conditions—considering variations in flow velocity, sediment type, and concentration. Evaluates the accuracy and precision of each measurement methodology.

5.1. Test Matrix

Table 5.1: Concentration test matrix

	Test				Target concentration (g/L)	Flow velocity (m/s)
	b1	c1	d1	f1	0	2
	b2	c2	d2	f2	0	3
	b3	c3	d3	f3	0	4
	b4	c4	d4	f4	5	2
	b5	c5	d5	f5	5	3
	b6	c6	d6	f6	5	4
	b7	c7	d7	f7	10	2
	b8	c8	d8	f8	10	3
	b9	c9	d9	f9	10	4
	b10	c10	d10	f10	20	2
	b11	c11	d11	f11	20	3
	b12	c12	d12	f12	20	4
	b13	c13	d13	f13	40	2
	b14	c14	d14	f14	40	3
	b15	c15	d15	f15	40	4
	b16	c16	d16	f16	80	2
	b17	c17	d17	f17	80	3
	b18	c18	d18	f18	80	4
	b19	c19	d19	f19	160	2
	b20	c20	d20	f20	160	3
	b21	c21	d21	f21	160	4
Sediment	Coarse	Medium	Fine	Deep sea		
Series	B-series	C-series	D-series	F-series		

To systematically investigate how velocity, sediment type, and concentration affect sensor performance, a structured test matrix was designed. By varying these factors individually and in combination, the tests provide insights into sensor behaviour under realistic conditions.

The test matrix, shown in Table 5.1, is presented in a condensed form to summarize the different tests performed. The middle section of the table highlights the target concentrations and velocities for each test. Moving right shows the sediment type, while the bottom section identifies the corresponding sediment series. Each sediment type corresponds to a unique letter. Tests were conducted in sets of three, maintaining the same concentration while varying the velocity. After completing a set, the target concentration was increased.

Baseline tests were conducted as comparison material to observe sensor behaviour with varying flow velocities in clean tap water (no sediment). These tests primarily serve to compensate the U-loop, as discussed in Subsection 5.2.6. The A-series aligns with the B, C, and D-series, while the E-series matches the deep sea sediment due to differences in valve settings, see section 4.1. Table 5.2 summarizes these tests.

Table 5.2: Baseline test matrix

	Test		**Target concentration (g/L)**	**Flow velocity (m/s)**
	a1	e1	0	0
	a2	e2	0	0.5
	a3	e3	0	1
	a4	e4	0	1.5
	a5	e5	0	2
	a6	e6	0	2.5
	a7	e7	0	3
	a8	e8	0	3.5
	a9	e9	0	4
Series	A-series	E-series		

5.2. Data Processing

Data processing involves organising and cleaning the raw measurements from each sensor. This section explains the steps taken to remove incorrect data, align data from the two data acquisition systems, and convert raw signals into useful values, such as concentration. The result is a dataset ready for further analysis.

5.2.1. Data Cleaning

In some tests, the data acquisition systems were not stopped on time, leading to overly long recordings. The end of the recording was detected by a change in velocity either an increase or a decrease in velocity. Therefore, all datasets were trimmed to the correct test durations. The following datasets were adjusted:

- d12, d15, c20
- c4, c14
- f19, f20

5.2.2. Errors in the Dataset

Some tests encountered errors that impacted the recorded data:

For tests b7, b8, b9, and b12, the LabVIEW software logged insufficient data due to an incorrectly set sampling frequency. As a result, the system only captured the first 10 seconds of each test, producing limited data. This issue is evident in the time-series shown in Appendix C, Figures C.1 and C.2.

During the first test, the pressure sensors were not set to the correct pressure range. The pressure range was too narrow, and high pressures caused the sensors to enter error mode, recording invalid values. These erroneous readings were excluded from tables, graphs, and analyses. For example, NaN values appear in Table A.1.

These tests were not repeated due to limited time available to complete all the tests. Additionally, there was insufficient time to redo individual tests. The tests were performed in a series by progressively increasing the concentration, and repeating individual tests would have been extremely time-consuming.

5.2.3. Combining Data Sets

The two data acquisition systems—LabVIEW and ProLink III—recorded timestamps in the same format: day/month/year hour:minute:second.millisecond. ProLink III operated at 0.5 ms, while the LabVIEW system had a sampling frequency of 0.05 ms, which is the smallest sampling interval for the systems. To merge the datasets, a Python script averaged the ProLink III data over each second and aligned it with the LabVIEW data. The merged dataset was then saved for further processing.

5.2.4. Mixture Density to Concentration Conversion

After creating the merged dataset, the next step was to process the raw data. First, the density of water was calculated based on its temperature. Water temperature varied during tests due to ambient conditions and heat generated by the pump. The water density for each time step was calculated using Equation 4.5.

With the water density determined, the densities measured by each sensor were converted into concentrations using Equation 5.2, which is derived from the Equations 5.1.

$$v_s = \frac{c}{\rho_s}, \quad v_w = 1 - v_s, \quad \rho_m = v_s \cdot \rho_s + v_w \cdot \rho_w \tag{5.1}$$

$$c = \frac{\rho_m - \rho_w}{1 - \frac{\rho_w}{\rho_s}} \tag{5.2}$$

Where:

- v_s (-): Volume fraction of sediment.
- c (g/L): Sediment concentration in the mixture.
- ρ_s (kg/m³): Sediment density.
- v_w (-): Volume fraction of water.
- ρ_w (kg/m³): Water density.
- ρ_m (kg/m³): Mixture density.

5.2.5. Effect of Temperature

Water density fluctuates with temperature, which in turn affects the mixture density. Figure 5.1 illustrates the temperature variation over time and its impact on water and mixture densities.

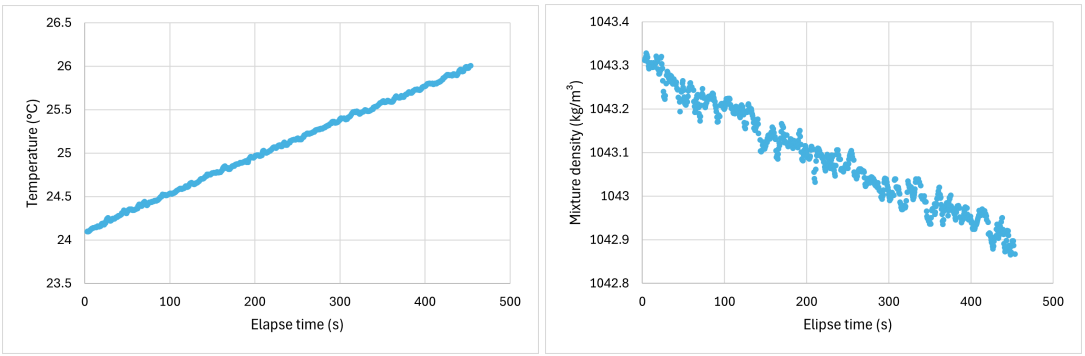

(a) Coriolis temperature over time

(b) Coriolis mixture density over time

Figure 5.1: The effect of temperature on the system

As shown in Figure 5.1b, changes in mixture density result from temperature variations. By calculating the concentration for each time step, the effects of changing water temperature and mixture density cancel out, leaving only concentration variations for analysis.

5.2.6. Post-Testing U-Loop Compensation

As expected, the U-loop required post-processing. Two types of compensations were applied to the signal:

1. **Pressure Compensation**: During the baseline test at zero velocity, the pressure differential across the sensors should theoretically be zero. Any difference observed (highlighted in red in Table 5.3) indicates an offset in the sensors. This offset was subtracted from the differential pressures for all other tests, resulting in the pressure-compensated U-loop measurement.
2. **Velocity Compensation**: After pressure compensation, the water density and the U-loop pressure-compensated density should theoretically remain consistent, even as velocity increases. However, this is not the case in practice, as the increase in velocity introduces a false error in the measured concentration. This error is addressed through velocity compensation. Following pressure compensation, the "Density error (kg/m³)" was calculated by subtracting the "Water density (kg/m³)" from the "U-loop (press. comp.) density (kg/m³)." This "Density error (kg/m³)" is utilised as a compensation value. The compensation value was then subtracted from the density at each velocity (2, 3, and 4 m/s), producing the velocity-compensated U-loop measurement.

Table 5.3: U-loop results of A-series

Velocity (m/s)	DP1 (Pa)	DP2 (Pa)	U-loop old density (kg/m³)	Updated DP1 (Pa)	Updated DP2 (Pa)	U-loop (press. comp.) density (kg/m³)	Water Density (kg/m³)	Density error (kg/m³)
0.0	-31.29	-35.43	993.67	0.00	0.00	998.48	998.48	0.00
0.5	34.48	-116.04	992.93	65.77	-80.61	997.73	998.47	-0.74
1.0	230.36	-326.56	992.19	261.65	-291.13	996.99	998.46	-1.47
1.5	516.20	-615.90	992.02	547.50	-580.47	996.80	998.45	-1.65
2.0	902.07	-1013.02	991.46	933.37	-977.60	996.21	998.42	-2.21
2.5	1382.49	-1510.23	990.62	1413.78	-1474.81	995.32	998.37	-3.05
3.0	1957.29	-2120.99	988.82	1988.59	-2085.56	993.43	998.28	-4.85
3.5	2593.82	-2807.14	986.34	2625.11	-2771.71	990.86	998.18	-7.33
4.0	3243.31	-3480.24	985.16	3274.61	-3444.82	989.40	997.90	-8.51

Both pressure and velocity compensations were applied to the fine sediment tests (D-series) to demonstrate their impact. In Figure 5.2, pressure compensation provides some improvement, while velocity compensation aligns the results closely with the ideal line. In Subsection 5.3.1 the graph is further explained.

Compensation values for deep sea sediment tests (F-Series)

For the tests using deep sea sediment (F-series), slight adjustments to the valve openings (section 4.1) was required resulting in a new baseline test (E-series). Using similar analysis, compensation values for the deep sea sediment test were calculated, as shown in Tables 5.4 and 5.5.

Table 5.4: Pressure compensation value, deep sea sediment test (F-series)

	DP1	DP2
Pressure compensation value	-30.7453	-57.6642

Table 5.5: Velocity compensation value, deep sea sediment test (F-series)

Velocity (m/s)	2	3	4
Velocity compensation value (kg/m³)	-3.19298	-8.07231	-10.6684

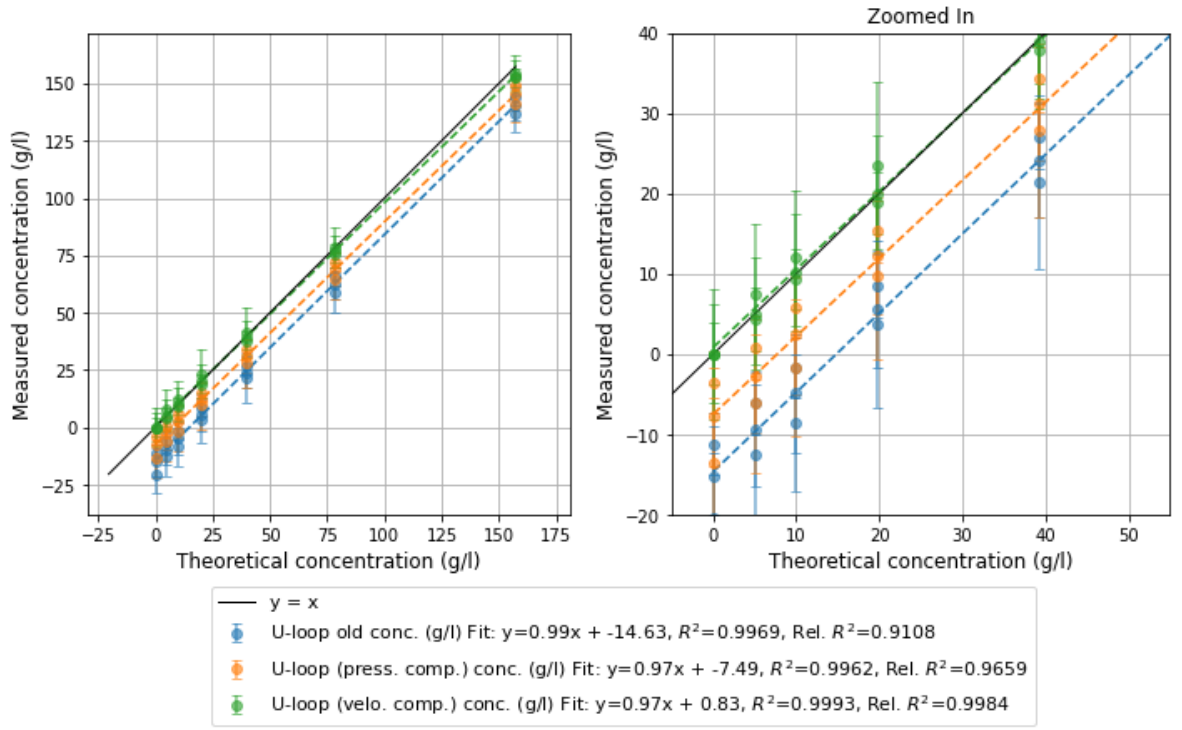

Figure 5.2: U-loop compensation applied to medium sediment tests (D-series)

Note: Following these compensations, the U-loop always records a measured concentration of 0 g/L for a theoretical concentration of 0 g/L, positively impacting its accuracy.

5.2.7. Correcting Target Concentration

During testing, manual samples remove mixture from the system—both water and sediment. After every third test, a new target concentration is created by adding ”Relative added mass, to the previous concentration (g)”, ideally creating the target concentration if no mixture were removed. To keep the total volume of water in the system constant, 1.5 liters of water is also added.

Post-testing, removed sediment was accounted for by subtracting the ”Removed sediment by manual sampling (g)” from the ”Total added mass (g).” From the ”Target concentrations” the ”Theoretical concentration” is calculated, illustrated in the flowchart in Figure 5.3. This theoretical concentration should be extremely close to the true concentration flowing through the pipes. In Table 5.6, the error of the theoretical concentration relative to the target concentration is presented.

Table 5.6: Error of the theoretical concentration relative to the target concentration

	Coarse sediment	Medium sediment	Fine sediment	Deep sea sediment
Target concentration (g/L)	B-series error (%)	C-series error (%)	D-series error (%)	F-series error (%)
5	0.01	0.01	0.01	0.00
10	-1.17	-0.97	-0.95	-1.86
20	-1.89	-1.48	-1.45	-3.71
40	-2.31	-1.67	-1.66	-3.37
80	-2.51	-1.74	-1.73	-2.88
160	-2.54	-1.70	-1.68	-1.95

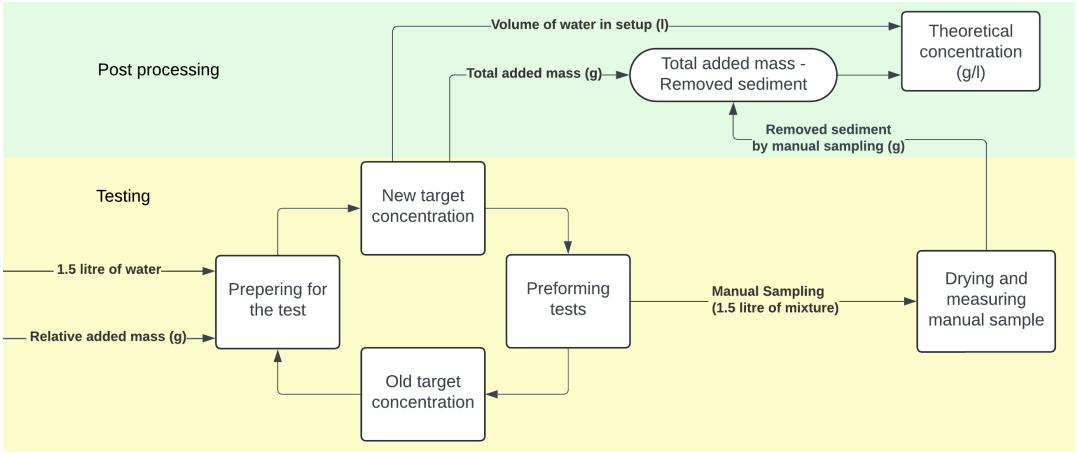

Figure 5.3: Flowchart for correcting target concentration

5.3. Test Results

This section presents the processed sensor data, converted into concentration and other relevant metrics, and compiled into tables. Detailed tables listing statistical parameters such as mean and standard deviation are provided in Appendix A. Here, graphs are used to highlight key observations. First, the *baseline tests* are analysed to understand how sensors behave under varying flow velocities without sediment present. Next, the *concentration tests* are examined to evaluate sensor responses to different concentrations, sediment types, and flow velocities. This two-part analysis provides a comprehensive understanding of sensor performance under diverse conditions.

5.3.1. Statistical Explanation

To visualise the data, graphs are used. Below is a brief explanation of the key elements included in these graphs.

- *Measured concentration (red box):* The value recorded by the sensor.
- *Theoretical concentration (pink box):* The concentration calculated from the known quantities of sediment and water, assuming a perfectly homogeneous mixture.
- *Sensing method (light blue box):* Each methodology is represented by a distinct color in the graph.
- *Trendline (yellow box):* Represents the trend of the sensor data points.
- *R^2 (green box):* Indicates how well the trendline fits the data, measuring the precision of the sensor.
- *Ideal line (black diagonal):* Represents perfect relation between measured and theoretical concentrations.
- *Relative R^2 (dark blue box):* Shows how closely the data aligns with the ideal line, reflecting the accuracy of the sensor.

Precision

Precision measures the consistency of repeated measurements, regardless of their proximity to the true value. Two statistical parameters are used to evaluate precision:

Standard Deviation (STD): This indicates the spread of measured values around the mean for each test. The standard deviation is calculated per test, it will indicate the precision per test. A lower standard deviation reflects higher precision.

R^2: This statistical value shows the proportion of variance in the data that can be explained by the trendline. It is calculated for the mean values across tests, indicating precision between tests. A higher R^2 value implies better precision, a value of 1 is highest and implies perfect correlation.

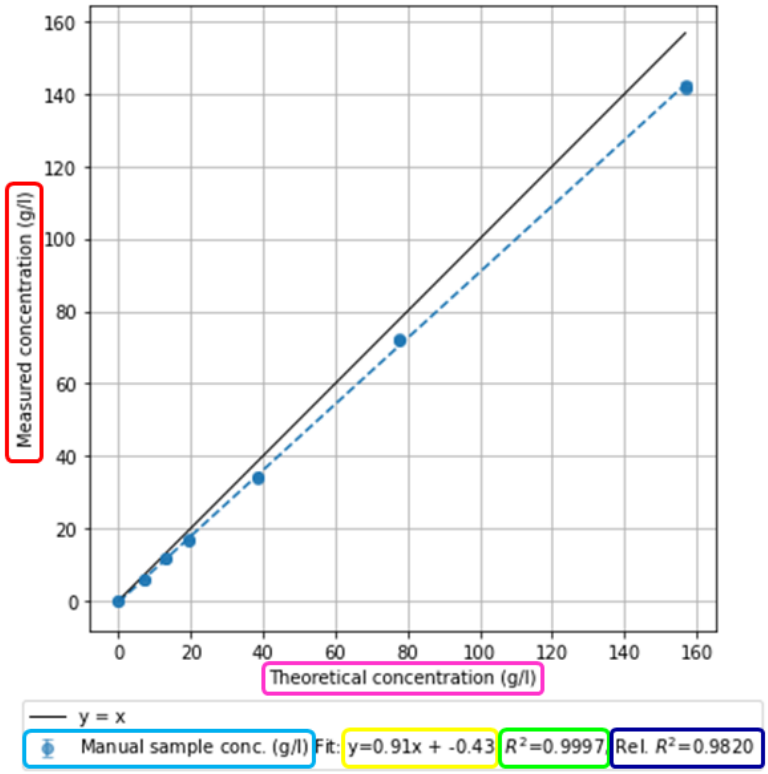

Figure 5.4: Explanation of the graph components

Accuracy

Accuracy assesses how close the measured value is to the true value, in this case, the theoretical concentration. Two statistical measures are used to evaluate accuracy:

Error Calculation: The absolute error represents the difference between the measured concentration and the theoretical concentration:

$$Error = C_{\text{measured}} - C_{\text{theoretical}} \tag{5.3}$$

The relative error normalises this difference by expressing it as a percentage of the theoretical concentration:

$$\text{Relative Error (\%)} = \frac{C_{\text{measured}} - C_{\text{theoretical}}}{C_{\text{theoretical}}} \cdot 100 \tag{5.4}$$

$$\text{Absolute Relative Error (\%)} = \left| \frac{C_{\text{measured}} - C_{\text{theoretical}}}{C_{\text{theoretical}}} \right| \cdot 100 \tag{5.5}$$

Note: When $C_{\text{theoretical}} = 0$, the relative error becomes undefined and is excluded from the analysis.

The absolute relative error provides a normalised measure of error, showing how well the data aligns with the ideal line. However, it does not capture values when the theoretical concentration is zero.

Relative R^2: This value indicates how well the data fits the ideal line, emphasising outliers through the squaring of errors. It is calculated for the mean values of the tests, providing a measure for accuracy.

5.3.2. Baseline Tests

The baseline test results are presented in Figure 5.5. These tests assess the effect of flow velocity on sensor performance in the absence of sediment. The results highlight whether increased velocity leads to erroneous measurements of zero concentration.

For the U-loop, only the pressure-compensated measurement is displayed. The velocity-compensated U-loop signal aligns perfectly with $y = 0$, providing no additional information. To maintain clarity, the original U-loop signal is excluded.

A second-order polynomial function is used to create the trendline:

$$y = ax^2 + bx + c \tag{5.6}$$

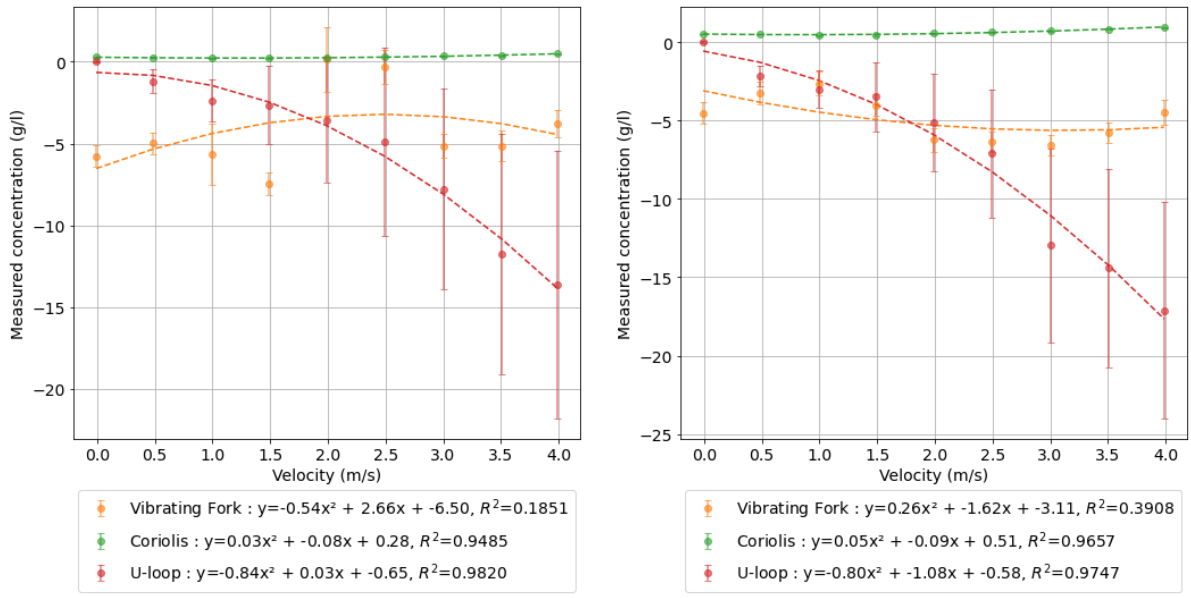

(a) A-series: Measured concentration per sensor

(b) E-series: Measured concentration per sensor

Figure 5.5: Measured concentration per sensor for A-series and E-series.

Vibrating Fork: This sensor exhibits a clear error for clean water, with no apparent relationship between concentration error and velocity. The trendline shows low R² values, indicating poor fit. However, the sensor consistently underestimates concentration across both the A and E series. The error is considered a characteristic of the sensor and is not compensated for in the concentration tests.

Coriolis Sensor: The Coriolis sensor displays a minor concentration error, primarily an offset. The trendline coefficients a and b are small, while c dominates, confirming the offset nature of the error. High R² values indicate a strong fit, and minimal deviation in the signal is shown by the lack of noticeable error bars. This small error is not compensated for.

U-loop: The U-loop sensor shows a clear relationship between velocity and concentration error, as addressed in Subsection 5.2.6. Higher velocities also correlate with increased standard deviation. This trend is observed across both test series.

5.3.3. Sediment tests

5.3.4. Coarse sediment (B-series)

The B-series involves coarse sediment (sand) with relatively large particles ($D_{50} \approx 168\,\mu$m). The sediment does not have cohesive or adhesive properties. The primary focus of this series is to observe how coarse particles settle in low-velocity zones, potentially forming a non-homogeneous mixture.

As discussed in Subsection 5.2.2, the B-series contains missing data points (NaN values) for some U-loop tests. These tests were excluded from the graphs and analysis. Since these data points are missing, it is more challenging to draw definitive conclusions about the U-loop data. Additionally, the coarse sediment introduces settling effects that complicate accurate concentration measurements.

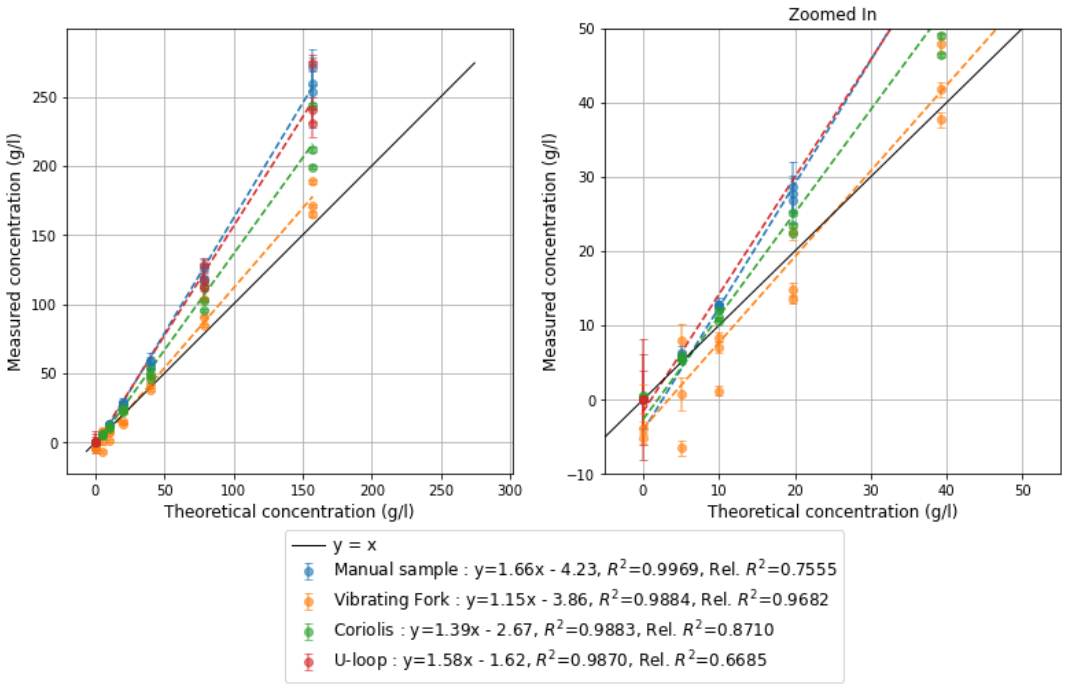

Figure 5.6: Coarse sediment (B-series): Measured concentration per method

The results indicate that the sensors generally overestimate the sediment concentration, especially at higher concentrations. At lower concentrations, the measured values align more closely with the ideal line. The difference between the theoretical and measured concentrations could come from the assumption that the sediment is homogeneously distributed throughout the system, which is likely not valid. The settling effect is visually confirmed by the clear concentration gradient in the hopper (Figure 5.9), where sediment visibly accumulates at the bottom.

Additionally, the larger particle size of the sediment may cause the flow to behave less like a homogenous mixture and more like a heterogenous flow. The analysis shows velocity-dependent effects on concentration measurement, which are discussed for each sensor below.

Manual Sample: The manual sampling method overestimates the concentration significantly, likely due to non-isokinetic sampling. This issue is addressed in subsequent series by adjusting the sample section design (see Section 4.8.1). It demonstrates high precision ($R^2 = 0.9969$) but very poor accuracy (rel. $R^2 = 0.7555$) (Figure 5.6). The standard deviation increases with higher concentrations, indicating reduced precision at higher sediment levels (Table A.1). Both the error and relative error plots actually increase with concentration (Figure 5.7). Velocity does not appear to influence the measured concentration significantly (Figure 5.8).

Vibrating Fork: The vibrating fork sensor performs relatively well compared to other methodologies, demonstrating medium precision ($R^2 = 0.9884$) and good accuracy (rel. $R^2 = 0.9682$) (Figure 5.6), with

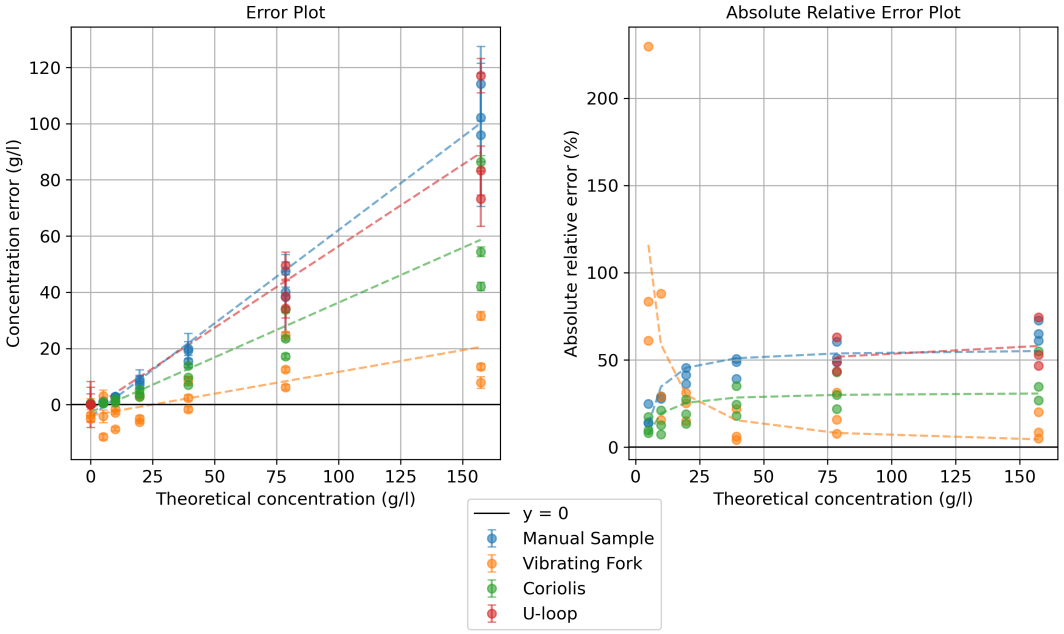

Figure 5.7: Coarse sediment (B-series): Error and relative error

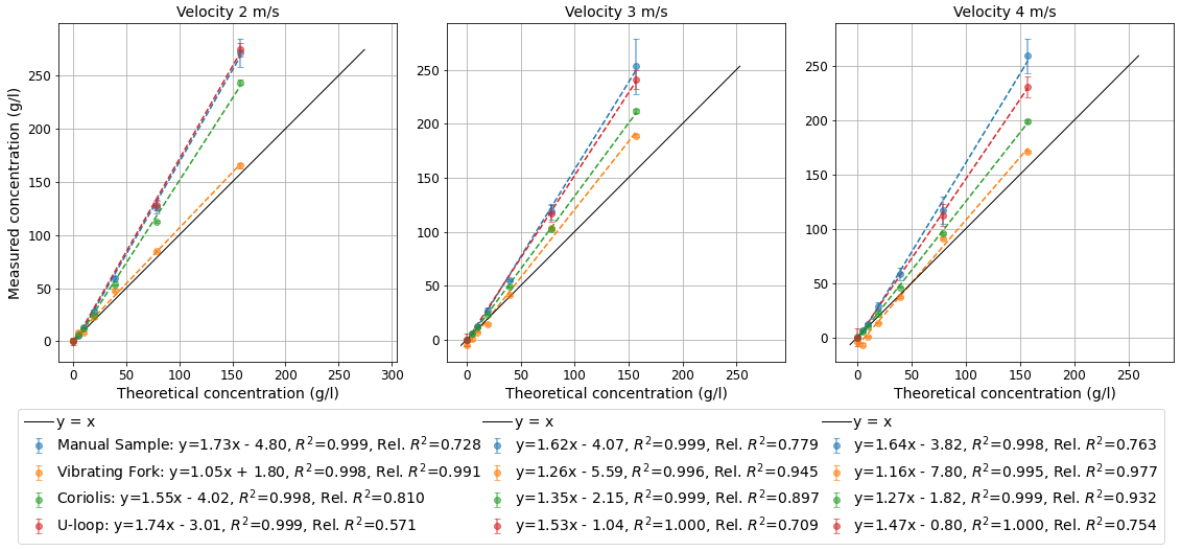

Figure 5.8: Coarse sediment (B-series): Measured concentration of the method per velocity

a medium standard deviation (Table A.1). The error and relative error plots show big values for low concentrations (Figure 5.7). However, its measured concentration is changes with velocity as seen in Figure 5.8, though no clear trend is observed. Despite its performance in this series, the vibrating fork's inconsistent results in other series suggest this observation may be coincidental.

Coriolis Sensor: The Coriolis sensor overestimates the concentration but performs reasonably well compared to other sensors, demonstrating medium precision ($R^2 = 0.9883$) and poor accuracy (rel. $R^2 = 0.8710$) (Figure 5.6). The standard deviation increases notably at higher concentrations, which indicates a decrease in precision for these tests (Table A.1). Both the error and relative error plots actually increase with concentration (Figure 5.7). Its measurements are influenced by velocity, with higher velocities resulting in better accuracy (Figure 5.8).

Figure 5.9: Coarse sediment (B-series): Solid separation in the hopper

U-loop: The U-loop sensor also overestimates the concentration. Demonstrating medium precision ($R^2 = 0.9870$) and poor accuracy (rel. $R^2 = 0.8710$) (Figure 5.6). The standard deviation is poor (Table A.1). The errors increases with concentration (Figure 5.7). Similar to the Coriolis sensor, its measurements are velocity-dependent, with higher velocities resulting in better accuracy (Figure 5.8). However, missing data points for the U-loop in this series limit the ability to draw conclusive observations.

The coarse sediment poses significant challenges for accurate concentration measurement due to settling effects and particle size. Future studies should focus on improving methods to account for non-homogeneous mixtures and mitigating the influence of velocity on measurements.

5.3.5. Medium Sediment (C-series)

This series uses medium sediment (silt) consisting of small silica particles ($D_{50} \approx 23\,\mu$m), which have neither cohesive nor adhesive properties. Compared to coarse sediment, this medium exhibits a lower tendency to settle, promoting a more homogeneous flow without flocculation or adhesion effects.

Overall, the data aligns more closely with the ideal line due to the smaller grain size and minimal settling. In the hopper, where the flow velocity is lowest, no visible concentration differences were observed between the top and bottom layers. If separation does not occur in the hopper, it is unlikely to occur elsewhere in the system.

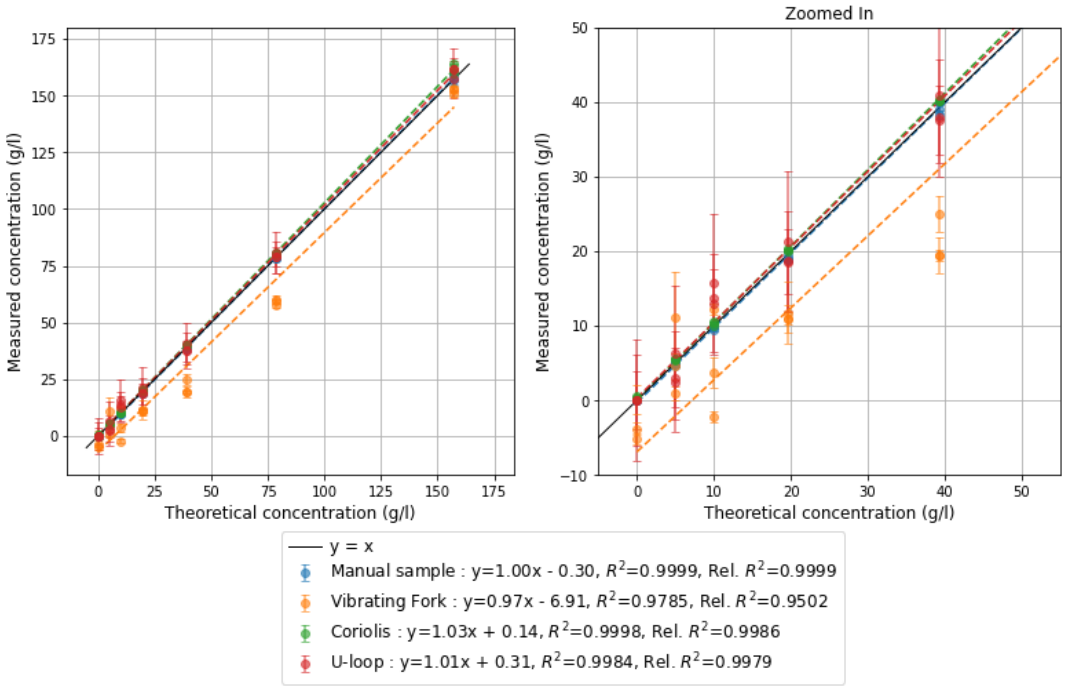

Figure 5.10: Medium Sediment (C-series): Measured concentration per method

Manual Sampling: This method achieves very high precision ($R^2 = 0.9999$) and very high accuracy (rel. $R^2 = 0.9999$), an impressive performance overall. The standard deviation is low (Figure 5.10). However, it is surprising that the standard deviation at the highest concentration is at least five times larger compared to the other concentrations, as shown in Table A.2. There are no notable deviations in the error or relative error (Figure 5.11), and velocity does not significantly affect the measurement (Figure 5.12).

Vibrating Fork: The vibrating fork significantly underestimates the concentration. The data points do not align well with the trendline, suggesting random variability in the sensor's measurements. The sensor exhibits low precision ($R^2 = 0.9785$) and low accuracy (rel. $R^2 = 0.9502$) (Figure 5.10). Across the entire concentration range, the sensor shows significant errors, with particularly large relative errors at lower concentrations (Figure 5.11). Additionally, the sensor occasionally measures negative concentrations, which is impossible.

Coriolis Sensor: The coriolis sensor performs well, demonstrating very high precision ($R^2 = 0.9998$) and high accuracy (rel. $R^2 = 0.9986$) (Figure 5.10). The standard deviation is small and consistent across all concentrations (Table A.2). Both the error and relative error plots show no unusual behaviour (Figure 5.11). Velocity does not appear to have any significant impact on the sensor's measurements (Figure 5.12).

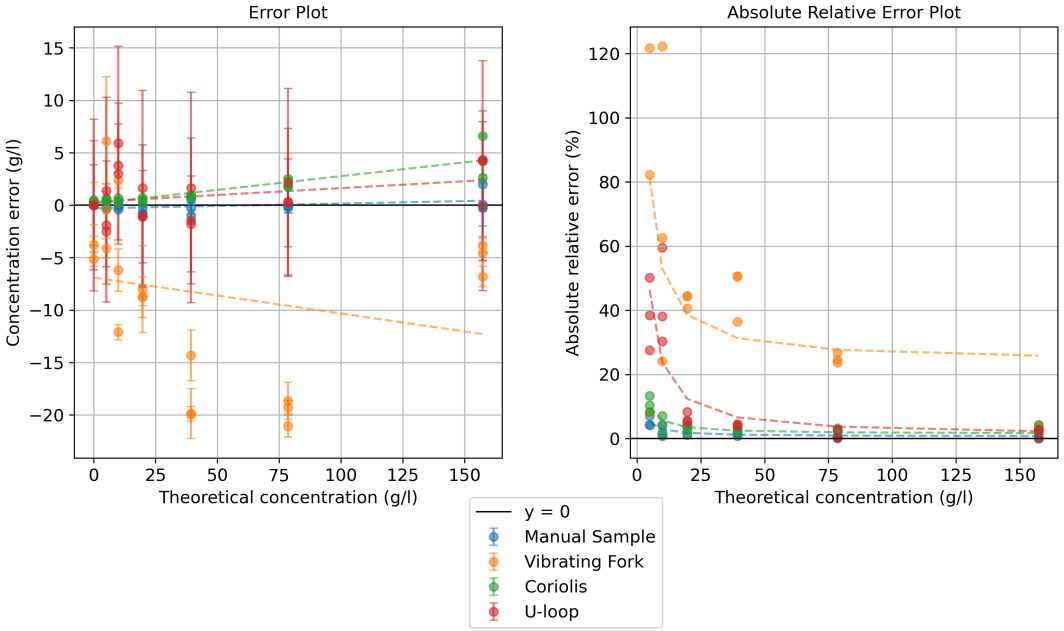

Figure 5.11: Medium Sediment (C-series): Error and relative error per method

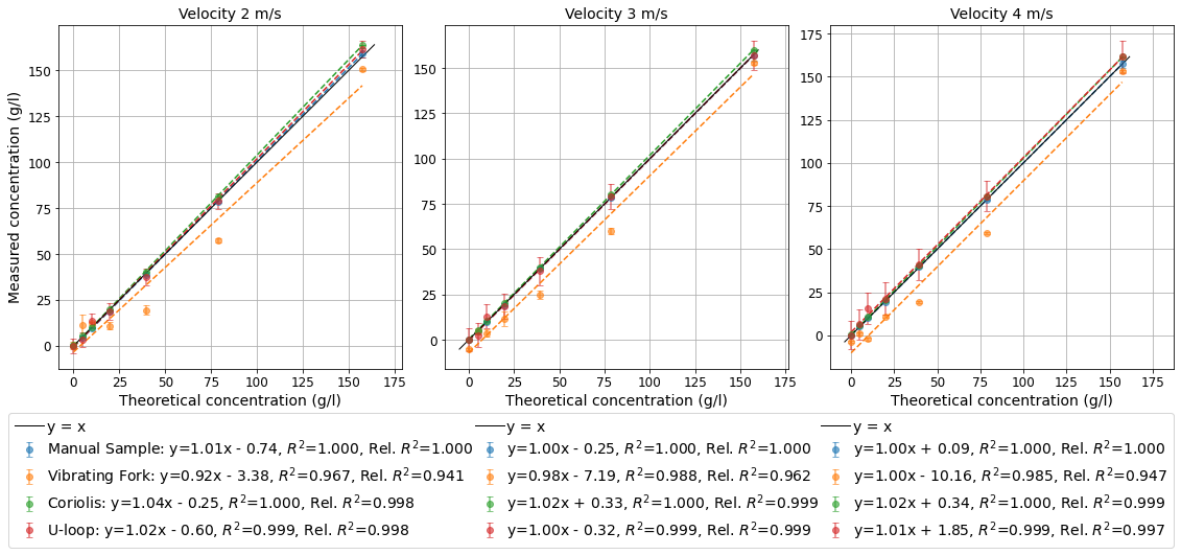

Figure 5.12: Medium Sediment (C-series): Measured concentration of the method per velocity

U-loop: The U-loop performs well, achieving good precision ($R^2 = 0.9984$) and good accuracy (rel. $R^2 = 0.9979$). Interestingly, the U-loop's trendline aligns better with the ideal line than the coriolis sensor's, but its relative R^2 is slightly lower due to greater variability in the mean data points (Figure 5.10). The standard deviation is poor, indicating more spread in the measurements (Table A.2). There is nothing significant in the error or relative error plots (Figure 5.11), and velocity does not appear to significantly affect the measurements (Figure 5.12).

5.3.6. Fine Sediment (D-series)

The D-series utilises fine sediment (clay) instead of the silica used in Series B and C. It features a very small particle size of $D_{50} \approx 1.3\,\mu$m. Clay exhibits both cohesive and adhesive properties, which can lead to floc formation and adhesion to sensor walls or tubing under certain flow conditions. Testing this series ensures that the measurement methods can accurately capture the behaviour of fine particles, where cohesive and adhesive interactions significantly affect concentration measurements and flow characteristics.

For the fine sediment, all methodologies demonstrate a good fit, as evidenced by the high relative R^2 values across all methods. Interestingly, all sensors trendlines intersect the ideal line, as seen more clearly in the error graph.

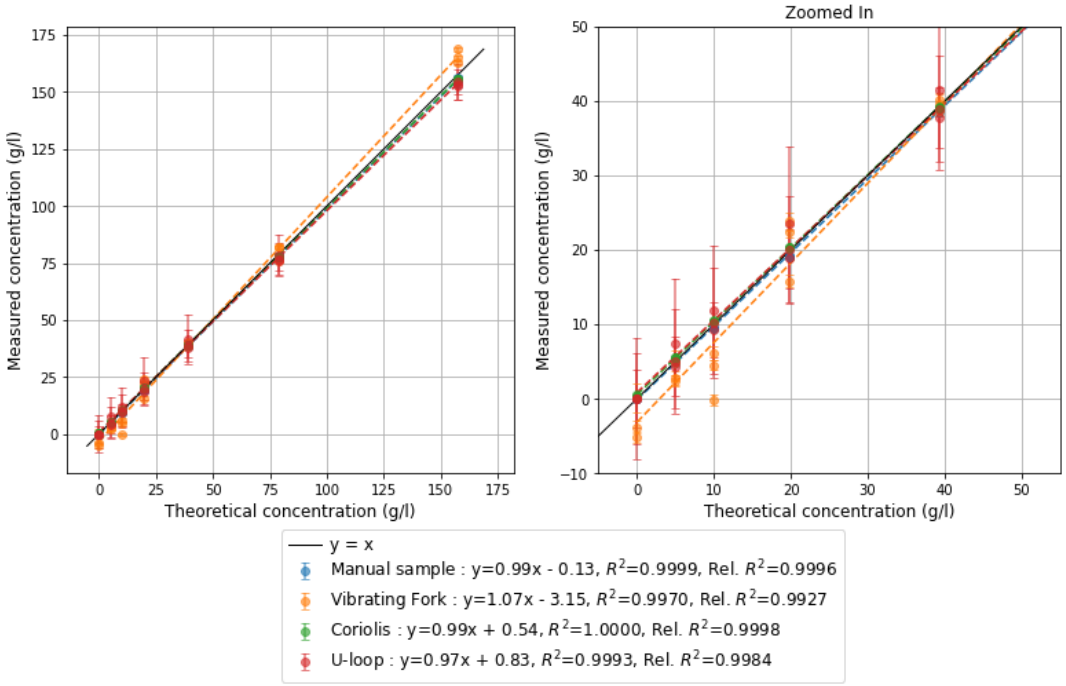

Figure 5.13: Fine Sediment (D-series): Measured concentration per method

Manual Sampling: This method performs exceptionally well, achieving very high precision ($R^2 = 0.9999$) and very high accuracy (rel. $R^2 = 0.9996$) (Figure 5.13). The standard deviation is low, although it increases noticeably at the highest concentration (Table A.3). The error and relative error plots do not reveal any unusual behaviour (Figure 5.14). Velocity does not appear to significantly affect the measurements.

Vibrating Fork: The vibrating fork estimates concentrations reasonably well, though its trendline crosses the ideal line. The sensor demonstrates decent precision ($R^2 = 0.9970$) and accuracy (rel. $R^2 = 0.9927$) (Figure 5.13). However, at lower concentrations, there is a larger relative error. Additionally, the sensor occasionally measures negative concentrations (Figure 5.14). At the highest concentration of 160 g/L, insufficient refreshment of the sample pocket was observed in the vibrating fork sample section, resulting in a stationary mixture at the end of the section. This could lead to a non-representative sample and potentially impact the sensor's ability to accurately measure concentration.

Coriolis Sensor: The coriolis sensor performs excellently, with very high precision ($R^2 = 1.0000$) and high accuracy (rel. $R^2 = 0.9998$). Interestingly, the trendline crosses the ideal line (Figure 5.13). The standard deviation is small and consistent across all concentrations (Table A.3). Both the error and relative error plots are acceptable, with no significant interest (Figure 5.14). Velocity does not appear to have any noticeable impact on the measurements (Figure 5.15).

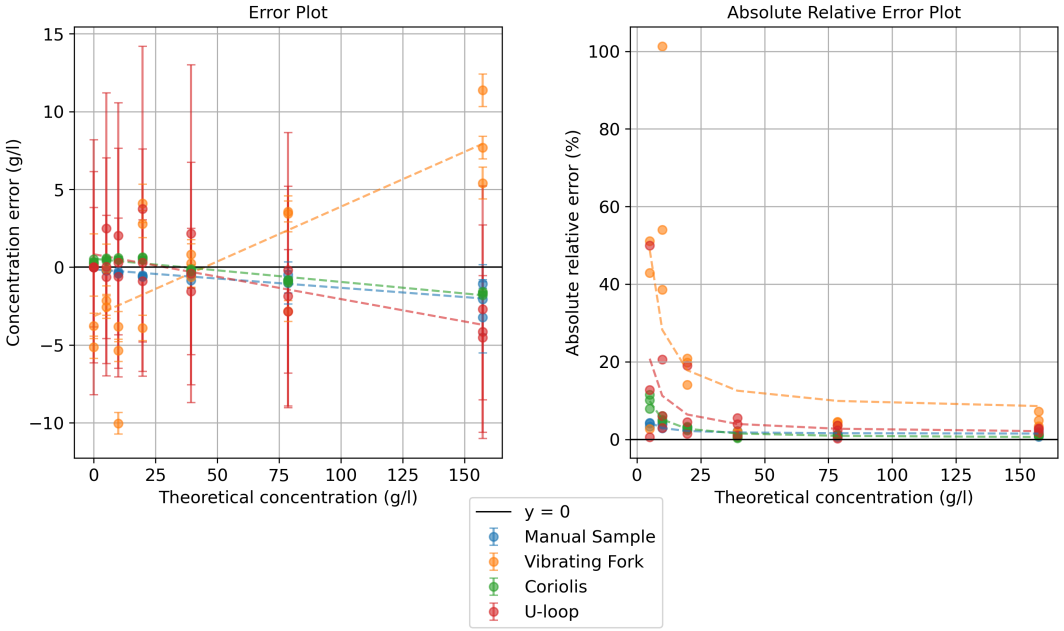

Figure 5.14: Fine Sediment (D-series): Error and relative error per method

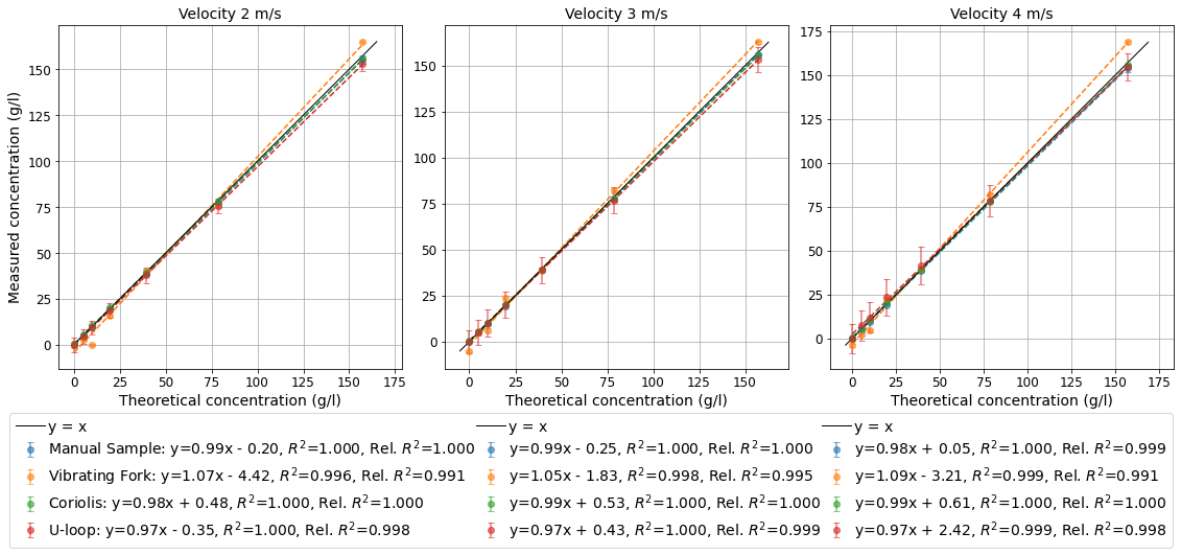

Figure 5.15: Fine Sediment (D-series): Measured concentration of the method per velocity

U-loop: The U-loop sensor exhibits high precision ($R^2 = 0.9993$) and high accuracy (rel. $R^2 = 0.9984$). Interestingly, its trendline also crosses the ideal line (Figure 5.13). However, the standard deviation is relatively poor (Table A.3). The error and relative error plots do not reveal any significant issues (Figure 5.14). Velocity effects are most pronounced in the 4 m/s test, where the R^2 value decreases, and the a-coefficient of the polynomial function (5.6) increases (Figure 5.15).

5.3.7. Deep Sea Sediment (F-series)

The final and most significant test series was conducted using deep-sea sediment, a type of clay. This material has a particle size distribution of approximately $D_{10} \approx 7.2\,\mu$m and $D_{50} \approx 11\,\mu$m. Deep-sea clay possesses cohesive and adhesive properties, which can vary depending on the presence of organic matter, biogenic particles, or other mineral components in the sediment. Evaluating sensor performance with this material provides valuable insights into realistic conditions for deep-sea mining operations, however nodule fines are excluded.

The results differ from those of the fine sediment tests, which was also conducted with clay. The data for deep sea sediment is more scattered than for medium sediment and fine sediment. Notably, manual sampling performed worse compared to the medium sediment and fine sediment. Another interesting observation is that the standard deviation for most methodologies is significantly higher during test f19, this is due to the air injection needed to unblock the manual sample tube, further explained in text 5.3.8.

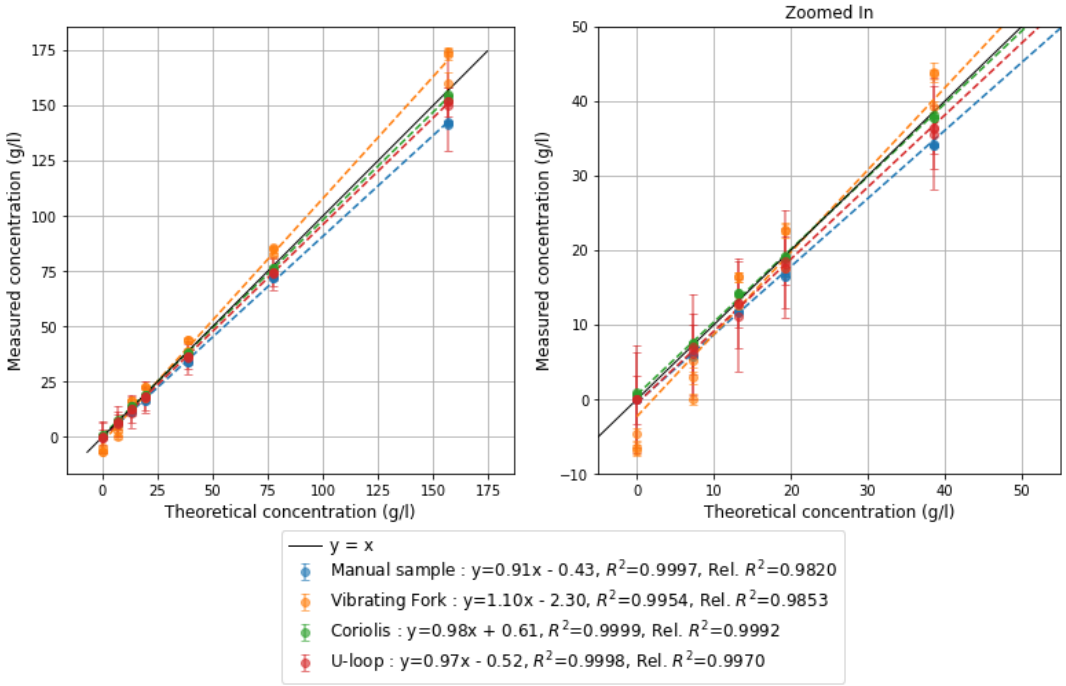

Figure 5.16: Deep Sea Sediment (F-series): Measured concentration per method

Manual Sampling: The performance of manual sampling is noticeably worse compared to coarse sediment and medium sediment. While it has high precision ($R^2 = 0.9997$), the accuracy is moderate (rel. $R^2 = 0.9853$)(Figure 5.16). The standard deviation is relatively low, but the error increases with concentration (Table A.4), even though the relative error remains stable (Figure 5.17). Velocity does not significantly affect the measurements (Figure 5.18). At the highest concentration of 160 g/L, the mixture became so viscous that it blocked the sample tube even when fully opened. Pressurised air was required to unblock the tube, after which it was left open continuously to prevent further blockages.

Vibrating Fork: The sensor performs moderately well, but the trendline crosses the ideal line. It exhibits medium precision ($R^2 = 0.9954$) and good accuracy (rel. $R^2 = 0.9853$) (Figure 5.16). However, the standard deviation is notably higher at the highest concentration, particularly during test f19 (Table A.4). The relative error is substantial at both low and high concentrations, and the sensor produces both positive and negative errors, crossing the ideal line (Figure 5.17). Additionally, it measures significant negative concentrations with clean water. Velocity affects the measurements, but no consistent positive or negative trend is observed (Figure 5.18). For the highest concentration of 160 g/L, the sample pocket experienced insufficient refreshment, leading to a stationary mixture at the end of the sample section. This non-representative sample may have affected the sensor's ability to measure accurately.

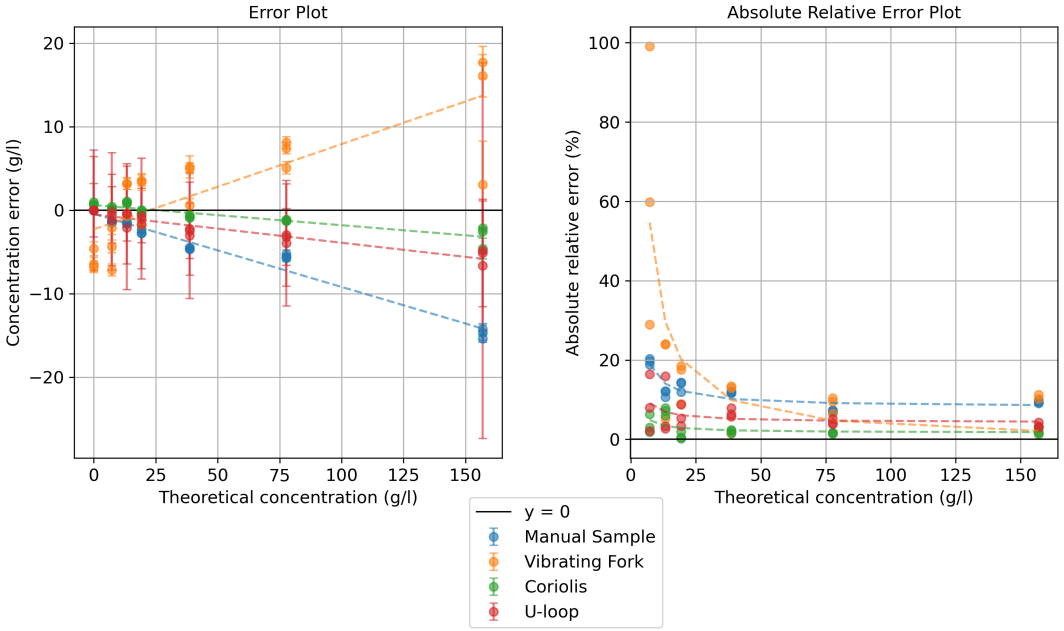

Figure 5.17: Deep Sea Sediment (F-series): Error and relative error per method

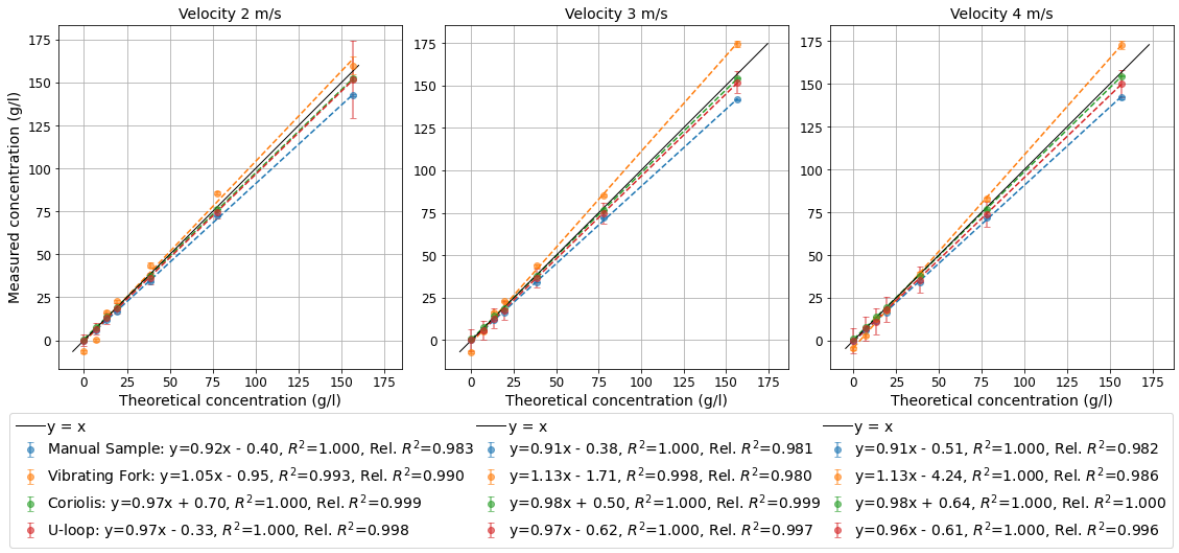

Figure 5.18: Deep Sea Sediment (F-series): Measured concentration of the method per velocity

Coriolis Sensor: This sensor performs exceptionally well, demonstrating very high precision ($R^2 = 0.9999$) and accuracy (rel. $R^2 = 0.9992$) (Figure 5.16). Interestingly, the trendline crosses the ideal line. The standard deviation is small and remains consistent across concentrations, except for test f19, where it is significantly higher (Table A.4). The error and relative error plots show no anomalies (Figure 5.17). The sensor's performance improves with higher velocity, as evidenced by an increase in relative R^2 (Figure 5.18).

U-loop: The U-loop sensor exhibits high precision ($R^2 = 0.9998$) and moderate accuracy (rel. $R^2 = 0.9970$) (Figure 5.16). However, its standard deviation is notably poor (Table A.4). The error and relative error plots show no significant deviations (Figure 5.17). A slight decrease in performance is observed with increasing velocity, as indicated by the relative R^2v(Figure 5.18).

5.3.8. Histogram and Time-series Analysis

Histogram

To better analyse the data, histograms were generated to display the distribution of data points for each methodology during the tests, the histograms can be seen in Appendix B. The x-axis represents the concentration in g/L, while the y-axis indicates the percentage of data points within each bin.

Note: The range of the concentration axis is not the same for all methodologies. More precise methodologies display smaller ranges.

On average, the Coriolis sensor demonstrates the highest precision, with a much narrower range compared to the other methodologies. Specifically, the range of the vibrating fork is approximately 10 times larger, and the U-loop's range is about 100 times larger. When analysing the histograms, it is evident that the data generally follow a normal distribution. Among the methodologies, the U-loop exhibits the most consistent adherence to a normal distribution, while the vibrating fork and Coriolis sensors display slight deviations.

The Coriolis sensor provides approximately 600 data points, significantly fewer than the vibrating fork and U-loop sensors, which each have about 6,000 data points. The smaller dataset for the Coriolis sensor is less likely to be a perfect normal distribution for the histograms.

Time-series

Time-series were created to observe the distribution of data points for each methodology throughout the duration of the test. These time-series help identify whether a methodology shows tendencies to respond consistently or variably to conditions that evolve during testing. Additionally, trendlines are included to visualise any systematic behaviour of the methodologies over time.

The time-series reveal that the sensors exhibit varying behaviours during the tests, although no clear trends are discernible. This conclusion is supported by Table 5.7, which presents the average slopes of the trendlines for each test series, and the average change in measured concentration over the duration of the test (5 min).

The vibrating fork sensor exhibits a low resolution for displaying concentration measurements. This is shown by the distinct steps between different concentration levels, with no intermediate data points. Consequently, the measurements will rounded up or down, potentially affecting the precision. However, this rounding does not impact the average concentration measurement, as the overall spread of measured concentrations is much larger.

During tests f19 and f20, pressurised air was used to unblock the sample tube of the manual sampling section. The moments when air was injected are clearly visible as disruptions in the time-series (Appendix C.21).

Table 5.7: Slopes of the time-series and differences over 5 minutes

Average Slope	**Vibrating Fork**	**Coriolis**	**U-loop**	**Velocity**
B	-0.01738	-0.00314	-0.00579	-0.00068
C	0.003196	0.000176	-0.00012	7.03E-06
D	0.00086	9.13E-05	-0.00027	9.35E-06
F	0.001028	0.000292	-0.00043	1.58E-05
All	-0.00307	-0.00065	-0.00165	-0.00016
Difference over 5 min (g/L)	**Vibrating Fork**	**Coriolis**	**U-loop**	**Velocity**
B	-5.214	-0.942	-1.737	-0.204
C	0.9588	0.0528	-0.036	0.002109
D	0.258	0.02739	-0.081	0.002805
F	0.3084	0.0876	-0.129	0.00474
All	-0.921	-0.195	-0.495	-0.048

Fourier transfer

To identify oscillatory effects in the system, a Fourier Transform was performed on the dataset. The Fourier Transform analyses frequencies ranging between a lower and an upper limit. The upper limit is determined by the Nyquist frequency:

$$f_{\text{Nyquist}} = \frac{1}{2T} = \frac{1}{2 \times 0.05} = 10\,\text{Hz},$$

where $T = 0.05\,\text{s}$ is the sampling interval.

The lower limit is governed by the duration of the test, which is 300 seconds. The corresponding minimum resolvable frequency is:

$$f_{\text{min}} = \frac{1}{\text{Duration}} = \frac{1}{300} \approx 0.0033\,\text{Hz}.$$

Thus, the Fourier Transform evaluates frequencies in the range $0.0033\,\text{Hz}$ to $10\,\text{Hz}$, capturing oscillations at various timescales within the system. The Fourier Transform results are plotted alongside the corresponding time-series data.

It is not possible to analyse how vibrations from different sensors and the pump affect each other, as these frequencies are significantly higher than the Nyquist frequency:

- Coriolis: $71\,\text{Hz}$,
- Vibrating fork: $975\,\text{Hz}$,
- Centrifugal pump: $25\,\text{Hz}$.

The objective was to identify density waves within the system, which typically have frequencies in the range $0.1\,\text{Hz}$ to $1\,\text{Hz}$. Density waves were especially anticipated for the coarse sediment. However, these effects were not observed. A peak around $3\,\text{Hz}$ was detected for the U-loop, but similar effects were not observed for other sensors. Notably, the peak did not shift with changes in velocity, concentration, or sediment type. The cause of this peak remains unclear.

Note: From the analysis of the time-series data and the Fourier Transform, it can be concluded that the tests performed represent a steady-state system.

Table 5.8: Statistical overview per velocity C, D, and F series (excluding coarse sediment, B-series)

Velocity (m/s)	Manual Sample	Vibrating Fork	Coriolis	U-loop
R²				
2	0.9999	0.9852	1.0000	0.9995
3	0.9999	0.9946	1.0000	0.9997
4	0.9999	0.9944	1.0000	0.9994
Rel. R²				
2	0.9943	0.9739	0.9986	0.9980
3	0.9935	0.9794	0.9995	0.9985
4	0.9938	0.9748	0.9994	0.9968
Average Std (g/L)				
2	0.452	1.531	0.110	4.737
3	0.348	1.292	0.062	6.640
4	0.380	0.927	0.049	8.494
Abs. Rel. Error (%)				
2	5.88	34.06	3.07	8.39
3	5.41	19.50	3.43	7.91
4	5.37	30.57	3.98	13.47

5.3.9. Effect of Velocity

The results of the B-series heavily influence the analysis, as shown in Table 5.9. To mitigate this influence, a separate table 5.8 excludes the coarse sediment tests (B-series) results. The following observations are made about the other sediments (C, D, and F series):

The Manual Sample shows a slight increase in accuracy with increasing velocity, as indicated by the improved relative R^2 and absolute relative error. The standard deviation remains relatively unaffected. Overall, the method performs slightly better at higher velocities.

The Vibrating Fork shows no significant correlation between accuracy and velocity. However, precision improves with higher velocities, as evidenced by increasing R^2 values and decreasing standard deviations. The sensor performs better with increased velocity.

The Coriolis Sensor exhibits a slight decrease in accuracy with velocity, as the absolute relative error increases slightly, although the relative R^2 improves. Precision improves with higher velocities due to lower standard deviations. Overall, the Coriolis sensor is only minimally affected by velocity changes.

The U-loop experiences a decrease in both accuracy and precision as velocity increases. The relative R^2 decreases, and the absolute relative error increases, likely due to higher shear forces at increased velocities. The standard deviation also increases, possibly due to more pronounced pressure shocks in the system. The U-loop performs worse at higher velocities.

Table 5.9: Statistic overview per velocity for coarse sediment (B-series)

Velocity m/s	Manual sample	Vibrating fork	Coriolis	U-loop
R^2				
2	0.9985	0.9979	0.9982	0.9986
3	0.9986	0.9956	0.9995	0.9998
4	0.9977	0.9954	0.9995	0.9999
Rel. R^2				
2	0.7276	0.9908	0.8097	0.5714
3	0.7792	0.9450	0.8969	0.7091
4	0.7632	0.9769	0.9317	0.7540
Average std (g/L)				
2	3.5773	1.4274	0.6040	4.9203
3	5.3220	1.1951	0.4867	7.5157
4	5.6818	0.8703	0.4334	9.3395
Abs. Rel. Error (%)				
2	44.75	21.05	33.10	68.69
3	38.19	32.53	21.69	50.97
4	43.59	62.91	15.89	45.05

5.3.10. Effect of Sediment Type

The performance of the manual sample, Coriolis, and U-loop methodologies shows clear differences between coarse sediment and other sediment types. These differences are clear across various statistical measures, as shown in Table 5.10. For the vibrating fork sensor, its performance with coarse sediment is comparable to its performance with other sediment types.

The Manual Sample experiences a significant decrease in accuracy when measuring coarse sediment and a moderate decrease for deep-sea sediment. This is reflected in the reduced relative R^2 and increased absolute relative error. The precision of the method improves from the coarse sediment to the deep sea sediment tests, likely due to increased operator experience, as evidenced by a reduction in the standard deviation. The poor performance with coarse sediment may stem from the sampling section design, which was updated after the coarse sediment tests (detailed in Section 4.8.1). The

results do not suggest a direct correlation between measurement performance and either particle size or the silica versus clay composition.

The Vibrating Fork improves its accuracy when switching from silica to clay. The absolute relative error is reduced by half, and the relative R^2 increases significantly. Precision also improves when using clay, as the R^2 values increase and the standard deviation decreases slightly. The sensor performs better with clay due to its adhesive and cohesive properties, which affect the mixture's behaviour compared to silica, which lacks these properties. Grain size does not appear to have a strong influence on the vibrating fork's performance.

The Coriolis Sensor shows improved accuracy with decreasing grain size. This trend is reflected in the increased relative R^2 and decreased absolute relative error, although a slight accuracy reduction is observed for fine sediment. Precision also improves with smaller grain sizes, as indicated by increased R^2 values and reduced standard deviation. Overall, the Coriolis sensor performs better with smaller grain sizes.

The U-loop similarly improves in accuracy as grain size decreases. Both the relative R^2 and absolute relative error generally improve with smaller grain sizes. Precision also increases, with higher R^2 values and lower standard deviation for finer sediment. The U-loop methodology performs better as particle size decreases.

In summary, methodologies generally perform better with smaller particle sizes. Smaller particles have reduced settling velocities, resulting in a more homogeneous mixture. This homogeneity ensures that the concentration at any given point is more representative of the overall mixture, thereby improving measurement accuracy.

Table 5.10: Statistic overview grouped by sediment type

Statistic	D_{50} (μm)	Manual Sample	Vibrating Fork	Coriolis	U-loop
R^2					
B coarse sediment	168	0.9969	0.9884	0.9883	0.9870
C medium sediment	23	0.9999	0.9785	0.9998	0.9988
D fine sediment	1.3	0.9999	0.9970	1.0000	0.9993
F deep sea sediment	11	0.9997	0.9954	0.9999	0.9998
rel. R^2					
B coarse sediment	168	0.7555	0.9682	0.8710	0.6685
C medium sediment	23	0.9999	0.9502	0.9986	0.9979
D fine sediment	1.3	0.9996	0.9927	0.9998	0.9984
F deep sea sediment	11	0.9820	0.9853	0.9992	0.9970
Average Std (g/L)					
B coarse sediment	168	4.8604	1.1643	0.5080	7.2585
C medium sediment	23	0.5670	1.6272	0.0768	6.7668
D fine sediment	1.3	0.4137	0.9647	0.0334	6.6572
F deep sea sediment	11	0.1996	1.1584	0.1105	6.4463
Abs. Rel. Error (%)					
B coarse sediment	168	42.18	38.83	23.56	54.91
C medium sediment	23	2.10	42.92	4.17	15.82
D fine sediment	1.3	2.38	20.98	3.46	7.87
F deep sea sediment	11	12.18	20.22	2.85	6.08

5.3.11. Effect of Concentration

As discussed in Subsection 5.3.4, the relative error in the B-series is substantial and increases with higher concentrations, as shown in Table 5.12. This trend is the opposite of what occurs in the other test series (Table 5.11). Detailed results for each test series are provided in Table D.1 in the appendix.

The combined results of the C, D, and F series (Table 5.11) reveal a general trend where the absolute relative error decreases with increasing target concentration. However, at the highest concentration, the absolute relative error slightly increases, which is unexpected. Initially, this was attributed to a non-homogeneous regime; however, the volumetric concentration is only 6%, which is insufficient for such behaviour given the small particle size. Furthermore, this increase in absolute relative error occurs not only in the clay-based deep sea sediment tests but also in the silica-based medium sediment tests, suggesting another underlying factor.

In contrast, the results of the B-series (Table 5.12) show that the absolute relative error increases with higher concentrations for the manual sample, Coriolis, and U-loop methods. This is contrary to the behaviour observed in the other test series and was not anticipated.

When examining the effect of concentration on standard deviation, there are two distinct observations. For the vibrating fork and U-loop methods, the standard deviation remains relatively constant regardless of the target concentration. In contrast, the manual sampling and Coriolis methods exhibit a linear relationship between standard deviation and target concentration. A more detailed analysis reveals that this linear relationship is primarily influenced by the coarse sediment test and the fine sediment tests at a target concentration of 160 g/L. For the other test series, the standard deviation for these methods appears independent of the target concentration. Additional details are presented in Table 5.13.

Table 5.11: Average absolute relative error for the C, D, and F series (excluding coarse sediment, B-series).

	Absolute Relative Error (%)			
Target Concentration (g/L)	**Manual Sample**	**Vibrating Fork**	**Coriolis**	**U-Loop**
5	9.56	55.19	8.08	22.87
10	5.77	50.66	5.54	19.95
20	6.50	25.45	2.08	6.84
40	4.99	18.87	1.55	4.75
80	2.77	12.67	1.76	2.53
160	3.75	5.41	1.96	2.59

Table 5.12: Average absolute relative error for the coarse sediment (B-series).

	Absolute Relative Error (%)			
Target Concentration (g/L)	**Manual Sample**	**Vibrating Fork**	**Coriolis**	**U-Loop**
5	17.59	124.73	11.69	
10	28.61	44.17	13.63	
20	41.05	23.76	19.90	
40	46.26	10.76	25.83	
80	53.38	18.35	31.54	51.82
160	66.18	11.21	38.76	57.99

Table 5.13: Standard deviation of measurements across different target concentrations and methods.

	Standard Deviation (g/L)			
Target Concentration (g/L)	**Manual Sample**	**Vibrating Fork**	**Coriolis**	**U-Loop**
0	0.000	1.075	0.028	5.946
5	0.236	1.646	0.052	6.125
10	0.210	0.872	0.064	6.254
20	0.827	1.259	0.085	6.437
40	1.008	1.191	0.138	6.670
80	2.563	0.930	0.275	6.627
160	5.727	1.626	0.634	8.529

5.3.12. Performance of the different methodologies

By combining all the findings from the analyses of the test results, it can be concluded that the Coriolis sensor performed the best among all the continuous measurement methodologies tested. The Coriolis sensor demonstrated performance comparable to, and in some cases better than, the manual sampling method, which was the original method.

Table 5.14 summarises the average statistical values for all tests, highlighting the strong performance of the Coriolis sensor. It exhibits the best standard deviation and absolute relative error among the tested methodologies. However, the R^2 and relative R^2 values are not the highest, primarily due to the Coriolis sensor's weaker performance during the coarse sediment tests.

The overall findings suggest that the Coriolis sensor is highly suitable for continuous concentration measurements, showing consistent accuracy and precision across various test conditions, except when dealing with coarse sediment in the B-series.

Table 5.14: Statistic overview average of all test

	Manual sample	Vibrating fork	Coriolis	U-loop
R²	0.9991	0.9898	0.9970	0.9962
rel. R²	0.9343	0.9741	0.9672	0.9155
average std (g/L)	1.5102	1.2286	0.1822	6.7822
Abs. Rel. Error (%)	14.71	30.74	8.51	21.17

5.4. Discussion

5.4.1. Scaling Issues

The experimental setup used in this study is smaller and simpler than the systems employed in real deep-sea mining operations. Industrial systems utilise larger pipes, where turbulence is greater near the walls, leading to relatively less mixing. This could result in non-homogeneous sediment distribution which would affect sensor performance in other ways.

For all sensors, a bypass from the main flow would likely be implemented, where the sensor would conduct its measurements. This would require significant attention to ensure that the concentration in the bypass is representative of the full flow. Ensuring a fully homogeneous main flow and applying isokinetic sampling is crucial, particularly for accurately measuring nodule fines.

5.4.2. Salinity

This study used fresh water instead of salt water, which is normal in deep-sea mining. The mixture density in the real situation in salt water is denser (1032–1074 kg/m³) than fresh water, and this could affect how well the sensors measures sediment concentration. However, the density range tested in this thesis (998–1098 kg/m³) exceeds the range found in real situation, so the sensors should still work well. For the sensors to change from fresh to salt water, only the water density needs to be changed to calculated the concentration with salt water.

The method most affected by salinity is manual sampling. Salt in the water can be absorbed by the filter, which could make it seem like there is more sediment than there actually is. This error can be minimized by following strict protocols, such as those described in [20].

5.4.3. Theoretical Concentration

The theoretical concentration assumes that sediment is evenly distributed in the system. In reality, this is not always true, and several factors can cause errors:

- **Leaks:** If a mixture leaks from the system, it can affect the concentration in the setup. In this study, any leaked mixture was collected and added back to the system to minimize this issue.
- **Sediment build-up or water pockets:** Sediment might collect in low-flow areas or water pockets might form, leading to uneven concentrations in the pipes.

- **Hopper Settling:** In the hopper, where flow velocity is lower, sediment can settle to the bottom. This was observed in the coarse sediment and is shown in Figure 5.9. Settled sediment can re-enter the pipes, increasing concentration in the pipes and reducing concentration in the hopper.
- **Non-homogeneous flow:** In pipes, sediment concentration might be higher at the bottom due to settling, or it might vary between upward and downward flows, as shown in Figure 4.9.

Despite these challenges, the theoretical concentration was close to the true concentration in most cases (error $\approx$ 0.3 % as calculated in subsection 4.10). The coarse material was an exception, likely due to the rapid settling of coarse sediment.

Coarse sediment (B-series) correction theoretical concentration

In the hopper, where flow velocity is lower, sediment can settle to the bottom. This was observed in the coarse sediment test and is shown in Figure 5.9. Settled sediment can re-enter the pipes, increasing concentration in the pipes and reducing concentration in the hopper.

To compensate the theoretical concentration for this error, it is assumed sediment entering the hopper will not flow upwards and be homogenously distributed in the lower half of the hopper. The volume above the entering pipe will be assumed to be consiting of water. This volume calculated to be equal to 12.65 l. This water volume is substracted from the total water volume and the theoretical concentration is recalculted.

Table 5.15: Comparison of Old and New Theoretical Concentrations.

Target Concentration (g/L)	5	10	20	40	80	160
Old Theoretical Concentration (g/L)	5.001	9.883	19.622	39.074	77.996	155.932
New Theoretical Concentration (g/L)	6.042	11.936	23.681	47.085	93.698	186.190
Change (%)	20.82	20.78	20.68	20.50	20.13	19.40

Table 5.16: Statistic overview for B coarse sediment ($D_{50} = 168\,\mu$m).

Statistic old	Manual Sample	Vibrating Fork	Coriolis	U-loop
R^2	0.9969	0.9884	0.9883	0.9870
Rel. R^2	0.7555	0.9682	0.8710	0.6685
Average Std (g/L)	4.8604	1.1643	0.5080	7.2585
Abs. Rel. Error (%)	42.18	38.83	23.56	54.91
Statistic new				
R^2	0.9966	0.9886	0.9881	0.9868
Rel. R^2	0.8769	0.9801	0.9592	0.8422
Average Std (g/L)	4.8604	1.1643	0.5080	7.2585
Abs. Rel. Error (%)	20.05	36.09	8.58	30.43

The result show a clear improvement to the statistical parameters, only to the accurcay parameters which makes sense due to the fact that the theoretical concentration is changed and the measured concentration is constant. This shows that part of the error for coarse sediment is due to short comings of the setup, because of sediment settling in the hopper.

5.4.4. Effect of Velocity

The effect of velocity on sensor performance varied significantly across the tested methodologies. Higher velocities tended to improve mixture homogeneity, particularly for coarse sediments, reducing errors in measured concentration. Effect of velocity are not the same across all test, there is a clear difference between the coarse sediment and the other test series. Which shows, this improvement was not universal:

- **Manual Sampling:** Performance improved slightly with increased velocity as higher velocities reduced sediment settling, leading to more representative samples. The effect, however, was

minimal, and the method remained largely unaffected by velocity changes. For the coarse sediment the affect of isokenetic sampling which increases its measured concentration with velocity. And a better mixing in the setup due to increased velocity which decreases the concentration. These actually cancel out, which can be seen in table 5.9

- **Vibrating Fork Sensor:** Precision increased with velocity due to reduced sedimentation effects. However, accuracy remained relatively poor and random, suggesting that velocity alone cannot overcome the sensor's inherent limitations.
- **Coriolis Sensor:** The sensor demonstrated consistent performance across different velocities, with only minor decreases in accuracy at higher velocities. This highlights its robustness across flow regimes.
- **U-Loop:** The methodology was significantly affected by velocity, with accuracy decreasing as velocity increased. This was likely due to increased shear forces and pressure shocks, introducing errors into the measurements.

5.4.5. Effect of Sediment Type and Grain Size

The type and grain size of sediment had a clear impact on sensor performance, as smaller particles tend to create more homogeneous mixtures, reducing errors. A smaller grain size also tends to follow the flow better thus following the vibrations of the Coriolis and vibrating fork sensor better, which is indicated by a lower Stokes number:

- **Coarse Sediments (e.g., Sand, $D_{50} \approx 168\,\mu$m):** Coarse sediments caused overestimation of concentration in most methods due to settling and uneven distribution in low-velocity areas. The large, heavy particles settled quickly, leading to uneven mixtures. This was especially visible in the hopper, where sediment concentration was higher at the bottom than at the top, as shown in Figure 5.9. Due to this settling, the sediment re-entered the pipes quicker than normal, causing higher concentrations in the pipes than in the hopper. In Figure 5.9, the performance of the Coriolis sensor and the U-loop improved as velocity increased, supporting the idea that higher flow speeds help keep the sediment better mixed. This shows that maintaining higher velocities is important to reduce settling and improve measurement accuracy for coarse sediments. The Stokes number for coarse sediment is relatively high, indicating significant particle inertia, which affects the measurement accuracy of the Coriolis and vibrating fork sensors. While the exact extent of the error is not fully quantified, this explains the larger deviations observed in measurements for coarse sediment.
- **Medium Sediments (e.g., Silt, $D_{50} \approx 23\,\mu$m):** Medium sediments showed improved performance compared to coarse sediments. The smaller grain size reduced settling and promoted a more homogeneous mixture, leading to better accuracy and precision for most sensors. The absence of cohesive or adhesive properties simplified the flow behaviour. The Stokes number for medium sediment remains significant for the vibrating fork sensor, indicating that particle inertia still plays a role in measurement error. While the exact extent of the impact is not quantified, it contributes to the observed measurement errors for medium sediment.
- **Fine Sediments (e.g., Clay, $D_{50} \approx 1.3\,\mu$m):** Fine sediments provided the best results for most sensors. The small particle size minimized settling, creating a highly homogeneous flow. However, cohesive and adhesive properties introduced by clay did not show any negative effect on the performance of the methodologies. The Stokes number for fine sediment is determined to be negligible, meaning particle inertia does not significantly influence the measurement process.
- **Deep-Sea Sediments (e.g., Clay, $D_{50} \approx 11\,\mu$m):** Deep-sea sediments presented unique challenges due to their mixed composition, including organic matter and biogenic particles. While the adhesive and cohesive properties did not seem to affect performance for fine sediments, they could influence the methodologies' ability to measure concentration accurately. The Stokes number for deep-sea sediment is also negligible, suggesting that particle inertia does not significantly impact measurement accuracy.

In general, a smaller grain size results in a better performance looking at the other sediment types, but the deep sea sediment does not completely fit into this trend.

Adhesion and cohesion properties, which are present in clay sediment but not in silica sediment, showed no significant effect in the results. Therefore, it is determined that these properties do not impact the ability of the different sensors to measure concentration.

5.4.6. Effect of Concentration

The effect of sediment concentration on measurement performance showed different patterns depending on the type of sediment and test conditions. In general, for most test series (C, D, and F), increasing sediment concentration improved measurement accuracy. As most methods have accuracy defined in absolute value in (g/L) and not a percentage. As the concentration increased, the relative error reduces for most methods. This trend is shown in Table 5.11. However, at the highest concentration of 160 g/L, there was a slight increase in the absolute relative error. This unexpected result might be due to changes in the flow behavior, such as localized sediment clustering or increased viscosity, but these effects were not significant enough to really effect the accuracy of the mythologies.

For the B-series with coarse sediments, the opposite trend was observed, as shown in Table 5.12. In this case, the absolute relative error increased with higher concentrations. This was likely caused by the fast settling of the coarse sediment, which led to uneven distributions within the setup. The non-homogeneous nature of the mixture in this series made it difficult for methods to provide accurate measurements, especially at higher concentrations where the settling effect was more pronounced.

The standard deviation of measurements also showed different patterns per methodology. For methods like the vibrating fork and U-loop, the standard deviation remained consistent regardless of the concentration, indicating that their precision was not affected by the sediment load. On the other hand, for methods like the manual sampling and Coriolis sensor, the standard deviation appeared to increase linearly with the concentration. However, further analysis revealed that this was mainly due to the results of the coarse sediment and the fine sediment at 160 g/L. For other tests, the standard deviation was generally independent of the concentration, as seen in Table 5.13.

Overall, the results suggest that higher sediment concentrations generally lead to better accuracy, except for coarse sediments where settling and uneven distribution significantly affect measurements. The standard deviation analysis indicates that while some methods are influenced by concentration, others maintain stable precision regardless of concentration.

5.4.7. Effect of Temperature

Temperature primarily affected water density, which influenced the mixture density. But when converting the mixture density to concentration, this effect of temperature on the concentration measurement was canceled out. Temperature increased during testing due to pump activity. Further effects could not be found, the slopes of the time-series in Table 5.7, does not show a clear trend that the methods performance are influenced over time.

5.4.8. Sensor Performance

Vibrating Fork Sensor

The vibrating fork sensor had several issues. It needed frequent manual calibration, which was done in clean tap water, which was time-consuming and prone to errors. The sensor also struggled to measure low concentrations accurately and sometimes recorded negative values, which is impossible.

The sample section caused additional problems. At the highest concentrations (160 g/L) with clay sediment, the sample section clogged and did not refresh properly, leading to non-representative samples.

U-Loop Methodology

The U-loop method required significant corrections to its raw data, making it less practical for use in the field. The method was sensitive to flow velocity and pipe design, with bends and diameter changes affecting measurements. Placing the measurement point farther from bends and avoiding diameter changes could reduce these effects.

The need for extensive corrections also limits the U-loop's reliability as a plug-and-play system. While it performed well under certain conditions, it is an ideal measurement method.

Manual Sampling

Manual sampling performed well in most cases but had problems with coarse sediment. The original sample section design caused sampling errors, but the design was improved after the coarse sediment test (B-series). Unfortunately, the coarse sediment tests were not repeated with the improved setup, so its effectiveness remains unverified. It is ofcourse also manual process to prone to human mistake. Manual sampling is reliable in many situations but requires careful design and protocol, but it is clearly not a flawless method.

Coriolis

This study shows that the Coriolis sensor is the best option for measuring sediment concentration in deep-sea mining operations. It worked well across different sediment types, flow velocities, and concentrations. However, challenges with coarse sediment in the B-series suggest that further testing is needed to confirm its reliability under these conditions.

6

Conclusion

This study investigated four methods for measuring sediment concentration in water-based mixtures: *manual sampling*, *vibrating fork*, *Coriolis sensor*, and *U-loop*. The tests evaluated these methods under various flow velocities (2–4 m/s), sediment types (sand, silt, clay, and deep-sea clay), and concentrations (5–160 g/L). This conclusion summarizes the findings while addressing the research questions.

Sub-question 1: What are the material properties of the sediment and the flow conditions for deep-sea mining operations?

The material properties of the sediment and flow conditions in deep-sea mining operations are characterized by several key factors (see Chapter 2:

Sediment and Mixture Properties

The return flow consists of a mixture of clay and nodule fines. The main characteristics of the sediment are as follows:

- **Sediment Types:** The clay present in the return flow is siliceous clay-ooze with a grain density of 2500 kg/m³. Polymetallic manganese nodules, degraded during the riser process and dewatering plant operations, have a specific density of 3460 kg/m³. The return flow is estimated to contain a 50/50 volume ratio of clay and nodule fines.
- **Grain Size:** The clay particles range is 11 ± 3 µm, with most particles below 11 µm. For nodule fines, a size range of up to 150 µm is expected in industrial operations.
- **Concentration:** The concentration in the return flow is estimated to range from 10 to 75 g/L, with corresponding mixture densities varying between 1031.55 kg/m³ and 1074.11 kg/m³. The concentration consists of clay and nodule fines, and concentration directly affects the mixture density.

Flow Conditions

The flow in the return pipe exhibits the following characteristics:

- **Flow Velocity:** The return flow velocity ranges from 2–4 m/s. This ensures a turbulent regime, maintaining suspension of smaller particles. Higher velocities reduce settling and promote homogeneity, especially important for coarser sediments (nodule fines).
- **Flow Regime:** The Reynolds number for the flow is approximately $4.4 \cdot 10^5$, indicating turbulent flow. The Durand Froude number calculation suggests that the deposit limit velocity is 0.93 m/s, far below the operating velocities, confirming that the flow regime is in suspension for particle sizes at least up to 200 µm.

The return flow consists of a complex mixture of fine clay and nodule fines with varying grain sizes. The flow operates in a turbulent regime, ensuring homogeneity for smaller particles but requiring careful management of flow velocity to minimize settling for coarser materials. Sediment properties, particularly grain size, density, and flocculation, significantly influence the behavior of the flow and the accuracy of concentration measurements.

Sub-question 2: What are the existing concentration measurement methodologies, and what are their limitations?

Subsub-question 2a: What types of methodologies are available for measuring suspended sediment concentrations?

A range of different measurement methodologies were found to be possible for the application of this thesis and were evaluated in section 3. The methodologies were evaluated against criteria such as accuracy, range, spatial and temporal resolution, safety, cost, and impact on the flow.The optical, acoustic, conductivity, and radioactive source sensors were determined to be unsuitable for the application of this thesis due to limited range, low accuracy, or safety concerns. Promising alternatives were further investigated and tested in the test setup these include the U-loop, Coriolis, and vibrating fork sensors.

Subsub-question 2b: What is the achievable accuracy of concentration measurement methodologies under deep-sea mining flow and sediment conditions?

The four methodologies tested have different strengths and limitations (see Chapter 5.3:

- **Coriolis Sensor:** This method provided the best overall performance with high accuracy and precision for medium and fine sediments. It was largely unaffected by flow conditions, except during the coarse sediment tests (B-series). It consistently achieved accuracy within 2–10% of theoretical concentrations. Taking the performance per methodology of all tests except the coarse sediment (B-series), which involve finer sediments representative of deep-sea sediment, the Coriolis sensor achieved the highest accuracy, with absolute relative errors of 3.5%. For the B-series, which involves coarser sediment more representative of nodule fines, the Coriolis sensor still achieved the highest accuracy, but with a higher absolute relative error of 23.6
- **Manual Sampling:** Commonly used as a reference method, manual sampling performed well for smaller particles but exhibited significant limitations with coarse sediment due to settling and non-representative sampling. While it can achieve accuracy comparable to the Coriolis sensor under ideal conditions, its reliability is compromised by the potential for human error. Included in the tests as the current industry standard, it serves as a benchmark for comparison with other sensors. Manual sampling clearly demonstrated its constraints during this study, particularly when dealing with coarse sediment. In all tests except for the coarse sediment (B-series), manual sampling was accurate, with absolute relative errors of 5.5%. However, for the coarse sediment (B-series), its absolute relative errors increased significantly, ranging between 40–50%.
- **U-loop:** The U-loop required significant post-processing (pressure and velocity corrections) to achieve acceptable accuracy. Its standard deviation was the highest among all methods, and it performed poorly with coarse sediment. For all tests except the coarse sediment (B-series), its absolute relative errors of 5–20%. For the coarse sediment (B-series), the errors were even higher 54.91%.
- **Vibrating Fork:** This method had the poorest accuracy and struggled at low concentrations (often recording negative values). Its results were less affected by sediment type but lacked the precision required for reliable measurements. Similar to the U-loop, the vibrating fork sensor showed high absolute relative errors, often exceeding 20% in tests across all tests.

Sub-question 4: How do sediment properties (e.g., size, adhesion, and cohesion) affect the performance of the concentration measurement methodologies?

Sediment properties such as particle size, shape, and material composition significantly influenced sensor performance. Coarse sediment caused overestimations due to sediment settling in the hopper, resulting in lower concentrations in the hopper and higher concentrations in the pipes. Finer sediments, including silica and clays, produced more uniform mixtures and better measurement accuracy across all methods. The Stokes number also decreases with grain size. Generally, smaller grain sizes result in better performance when compared to other sediment types, although deep-sea sediment does not completely follow this trend.

Adhesion and cohesion properties, which are present in clay sediment but not in silica sediment, showed no significant effect in the results. Therefore, it is determined that these properties do not impact the ability of the different sensors to measure concentration.

Sub-question 5: How do flow and mixture properties (e.g., velocity, concentration, temperature) influence the performance of the concentration measurement methodologies?

The effect of sediment concentration on measurement performance varied depending on the type of sediment and test conditions. In general, for most test series (C, D, and F series), increasing sediment concentration improved measurement performance, as shown in Table 5.11. However, for coarse sediment (B-series), the opposite trend was observed, the absolute relative error increased with higher concentrations, as shown in Table 5.12.

The effect of velocity on sensor performance varied significantly across the tested methodologies. Higher velocities tended to improve mixture homogeneity, particularly for coarse sediments. However, the impact of velocity was not consistent across all tests or methodologies.

Temperature influenced water density but had no significant impact on concentration measurements, as this effect was cancelled out during conversion from density to concentration. No clear trend in sensor performance over time was observed, as shown in Table 5.7.

Research Question: How could low concentrations of suspended sediment in the range of 10-75 g/L in a flow accurately be measured?

Suspended sediment concentrations ranging from 10 to 75 g/L can be measured accurately using a Coriolis sensor, which has demonstrated superior accuracy and precision across various flow conditions and concentration levels in this study. While the sensor has shown no issues detecting finer sediment like deep-sea sediment, it may encounter slight difficulties in accurately measuring coarse sediment, such as nodule fines. Sensor performance for coarse sediment could further be improved and verified by theoretical concentration improvements as discussed in subsection 5.4.3. Its ability to directly measure density and convert this into sediment concentration with minimal calibration or correction makes it highly reliable for continuous monitoring in operational environments.

Recommendations

6.1. Improvements to Experimental Setup

Flow Improvements

To address the challenges encountered during tests with coarse sediment, particularly its tendency to settle and create an uneven distribution throughout the setup, improvements to the mixing process in the hopper are recommended. One potential solution is the addition of a stirring mechanism to enhance flow velocity within the hopper, thereby promoting a more homogeneous sediment mixture.

Improvement to the DAC

If the tests were to be repeated, it is recommended to use a single data acquisition system (DAC) instead of two. Considerable effort was required to match the data from the two different systems. Two separate systems were utilised because the Coriolis sensor was incompatible with the LabVIEW interface, as LabVIEW uses a 4–20 mA signal, whereas the Coriolis sensor communicates via an RS-485 signal. Using a unified system would eliminate these challenges.

- The two systems operated at different sampling frequencies. The LabVIEW system required a minimum sampling interval of 50 milliseconds, while the Pro-Link system had a maximum sampling interval of 500 milliseconds and even displayed inconsistent sampling times. On occasion, there were periods of up to one minute with no recorded data. As a result, significant effort was needed to align the data sets, requiring averaging during data processing.
- The mixture temperature was only measured by one system. Since temperature is necessary for calculating water density to convert density into concentration, real-time concentration calculations were not possible. All conversions had to be performed after testing, increasing the workload.
- During testing, minimising the number of steps is essential, as each step introduces the potential for errors or omissions. On several occasions, one of the systems encountered an error or was overlooked, necessitating the repetition of tests.

Improvement to the Vibrating Fork

To improve the sample section of the vibrating fork, a concentric reducer should be used instead of a Y-section.

The issue with the Y-section is that it is questionable whether the pocket in the Y-section represents the flow accurately. With larger grain sizes (primarily coarse sediment), sediment build-up was observed on the bottom pipe wall. This sediment was not subjected to vibration by the fork and thus went unmeasured.

In tests with clay (fine sediment and deep-sea sediment), it was observed that the pocket could not be properly circulated. Due to the cohesive properties of clay, the mixture in the pocket became fixed and was not effectively exchanged with the main flow. This issue arose only at the highest target concentrations of 160 g/L, making it doubtful whether the measured mixture was representative of the overall flow.

These issues could be mitigated by using a concentric reducer, placing the sensor in the middle of the flow. The pipe diameter expansion via the concentric reducer would reduce the velocity to below 1 m/s. This setup could introduce a minor error due to slight changes in concentration from flow direction differences, as illustrated in Figure 3.8a. However, this error is negligible compared to the current issues.

Additionally, upgrading to a higher-quality sensor would significantly improve performance. The current sensor was highly prone to errors. When initiated in clean water, the sensor often displayed inconsistent density values for water within a range of ± 10 kg/m³. Every time the sensor was restarted, it required

recalibration. Furthermore, after increasing and subsequently reducing the flow velocity to zero, the sensor often read a different density value, even though the mixture remained unchanged.

Improvement to the U-loop

The original U-loop measurement pipes were constructed from PMMA with a diameter of 40 mm, whereas the newly introduced pipes in the setup had a diameter of 45 mm. This significant diameter change influenced both flow and pressure. Additionally, bends in the pipes affected the flow and pressure. These factors must be minimised near the measurement points to avoid impacting the pressure sensors.

To improve the U-loop, it is recommended to extend the U-loop to increase the distance between the measurement points and the bends. Furthermore, replacing the pipes with ones that match the original U-loop diameter would help eliminate discrepancies. This could reduce or even eliminate the need for velocity compensation, as described in Subsection 5.2.6.

Improving pump seal

During testing different causes for leakage could be identified of which the pump was the biggest leak. This leakage was minimized by using a lot of shaft grease. This grease partially enters in to the system which could potentially create errors for the different sensors. Grease could stick to vibrating parts and mislead the sensor, or it could block the connection tubes of the pressure sensors. Another problem is that a lot of mixture is leaked from the system through the pump seal. This leaked mixture is collected and put back into the system but this process is not perfect and errors are created.

Re-do the first test to check for drift

The first test should be repeated to assess potential drift in sensor performance over the test period. Drift can occur due to prolonged operation, wear, or environmental factors such as temperature fluctuations. Repeating the test under controlled conditions and comparing the results with the original data will help evaluate the stability and reliability of the sensors over time.

6.2. Future Research

The findings of this study highlight several areas for further investigation to enhance sediment concentration measurement in deep-sea mining operations:

Improved Research into Non-Density Sensors

While density-based sensors like the Coriolis sensor performed well, there is potential to explore non-density sensors such as optical, acoustic, or conductivity sensors. Besides their lower expectations, these sensors were partially excluded due to the limited resources of this thesis. These technologies could offer advantages in detecting low concentrations or addressing other limitations of current methods.

Distinguishing Between Sediment and Nodule Fines

The ability to differentiate sediment concentrations from nodule fines would provide more granular insights into return flow compositions. This could involve investigating sensors capable of detecting particle properties, such as size, shape, or mineral composition.

Larger-Scale Testing

Future studies should replicate these tests on a larger scale to better simulate industrial conditions. Larger pipelines, higher flow rates, and more complex systems could reveal challenges like sediment accumulation, sensor placement issues which are not visible in smaller setups. This research can also focus on representative sampling for a bypass flow, which will probably be used in full-scale mining.

Pressure Testing

Concentration measurements during deep-sea mining operations must also be conducted at high pressures, particularly in the diffuser at the back of the collector at the sea floor. For these applications, these sensors could potentially be utilised with modifications. The necessary modifications need to be identified, and measurement tests under high-pressure conditions should be conducted to verify sensor performance.

Long-Term Reliability Testing
Extended testing over longer durations is essential to evaluate sensor wear, performance drift, and reliability in real-world conditions. This would provide insights into the operational lifespan of the sensors and inform maintenance and calibration schedules for industrial use.

Testing in Saltwater Conditions
The tests conducted in this study used freshwater, whereas deep-sea mining operations occur in saline environments. Future research should examine how saltwater affects sensor performance, including potential influences on sediment behaviour, corrosion, and measurement accuracy.

Enhanced Sensor Technology
Investigating advanced sensor technologies or hybrid systems that combine different methodologies could improve measurement accuracy and robustness under challenging conditions. For example, integrating density-based measurements with optical or acoustic methods could increase performance for lower sediment concentration.

References

[1] International Seabed Authority (ISA). *Polymetallic nodules*. Tech. rep. 2021. URL: https://www.isa.org.jm/wp-content/uploads/2022/06/eng7.pdf.

[2] Sedlecký kaolin a.s. *TECHNICAL DATA SHEET, KAOLIN ZETTLITZ ia*. Tech. rep. Jan. 2021. URL: www.sedlecky-kaolin.cz.

[3] American Society for Testing and Materials. *D3977-97(2013)e1, Standard Test Methods for Determining Sediment Concentration in Water Samples*. West Conshohocken, PA: ASTM International, 2013.

[4] ATO. *Digital Tuning Fork density Meter for liquids*. URL: https://www.ato.com/density-meter-for-liquids.

[5] Endress+Hauser B.V. *Proline Promag 55S electromagnetic flowmeter*. URL: https://www.nl.endress.com/en/field-instruments-overview/flow-measurement-product-overview/electromagnetic-flowmeter-promag-55s?t.tabId=product-downloads.

[6] Raouf Baddour. "Thermohaline equation of state for pure water, seawater and brine". In: 61 (Apr. 2023), pp. 211–219. DOI: 10.1080/00221686.2023.2180444.

[7] U. Bergsten et al. "Batch measurements of wood density on intact or prepared drill cores using x-ray microdensitometry". en. In: *Wood Science and Technology* 35.5 (Oct. 2001), pp. 435–452. ISSN: 0043-7719, 1432-5225. DOI: 10.1007/s002260100106. URL: http://link.springer.com/10.1007/s002260100106 (visited on 02/28/2024).

[8] An-Bin Huang, Chih-Ping Lin, and Chih-Chung Chung. "TDR/DMT Characterization of a Reservoir Sediment under Water". en. In: *Journal of GeoEngineering* 3.2 (Jan. 2008). DOI: 10.6310/jog.2008.3(2).3.

[9] Jan J. Bosman, Elsbeth T. J. M. van der Velden, and Cornelis H. Hulsbergen. "Sediment concentration measurement by transverse suction". In: *Coastal Engineering* 11.4 (1987), pp. 353–370. ISSN: 0378-3839. DOI: https://doi.org/10.1016/0378-3839(87)90033-0. URL: https://www.sciencedirect.com/science/article/pii/0378383987900330.

[10] Jamie A.C. Bunt, Piers Larcombe, and Colin F. Jago. "Quantifying the response of optical backscatter devices and transmissometers to variations in suspended particulate matter". In: *Continental Shelf Research* 19.9 (July 1999), pp. 1199–1220. ISSN: 02784343. DOI: 10.1016/S0278-4343(99)00018-7. URL: https://linkinghub.elsevier.com/retrieve/pii/S0278434399000187 (visited on 02/22/2024).

[11] Campbell. *OBS-5+ - Monitoring System with Pressure Sensor for High Suspended-Sediment Concentrations*. URL: https://www.campbellsci.com/obs-5.

[12] Furio Cascetta. "Effect of fluid pressure on Coriolis mass flowmeter's performance". In: *ISA Transactions* 35.4 (Jan. 1996), pp. 365–370. DOI: 10.1016/s0019-0578(96)00048-1. URL: https://www.sciencedirect.com/science/article/pii/S0019057896000481.

[13] Oliver Chmiel, Ivo Baselt, and Andreas Malcherek. "Applicability of Acoustic Concentration Measurements in Suspensions of Artificial and Natural Sediments Using an Acoustic Doppler Velocimeter". en. In: *Acoustics* 1.1 (Dec. 2018), pp. 59–77. ISSN: 2624-599X. DOI: 10.3390/acoustics1010006. URL: https://www.mdpi.com/2624-599X/1/1/6 (visited on 02/22/2024).

[14] Chih-Chung Chung and Chih-Ping Lin. "High concentration suspended sediment measurements using time domain reflectometry". en. In: *Journal of Hydrology* 401.1-2 (Apr. 2011), pp. 134–144. ISSN: 00221694. DOI: 10.1016/j.jhydrol.2011.02.016. URL: https://linkinghub.elsevier.com/retrieve/pii/S0022169411001235 (visited on 03/08/2024).

[15] Roland Clift and Diana H. Manning Clift. "Continuous measurement of the density of flowing slurries". en. In: *International Journal of Multiphase Flow* 7.5 (Oct. 1981), pp. 555–561. ISSN: 03019322. DOI: 10.1016/0301-9322(81)90058-6. URL: https://linkinghub.elsevier.com/retrieve/pii/0301932281900586 (visited on 03/13/2024).

[16] Emerson Electric Co. *Installation Manual Micro Motion ELITE*. Tech. rep. Jan. 2024. URL: https://www.emerson.com/documents/automation/installation-manual-micro-motion-elite-coriolis-flow-density-sensors-en-64354.pdf.

[17] Charles R. Coble, Elaine G. Murray, and Dale R. Rice. *Prentice-Hall Earth Science*. Prentice-Hall, Inc., Jan. 1987. ISBN: 978-0136992400.

[18] C. F. Colebrook and C. M. White. "Experiments with fluid friction in roughened pipes". In: *Proceedings of the Royal Society of London A Mathematical and Physical Sciences* 161.906 (Aug. 1937), pp. 367–381. DOI: 10.1098/rspa.1937.0150. URL: https://doi.org/10.1098/rspa.1937.0150.

[19] *Coriolis Flow Meter: L-CoR | Anton Paar*. URL: https://www.anton-paar.com/nl-en/products/details/l-cor-8x00/.

[20] N A Crossouard, J A Taylor, and M W Lee. "POTENTIAL SOURCES AND MAGNITUDE OF ERRORS ASSOCIATED WITH THE MEASUREMENT OF SUSPENDED SEDIMENT CONCENTRATION". In: ().

[21] Yu Dai, Yanyang Zhang, and Xuyang Li. "Numerical and experimental investigations on pipeline internal solid-liquid mixed fluid for deep ocean mining". en. In: *Ocean Engineering* 220 (Jan. 2021), p. 108411. ISSN: 00298018. DOI: 10.1016/j.oceaneng.2020.108411. URL: https://linkinghub.elsevier.com/retrieve/pii/S0029801820313184 (visited on 03/22/2024).

[22] John Downing. "Twenty-five years with OBS sensors: The good, the bad, and the ugly". In: *Continental Shelf Research* 26.17 (Nov. 2006), pp. 2299–2318. ISSN: 02784343. DOI: 10.1016/j.csr.2006.07.018. URL: https://linkinghub.elsevier.com/retrieve/pii/S0278434306002469 (visited on 02/22/2024).

[23] Jeffrey C. Drazen et al. "Midwater ecosystems must be considered when evaluating environmental risks of deep-sea mining". en. In: *Proceedings of the National Academy of Sciences* 117.30 (July 2020), pp. 17455–17460. ISSN: 0027-8424, 1091-6490. DOI: 10.1073/pnas.2011914117. URL: https://pnas.org/doi/full/10.1073/pnas.2011914117 (visited on 02/23/2024).

[24] Ivo Dreiseitl. "ABOUT GEOTECHNICAL PROPERTIES OF THE DEEP SEABED POLYMETALLIC NODULES". In: Sept. 2017.

[25] easac. "Deep Sea Mining assessing evidence on future needs and environmental impacts". In: *d* d (2023), p. d.

[26] Emily Eidam et al. "OpenOBS: Open□source, low□cost optical backscatter sensors for water quality and sediment□transport research". In: *Limnology and Oceanography: Methods* 20.1 (Dec. 2021), pp. 46–59. DOI: 10.1002/lom3.10469. URL: https://doi.org/10.1002/lom3.10469.

[27] Emerson. *Installation Manual Micro Motion Fork Density meters*. Tech. rep. Apr. 2019. URL: https://www.emerson.com/documents/automation/installation-manual-fork-density-meter-micro-motion-en-64564.pdf.

[28] *Fluvial sediment transport: analytical techniques for measuring sediment load*. OCLC: 61732553. Vienna: International Atomic Energy Agency, 2005. ISBN: 978-92-0-107605-2.

[29] Ian Foster, Rob Millington, and R. GREW. "The impact of particle size controls on stream turbidity measurement; some implications for suspended sediment yield estimation". In: *Erosion and sediment monitoring programmes in river basins. Proc. international symposium, Oslo, 1992* 210 (Jan. 1992).

[30] Souza Dias Francisco. *Turbidity sensors - Coastal Wiki*. 2020. URL: https://www.coastalwiki.org/wiki/Turbidity_sensors.

[31] Benjamin Gillard et al. "Physical and hydrodynamic properties of deep sea mining-generated, abyssal sediment plumes in the Clarion Clipperton Fracture Zone (eastern-central Pacific)". In: *Elementa* 7 (Jan. 2019). DOI: 10.1525/elementa.343. URL: https://doi.org/10.1525/elementa.343.

[32] Walter H. Graf et al. *Critical velocity for solid-liquid mixtures*. Tech. rep. 1970. URL: https://core.ac.uk/download/pdf/228623912.pdf.

[33] Brian Greenwood et al. “NEARSHORE SEDIMENT FLUX AND BOTTOM BOUNDARY DYNAMICS THE CANADIAN COASTAL SEDIMENT TRANSPORT PROGRAMME (C-COAST)”. en. In: *Coastal Engineering Proceedings* 22 (Jan. 1990). Number: 22. ISSN: 2156-1028. DOI: 10.9753/icce.v22.%p. URL: https://icce-ojs-tamu.tdl.org/icce/article/view/4597 (visited on 02/27/2024).

[34] F van Grunsven and Allseas. *Interview*. 2024.

[35] F van Grunsven and A M Talmon. “LOCAL ANOMALIES IN SLIP FOR SLURRY FLOW WITHIN PIPES NEAR THE DEPOSIT LIMIT VELOCITY”. en. In: (Dec. 2012).

[36] Maciej Filip Gruszczyński et al. “A Simple and Effective Method for Measuring the Density of Non-Newtonian Thickened Tailings Slurry during Hydraulic Transport”. In: *Sensors* 22.20 (Oct. 16, 2022), p. 7857. ISSN: 1424-8220. DOI: 10.3390/s22207857. URL: https://www.mdpi.com/1424-8220/22/20/7857 (visited on 02/22/2024).

[37] Boyun Guo and Ali Ghalambor. “Chapter 11 - Transportation”. In: *Natural Gas Engineering Handbook (Second Edition)*. Ed. by Boyun Guo and Ali Ghalambor. Second Edition. Gulf Publishing Company, 2005, pp. 219–262. ISBN: 978-1-933762-41-8. DOI: https://doi.org/10.1016/B978-1-933762-41-8.50018-6. URL: https://www.sciencedirect.com/science/article/pii/B9781933762418500186.

[38] Xingsen Guo et al. “Deep seabed mining: Frontiers in engineering geology and environment”. In: *International Journal of Coal Science & Technology* 10.1 (Apr. 2023). DOI: 10.1007/s40789-023-00580-x. URL: https://doi.org/10.1007/s40789-023-00580-x.

[39] Sabine Haalboom et al. “Monitoring of Anthropogenic Sediment Plumes in the Clarion-Clipperton Zone, NE Equatorial Pacific Ocean”. en. In: *Frontiers in Marine Science* 9 (June 2022), p. 882155. ISSN: 2296-7745. DOI: 10.3389/fmars.2022.882155. URL: https://www.frontiersin.org/articles/10.3389/fmars.2022.882155/full (visited on 02/22/2024).

[40] PE Halbach and A Abram. *Study report about the surface sediments in the NE Pacific Clarion-Clipperton Zone (CCZ): type of sediments, mineral and chemical composition and soil mechanical results of the surface layers*. Tech. rep. 2013.

[41] Manus Henry et al. “Two-phase flow metering of heavy oil using a Coriolis mass flow meter: A case study”. In: *Flow Measurement and Instrumentation* 17.6 (Dec. 2006), pp. 399–413. ISSN: 09555986. DOI: 10.1016/j.flowmeasinst.2006.07.008. URL: https://linkinghub.elsevier.com/retrieve/pii/S0955598606000446 (visited on 02/22/2024).

[42] Imbros. *LISST-ABS Acoustic Backscatter Sensor for sale - Imbros*. Nov. 2019. URL: https://imbros.com.au/product/lisst-abs-acoustic-backscatter-sensor/.

[43] Nauru Ocean Resources Inc. *CARMU Investigation Report 01/2023*. Tech. rep. Apr. 2023. URL: https://www.isa.org.jm/wp-content/uploads/2023/05/NORI-Investigation-report-27.04.23.pdf.

[44] Instrumart. *Micro Motion FDM Fork Density Meter | Density Meters |*. URL: https://www.instrumart.com/products/46974/micro-motion-fdm-fork-density-meter.

[45] Instrumart. *Rosemount Pressure Transmitters*. URL: https://www.instrumart.com/brand-category/1207/6219/rosemount-pressure-transmitters.

[46] Daniel O.B. Jones et al. “Environment, ecology, and potential effectiveness of an area protected from deep-sea mining (Clarion Clipperton Zone, abyssal Pacific)”. en. In: *Progress in Oceanography* 197 (Sept. 2021), p. 102653. ISSN: 00796611. DOI: 10.1016/j.pocean.2021.102653. URL: https://linkinghub.elsevier.com/retrieve/pii/S0079661121001385 (visited on 03/21/2024).

[47] S.B. Jones, Jon M. Wraith, and Dani Or. “Time domain reflectometry measurement principles and applications”. In: *Hydrological Processes* 16 (2002). URL: https://api.semanticscholar.org/CorpusID:14751763.

[48] R. P. King. “4 - Transportation of slurries”. In: *Introduction to Practical Fluid Flow*. Ed. by R. P. King. Oxford: Butterworth-Heinemann, Jan. 2002, pp. 81–116. ISBN: 978-0-7506-4885-1. DOI: 10.1016/B978-075064885-1/50004-1. URL: https://www.sciencedirect.com/science/article/pii/B9780750648851500041 (visited on 03/22/2024).

[49] Jan Krupička and Václav Matoušek. *Mathematical and physical modelling of pipe flow of settling slurries*. July 2014. URL: https://dspace.cvut.cz/handle/10467/30667.

[50] Thomas Kuhn et al. “Composition, Formation, and Occurrence of Polymetallic Nodules”. In: Mar. 2017, pp. 23–63. ISBN: 978-3-319-52556-3. DOI: 10.1007/978-3-319-52557-0_2.

[51] Laboratorium.shop. *Filterpapier MN-616 md middel-snel filtrerend, 55 sec. kwalitatief, rond*. Oct. 2024. URL: https://www.laboratorium.shop/product/filterpapier-mn-616-md-middel-snel-filtrerend-55-sec-kwalitatief-100-stuks/.

[52] Laboratorium.shop. *Filterpapier MN-617 zeer snel filtrerend, 9 sec., kwalitatief, rond*. Sept. 2024. URL: https://www.laboratorium.shop/product/filterpapier-mn-617-zeer-snel-filtrerend-9-sec-kwalitatief-rond/.

[53] Laboratorium.shop. *Filterpapier MN-619 de zeer langzaam filtrerend, 195 sec. kwalitatief, rond*. Oct. 2024. URL: https://www.laboratorium.shop/product/filterpapier-mn-619-de-zeer-langzaam-filtrerend-195-sec-kwalitatief-rond/.

[54] T. Lanckriet, J. A. Puleo, and N. Waite. “A Conductivity Concentration Profiler for Sheet Flow Sediment Transport”. en. In: *IEEE Journal of Oceanic Engineering* 38.1 (Jan. 2013), pp. 55–70. ISSN: 0364-9059, 1558-1691. DOI: 10.1109/JOE.2012.2222791. URL: http://ieeexplore.ieee.org/document/6363485/ (visited on 03/05/2024).

[55] B.G. Lipták. *Instrument engineers’ handbook: Process measurement and analysis, fourth edition*. Jan. 2003, pp. 1–1861.

[56] emerson process management. *High Capacity Coriolis*. 2013. URL: https://www.emerson.com/documents/automation/brochure-high-capacity-coriolis-micro-motion-en-64962.pdf.

[57] Monte Marshall and U.S. Geological Survey. *SUMMARY OF PHYSICAL PROPERTIES—LEG 32*. Tech. rep. URL: http://deepseadrilling.org/32/volume/dsdp32_appendixI.pdf.

[58] Gustavo Henrique Merten, Paul D. Capel, and Jean P. G. Minella. “Effects of suspended sediment concentration and grain size on three optical turbidity sensors”. In: *Journal of Soils and Sediments* 14.7 (July 2014), pp. 1235–1241. ISSN: 1439-0108, 1614-7480. DOI: 10.1007/s11368-013-0813-0. URL: http://link.springer.com/10.1007/s11368-013-0813-0 (visited on 02/23/2024).

[59] Sape A. Miedema. *Slurry Transport Fundamentals, A Historical Overview ; The Delft Head Loss ; Limit Deposit Velocity Framework 2nd Edition*. Jan. 2019. DOI: 10.5074/t.2019.002. URL: https://textbooks.open.tudelft.nl/textbooks/catalog/book/17.

[60] Micro Motion. *Product Data sheet*. Tech. rep. June 2014. URL: https://www.bkwinstruments.co.uk/wp-content/uploads/2015/06/Fork-Density-Meter.pdf.

[61] Micro Motion. *Product Data sheet*. Tech. rep. Nov. 2024. URL: https://www.emerson.com/documents/automation/product-data-sheet-micro-motion-elite-coriolis-flow-density-meters-en-66748.pdf.

[62] Multiquartz and Hans van der Velde. *Multiquartz HN 0.1 mm - 0.3 mm Analyse*. Tech. rep. Jan. 2021.

[63] Nori. “Collector Test study Environmental Impact statement”. In: (July 2021). URL: https://static1.squarespace.com/static/611bf5e1fae42046801656c0/t/6152820c295c1543ff79796c/1632797221691/NORI-D+COLLECTOR+TEST+EIS_FINAL_ABBREVIATED_RE.pdf.

[64] Tom O’Banion. “Coriolis: The Direct Approach to Mass Flow Measurement”. In: *Back to Basics* ().

[65] John Parianos, Anthony O’Sullivan, and Pedro Madureira. “Geology of parts of the central and eastern Clarion Clipperton Zone”. en. In: *Journal of Maps* 18.2 (Dec. 2022), pp. 232–245. ISSN: 1744-5647. DOI: 10.1080/17445647.2022.2035267. URL: https://www.tandfonline.com/doi/full/10.1080/17445647.2022.2035267 (visited on 03/19/2024).

[66] R Paton. “Calibration techniques for coriolis mass flowmeters”. In: *FLOMEKO ’98* (1998).

[67] PipeFlow.com. *Pipe roughness*. Dec. 2024. URL: https://www.pipeflow.com/pipe-pressure-drop-calculations/pipe-roughness.

[68] Pomelo. *What is a turbidity sensor? | Atlas Scientific*. Aug. 2023. URL: https://atlas-scientific.com/blog/what-is-a-turbidity-sensor/.

[69] *Product Data sheet, Rosemount 1151 Pressure Transmitter*. Tech. rep. Feb. 2010. URL: https://www.emerson.com/documents/automation/product-data-sheet-rosemount-1151-pressure-transmitter-en-73232.pdf.

[70] Jack Puleo et al. "A Conductivity Sensor for Nearbed Sediment Concentration Profiling". In: *Journal of Atmospheric and Oceanic Technology - J ATMOS OCEAN TECHNOL* 27 (Feb. 2010). DOI: 10.1175/2009JTECHO718.1.

[71] Markus Raffel et al. *Particle Image Velocimetry*. Jan. 2018. DOI: 10.1007/978-3-319-68852-7. URL: https://doi.org/10.1007/978-3-319-68852-7.

[72] RS. *Kern EMS 12K0.1 Precision Balance Weighing Scale, 12kg Weight Capacity | RS*. URL: https://nl.rs-online.com/web/p/weighing-scales/7898633?srsltid=AfmBOor8D6MAvIKufEwIGC_ouIiRiq24CR0MKn3ER52vV5Rf4MQKfXoZ.

[73] *SEA DATA HRC-660 ACOUSTIC DOPPLER | EBay*. URL: https://www.ebay.ca/itm/362768815275?itmmeta=01HTPRXKHHBGPBWDQEJ68KH88Z&hash=item5476b4d4ab:g:m84AAOSwR0pbfdlG&itmprp=enc%3AAQAJAAAA4ArfHB%2F6K9v1fiUgvRWIyzPgjyZkmff%2BbfNMb6l1Z0VqMCuqVdmMPV4dLjeie%2B9pApU7fNOf9deD%2FFRBbEAEXu6o52Q7bqSen216ELjUfHw5%2FfYghzbkAoL7VfCZER56SJJ4c%2Bo%2FEudE%2FBNv7OQF3Jc9YSCEBzPh3Tvu%2B1tqRFyKHB0phu5FEErub60Ssuk%2FdD1wVQ8r85yKPgvG1qbdDFFErQVa0OADY%2FmiMMrPFRRBZvriIst%2Bugl648OA%2BtKqaq9j4t6y3CtY4wQfYY7Nf12s79N1k8l0V9MqR52XdhMw%7Ctkp%3ABk9SR-i49tjVYw.

[74] Rahul Sharma, ed. *Deep-Sea Mining: Resource Potential, Technical and Environmental Considerations*. en. Cham: Springer International Publishing, 2017. ISBN: 978-3-319-52556-3 978-3-319-52557-0. DOI: 10.1007/978-3-319-52557-0. URL: http://link.springer.com/10.1007/978-3-319-52557-0 (visited on 02/22/2024).

[75] SCR Sibelco. *CRYSTALLINE SILICA FLOUR*. Tech. rep. Oct. 2009. URL: https://coatings.sibelcotools.com/wp-content/uploads/2017/03/TDS_Silverbond_M4-M6-M8-M10_EN.pdf.

[76] Vivek Singhal, Pradeepkumar Ashok, and Eric Van Oort. "X-ray densitometry of drilling fluids at the rig standpipe". en. In: *Journal of Petroleum Science and Engineering* 181 (Oct. 2019), p. 106147. ISSN: 09204105. DOI: 10.1016/j.petrol.2019.06.011. URL: https://linkinghub.elsevier.com/retrieve/pii/S0920410519305595 (visited on 02/28/2024).

[77] Ed Stok. *Handleiding voor het circuit voor hydraulisch transport van korrelvorming materiaal*.

[78] Erik Stokstad. "Prospect of unregulated deep-sea mining looms". In: *Science* 381.6655 (July 2023), pp. 254–255. DOI: 10.1126/science.adj8304. URL: https://doi.org/10.1126/science.adj8304.

[79] Nazilla Tarabi et al. "Developing and evaluation of an electrical impedance tomography system for measuring solid volumetric concentration in dredging scale". en. In: *Flow Measurement and Instrumentation* 80 (Aug. 2021), p. 101986. ISSN: 09555986. DOI: 10.1016/j.flowmeasinst.2021.101986. URL: https://linkinghub.elsevier.com/retrieve/pii/S0955598621000959 (visited on 03/12/2024).

[80] SenTec Technology. *SPX504 Tuning Fork Densitometer Manual*. Tech. rep. URL: https://cdsentec.com/wp-content/uploads/2022/06/SPX504.pdf.

[81] *The control of re-suspension over mega-ripples on the continental shelf*. Coastal Sediments, 1999, pp. 269–280.

[82] P.D Thorne et al. "Measuring suspended sediment concentrations using acoustic backscatter devices". In: *Marine Geology* 98.1 (May 1991), pp. 7–16. ISSN: 00253227. DOI: 10.1016/0025-3227(91)90031-X. URL: https://linkinghub.elsevier.com/retrieve/pii/00253227919003 1X (visited on 02/22/2024).

[83] Stein-Arild Tjungum and Romulus Mihalca. "X-ray based densitometer for multiphase flow measurement". In: 2009. URL: https://api.semanticscholar.org/CorpusID:199522965.

[84] Jarrod Trevathan, Wayne Read, and Abdul Sattar. “Implementation and Calibration of an IoT Light Attenuation Turbidity Sensor”. In: *Internet of Things* 19 (Aug. 2022), p. 100576. ISSN: 25426605. DOI: 10.1016/j.iot.2022.100576. URL: https://linkinghub.elsevier.com/retrieve/pii/S2542660522000671 (visited on 02/23/2024).

[85] Shuuji Urabe and Kiyoaki Koyama. “ROTAMASS 3 Series Coriolis Mass Flow and Density Meter”. en. In: (2010).

[86] D. W. Van der Linde. *Protocol for determination of total suspended matter in oceans and coastal zones*. Technical Note I. Joint Research Centre, 1998, p. 182.

[87] Leo. C. Van Rijn. *Manual sediment transport measurements in rivers, estuaries and coastal seas*. 2nd ed. Rijkswaterstaat, Jan. 2007. URL: https://open.rijkswaterstaat.nl/open-overheid/onderzoeksrapporten/@87696/manual-sediment-transport-measurements/.

[88] Sidney Viana. “Measurement of Overflow Density in Spiral Classifiers Using a Vibrating Fork Densitometer with Accuracy Evaluation”. en. In: *Brazilian Journal of Instrumentation and Control* 3.1 (Sept. 2016), p. 10. ISSN: 2318-4531. DOI: 10.3895/bjic.v3n1.4451. URL: https://periodicos.utfpr.edu.br/bjic/article/view/4451 (visited on 03/14/2024).

[89] *Viscosity of Water – viscosity table and viscosity chart | Anton Paar Wiki*. URL: https://wiki.anton-paar.com/nl-en/water/.

[90] Robert Visintainer et al. *Slurry Transport Using Centrifugal Pumps*. en. Cham: Springer International Publishing, 2023. ISBN: 978-3-031-25439-0. DOI: 10.1007/978-3-031-25440-6. URL: https://link.springer.com/10.1007/978-3-031-25440-6 (visited on 03/13/2024).

[91] VWR. *VWR®, Maatkolven, klasse A, glas, helder, NS-kunststof stop*. 2024. URL: https://nl.vwr.com/store/product/7080205/vwr-maatkolven-klasse-a-glas-helder-ns-kunststof-stop.

[92] Zhenyu Xu et al. “A High-Performance, Reconfigurable, Fully Integrated Time-Domain Reflectometry Architecture Using Digital I/Os”. In: *IEEE Transactions on Instrumentation and Measurement* 70 (2021), pp. 1–9. DOI: 10.1109/TIM.2021.3060586.

[93] Hai Yang et al. “Research on Tuning Fork Dimension Optimization and Density Calculation Model Based on Viscosity Compensation for Tuning Fork Density Sensor”. en. In: *Mathematical Problems in Engineering* 2020 (Oct. 2020). Ed. by Alessandro Lo Schiavo, pp. 1–17. ISSN: 1563-5147, 1024-123X. DOI: 10.1155/2020/7960546. URL: https://www.hindawi.com/journals/mpe/2020/7960546/ (visited on 03/14/2024).

[94] Yokogawa. *ROTAMASS 3 Series Coriolis Mass Flow Meter | Yokogawa Nederland*. URL: https://www.yokogawa.com/nl/solutions/discontinued/rotamass-3/#Details__Benefits.

[95] Lotfi Zeghadnia, Jean Loup Robert, and Bachir Achour. “Explicit solutions for turbulent flow friction factor: A review, assessment and approaches classification”. In: *Ain Shams Engineering Journal* 10.1 (Feb. 2019), pp. 243–252. DOI: 10.1016/j.asej.2018.10.007. URL: https://doi.org/10.1016/j.asej.2018.10.007.

A

Result sheets of the processed data

The data sheets in this appendix show the processed results of the different series test, it shows us both the mean and the standard deviation of each individual test. The following terminology is us: $\rho_w(kg/m)$ is the water density, $c_T(kg/m)$ is the Theoretical concentration, $c_M(kg/m)$ is the manual sampling concentration, c_F is the vibrating fork concentration, $c_C(kg/m)$ is the coriolis concentration, $c_U(kg/m)$ is the U-loop concentration, $T(C)$ is the temperature of the mixture, $v(m/s)$ is the velocity of the mixture through the velocity sensor.

B series

Test	Statistic type	$\rho_w(kg/m)$	$c_T(g/L)$	$c_M(g/L)$	$c_F(g/L)$	$c_C(g/L)$	$c_U(g/L)$	T (°C)	v (m/s)
b1	mean	998.42	0.000	0.000	0.149	0.243	-0.001	18.931	1.988
	std	0.01	0.000	0.000	1.997	0.018	3.843	0.029	0.071
b2	mean	998.28	0.000	0.000	-5.142	0.348	-0.002	19.664	3.000
	std	0.02	0.000	0.000	0.721	0.030	6.148	0.081	0.070
b3	mean	997.91	0.000	0.000	-3.767	0.507	-0.003	21.440	3.987
	std	0.03	0.000	0.000	0.812	0.033	8.190	0.137	0.069
b4	mean	998.06	5.001	5.708	8.053	5.864	nan	22.553	2.017
	std	0.01	0.000	0.814	2.083	0.105	nan	0.074	0.068
b5	mean	997.95	5.001	5.688	0.823	5.485	nan	23.342	3.008
	std	0.04	0.000	0.408	2.223	0.070	nan	0.140	0.064
b6	mean	997.70	5.001	6.244	-6.481	5.407	nan	24.480	4.021
	std	0.06	0.000	1.032	1.044	0.066	nan	0.318	0.064
b7	mean	998.09	9.905	12.796	8.363	11.989	nan	21.216	1.986
	std	0.01	0.000	0.564	0.658	0.134	nan	0.006	0.064
b8	mean	997.96	9.905	12.662	7.046	11.154	nan	21.623	3.009
	std	0.04	0.000	0.221	0.710	0.057	nan	0.018	0.075
b9	mean	997.70	9.905	12.758	1.182	10.621	nan	22.553	3.981
	std	0.08	0.000	0.972	0.646	0.125	nan	0.007	0.065
b10	mean	997.70	19.711	27.858	22.658	25.103	nan	21.200	2.018
	std	0.01	0.000	2.254	1.116	0.261	nan	0.048	0.068
b11	mean	997.58	19.711	26.870	14.756	23.426	nan	21.887	3.009
	std	0.03	0.000	2.905	0.927	0.207	nan	0.135	0.067
b12	mean	997.29	19.711	28.676	13.566	22.368	nan	22.450	3.982
	std	0.08	0.000	3.427	0.611	0.043	nan	0.006	0.060
b13	mean	997.83	39.337	59.276	47.970	53.141	nan	22.299	2.004
	std	0.01	0.000	2.391	1.177	0.514	nan	0.045	0.067
b14	mean	997.70	39.337	54.774	41.743	48.979	nan	22.777	3.022
	std	0.03	0.000	0.878	1.016	0.362	nan	0.152	0.066
b15	mean	997.39	39.337	58.548	37.674	46.374	nan	24.076	4.009
	std	0.09	0.000	6.092	0.961	0.326	nan	0.291	0.064
b16	mean	997.46	78.619	126.208	84.760	112.328	128.104	19.498	1.960
	std	0.01	0.000	5.781	0.922	0.968	4.808	0.051	0.068
b17	mean	997.34	78.619	118.698	103.322	102.124	117.134	20.089	3.000
	std	0.04	0.000	7.352	1.258	0.934	7.693	0.174	0.067
b18	mean	997.02	78.619	116.854	91.052	95.798	112.841	21.263	3.977
	std	0.07	0.000	12.498	0.912	0.933	9.969	0.364	0.066
b19	mean	997.71	157.305	271.502	165.135	243.737	274.387	21.167	1.992
	std	0.01	0.000	13.236	2.039	2.228	6.110	0.050	0.067
b20	mean	997.04	157.305	253.280	188.898	211.725	240.614	21.869	3.018
	std	0.04	0.000	25.490	1.512	1.748	8.706	0.168	0.067
b21	mean	997.20	157.305	259.430	170.805	199.354	230.579	23.147	3.888
	std	0.08	0.000	15.751	1.106	1.508	9.859	0.400	0.068

Table A.1: B-series processed data

C series

Test	Statistic type	$\rho_w(kg/m)$	$c_T(g/L)$	$c_M(g/L)$	$c_F(g/L)$	$c_C(g/L)$	$c_U(g/L)$	T (°C)	v (m/s)
c1	mean	998.42	0.000	0.000	0.149	0.243	-0.001	18.931	1.988
	std	0.01	0.000	0.000	1.997	0.018	3.843	0.029	0.071
c2	mean	998.28	0.000	0.000	-5.142	0.348	-0.002	19.664	3.000
	std	0.02	0.000	0.000	0.721	0.030	6.148	0.081	0.070
c3	mean	997.91	0.000	0.000	-3.767	0.507	-0.003	21.440	3.987
	std	0.03	0.000	0.000	0.812	0.033	8.190	0.137	0.069
c4	mean	998.06	5.001	4.650	11.089	5.419	3.079	20.715	1.978
	std	0.01	0.000	0.113	6.150	0.046	3.952	0.044	0.070
c5	mean	997.95	5.001	4.790	4.593	5.520	2.493	21.249	2.989
	std	0.04	0.000	0.098	1.782	0.034	6.724	0.169	0.069
c6	mean	997.70	5.001	5.212	0.888	5.668	6.378	22.359	4.006
	std	0.06	0.000	0.029	0.914	0.037	8.911	0.278	0.068
c7	mean	998.09	9.903	9.486	12.295	10.089	13.677	20.595	1.977
	std	0.01	0.000	0.127	0.756	0.070	3.975	0.064	0.070
c8	mean	997.96	9.903	9.776	3.709	10.314	12.909	21.182	2.982
	std	0.04	0.000	0.169	2.012	0.054	6.733	0.185	0.069
c9	mean	997.70	9.903	9.980	-2.203	10.598	15.800	22.359	3.999
	std	0.08	0.000	0.171	0.741	0.052	9.235	0.327	0.069
c10	mean	997.70	19.704	18.860	10.937	19.941	18.597	22.365	2.018
	std	0.01	0.000	0.326	1.917	0.082	4.391	0.044	0.067
c11	mean	997.58	19.704	18.940	11.714	20.220	18.666	22.856	2.985
	std	0.03	0.000	0.209	4.139	0.105	6.778	0.129	0.066
c12	mean	997.29	19.704	19.474	10.978	20.414	21.348	24.062	3.994
	std	0.08	0.000	0.350	0.859	0.042	9.304	0.309	0.065
c13	mean	997.83	39.331	38.322	19.476	40.084	37.555	21.783	2.052
	std	0.01	0.000	0.541	2.379	0.091	4.565	0.066	0.069
c14	mean	997.70	39.331	39.046	25.015	40.114	37.881	22.346	3.012
	std	0.03	0.000	0.564	2.421	0.113	7.844	0.142	0.068
c15	mean	997.39	39.331	39.900	19.413	40.268	40.965	23.643	4.015
	std	0.09	0.000	0.354	0.693	0.043	9.139	0.384	0.068
c16	mean	997.46	78.604	78.486	57.534	81.129	78.821	23.383	2.021
	std	0.01	0.000	0.641	1.036	0.087	4.199	0.047	0.069
c17	mean	997.34	78.604	78.474	59.947	80.443	78.948	23.884	2.983
	std	0.04	0.000	0.301	1.773	0.107	6.982	0.151	0.068
c18	mean	997.02	78.604	78.376	59.344	80.349	80.775	25.142	3.990
	std	0.07	0.000	0.534	0.643	0.062	8.953	0.260	0.067
c19	mean	997.71	157.276	159.268	150.478	163.873	161.596	22.308	2.007
	std	0.01	0.000	2.550	0.970	0.115	4.671	0.049	0.070
c20	mean	997.04	157.276	157.018	152.728	159.875	157.176	25.081	3.008
	std	0.04	0.000	2.785	0.811	0.279	8.056	0.167	0.072
c21	mean	997.20	157.276	157.330	153.437	161.446	161.538	24.440	4.001
	std	0.08	0.000	2.046	0.646	0.113	9.510	0.313	0.071

Table A.2: C-series processed data

D series

Test	Statistic type	$\rho_w(kg/m)$	$c_T(g/L)$	$c_M(g/L)$	$c_F(g/L)$	$c_C(g/L)$	$c_U(g/L)$	T (°C)	v (m/s)
d1	mean	998.42	0.000	0.000	0.149	0.243	-0.001	18.931	1.988
	std	0.01	0.000	0.000	1.997	0.018	3.843	0.029	0.071
d2	mean	998.28	0.000	0.000	-5.142	0.348	-0.002	19.664	3.000
	std	0.02	0.000	0.000	0.721	0.030	6.148	0.081	0.070
d3	mean	997.91	0.000	0.000	-3.767	0.507	-0.003	21.440	3.987
	std	0.03	0.000	0.000	0.812	0.033	8.190	0.137	0.069
d4	mean	997.92	5.001	4.786	2.855	5.397	4.364	21.376	1.990
	std	0.01	0.000	0.048	0.940	0.027	3.959	0.035	0.069
d5	mean	997.82	5.001	4.836	4.866	5.507	5.029	21.814	2.999
	std	0.03	0.000	0.052	1.610	0.030	7.001	0.126	0.067
d6	mean	997.57	5.001	4.796	2.445	5.575	7.498	22.904	4.015
	std	0.07	0.000	0.031	0.726	0.038	8.694	0.307	0.067
d7	mean	998.35	9.905	9.490	-0.125	10.505	9.310	19.290	1.977
	std	0.01	0.000	0.029	0.698	0.077	3.757	0.075	0.071
d8	mean	998.22	9.905	9.526	6.086	10.369	10.202	19.940	3.023
	std	0.03	0.000	0.047	0.970	0.026	7.337	0.154	0.071
d9	mean	997.96	9.905	9.622	4.553	10.409	11.945	21.176	3.995
	std	0.07	0.000	0.050	0.713	0.032	8.529	0.303	0.068
d10	mean	997.86	19.711	19.114	15.808	20.178	18.828	21.641	1.976
	std	0.01	0.000	0.132	0.812	0.025	3.926	0.035	0.070
d11	mean	997.76	19.711	19.112	23.820	20.311	20.002	22.092	2.984
	std	0.03	0.000	0.082	1.231	0.032	7.303	0.154	0.069
d12	mean	997.48	19.711	19.204	22.482	20.363	23.454	23.279	3.397
	std	0.08	0.000	0.062	0.865	0.042	10.442	0.336	1.366
d13	mean	998.12	39.337	38.498	40.166	39.058	37.782	20.420	2.007
	std	0.01	0.000	0.512	0.671	0.029	4.053	0.055	0.071
d14	mean	998.02	39.337	38.892	38.699	39.124	38.927	20.936	3.007
	std	0.03	0.000	0.231	0.698	0.025	7.141	0.157	0.070
d15	mean	997.72	39.337	38.790	39.579	39.207	41.493	22.280	3.644
	std	0.07	0.000	0.201	1.528	0.042	10.851	0.311	1.005
d16	mean	997.66	78.619	77.762	75.795	77.637	75.777	22.510	1.980
	std	0.01	0.000	0.809	0.672	0.027	3.967	0.037	0.070
d17	mean	997.56	78.619	77.604	82.057	77.741	76.756	22.964	2.989
	std	0.03	0.000	1.360	1.153	0.036	7.058	0.147	0.069
d18	mean	997.24	78.619	78.148	82.200	77.818	78.426	24.253	3.996
	std	0.08	0.000	0.247	0.663	0.039	8.837	0.318	0.068
d19	mean	996.62	157.305	155.240	164.986	155.509	152.784	26.647	1.968
	std	0.00	0.000	2.232	0.717	0.026	3.991	0.012	0.070
d20	mean	996.51	157.305	156.234	162.708	155.653	153.162	27.052	3.008
	std	0.04	0.000	0.272	1.016	0.044	6.856	0.151	0.069
d21	mean	996.21	157.305	154.088	168.677	155.722	154.606	28.105	4.001
	std	0.08	0.000	2.292	1.047	0.025	7.916	0.297	0.069

Table A.3: D-series processed data

F series

Test	Statistic type	$\rho_w(kg/m)$	$c_T(g/L)$	$c_M(g/L)$	$c_F(g/L)$	$c_C(g/L)$	$c_U(g/L)$	T (°C)	v (m/s)
f1	mean	998.42	0.000	0.000	-6.475	0.590	-0.001	21.877	2.010
	std	0.01	0.000	0.000	0.815	0.023	3.208	0.046	0.071
f2	mean	998.28	0.000	0.000	-6.801	0.746	-0.003	22.827	3.030
	std	0.02	0.000	0.000	0.671	0.028	6.408	0.125	0.069
f3	mean	997.91	0.000	0.000	-4.616	0.981	-0.004	25.038	4.029
	std	0.03	0.000	0.000	0.823	0.037	7.192	0.292	0.068
f4	mean	998.06	7.233	5.870	0.068	7.364	6.659	23.167	1.995
	std	0.01	0.000	0.056	0.706	0.069	3.384	0.067	0.068
f5	mean	997.95	7.233	5.808	5.139	7.447	6.046	24.286	3.018
	std	0.04	0.000	0.103	0.809	0.042	5.476	0.224	0.067
f6	mean	997.70	7.233	5.762	2.903	7.689	7.080	25.926	4.005
	std	0.06	0.000	0.048	0.767	0.060	7.025	0.418	0.066
f7	mean	998.09	13.248	11.644	16.436	14.041	12.885	22.823	1.989
	std	0.01	0.000	0.073	0.692	0.057	3.322	0.073	0.069
f8	mean	997.96	13.248	11.842	16.418	14.290	12.811	23.668	3.005
	std	0.04	0.000	0.046	0.685	0.033	6.006	0.237	0.069
f9	mean	997.70	13.248	11.648	12.562	14.196	11.144	25.145	3.952
	std	0.08	0.000	0.052	1.186	0.046	7.393	0.466	0.070
f10	mean	997.70	19.258	16.960	22.640	19.302	18.608	21.024	2.000
	std	0.01	0.000	0.072	1.005	0.109	3.260	0.111	0.062
f11	mean	997.58	19.258	16.486	22.819	18.888	17.572	21.916	3.012
	std	0.03	0.000	0.044	0.651	0.026	5.307	0.234	0.065
f12	mean	997.29	19.258	16.522	17.534	19.171	18.239	24.792	4.009
	std	0.08	0.000	0.059	0.980	0.050	7.219	0.450	0.069
f13	mean	997.83	38.651	34.164	43.828	37.726	36.193	23.099	2.011
	std	0.01	0.000	0.070	1.323	0.043	3.321	0.076	0.069
f14	mean	997.70	38.651	33.978	43.662	37.821	36.433	23.755	3.023
	std	0.03	0.000	0.128	0.661	0.026	5.572	0.229	0.067
f15	mean	997.39	38.651	34.066	39.258	38.068	35.611	25.477	4.009
	std	0.09	0.000	0.136	0.768	0.047	7.544	0.469	0.066
f16	mean	997.46	77.698	72.438	85.787	76.381	74.496	22.155	2.009
	std	0.01	0.000	0.480	0.711	0.031	3.393	0.112	0.071
f17	mean	997.34	77.698	72.136	85.122	76.474	74.735	23.101	3.014
	std	0.04	0.000	0.370	0.675	0.029	6.130	0.252	0.069
f18	mean	997.02	77.698	71.970	82.770	76.597	73.738	25.073	3.994
	std	0.07	0.000	0.385	0.745	0.046	7.533	0.539	0.069
f19	mean	997.71	156.876	142.630	159.946	152.283	152.041	25.683	1.939
	std	0.01	0.000	0.682	5.193	1.237	22.489	0.023	0.070
f20	mean	997.04	156.876	141.490	174.560	154.311	151.754	26.425	3.009
	std	0.04	0.000	0.456	1.923	0.168	6.432	0.298	0.067
f21	mean	997.20	156.876	142.212	172.954	154.754	150.219	28.484	3.996
	std	0.08	0.000	0.933	2.537	0.112	7.755	0.460	0.068

Table A.4: F-series processed data

B

Histograms

Note: The range of the concentration axis is not the same for all methodologies. More precise methodologies display smaller ranges.

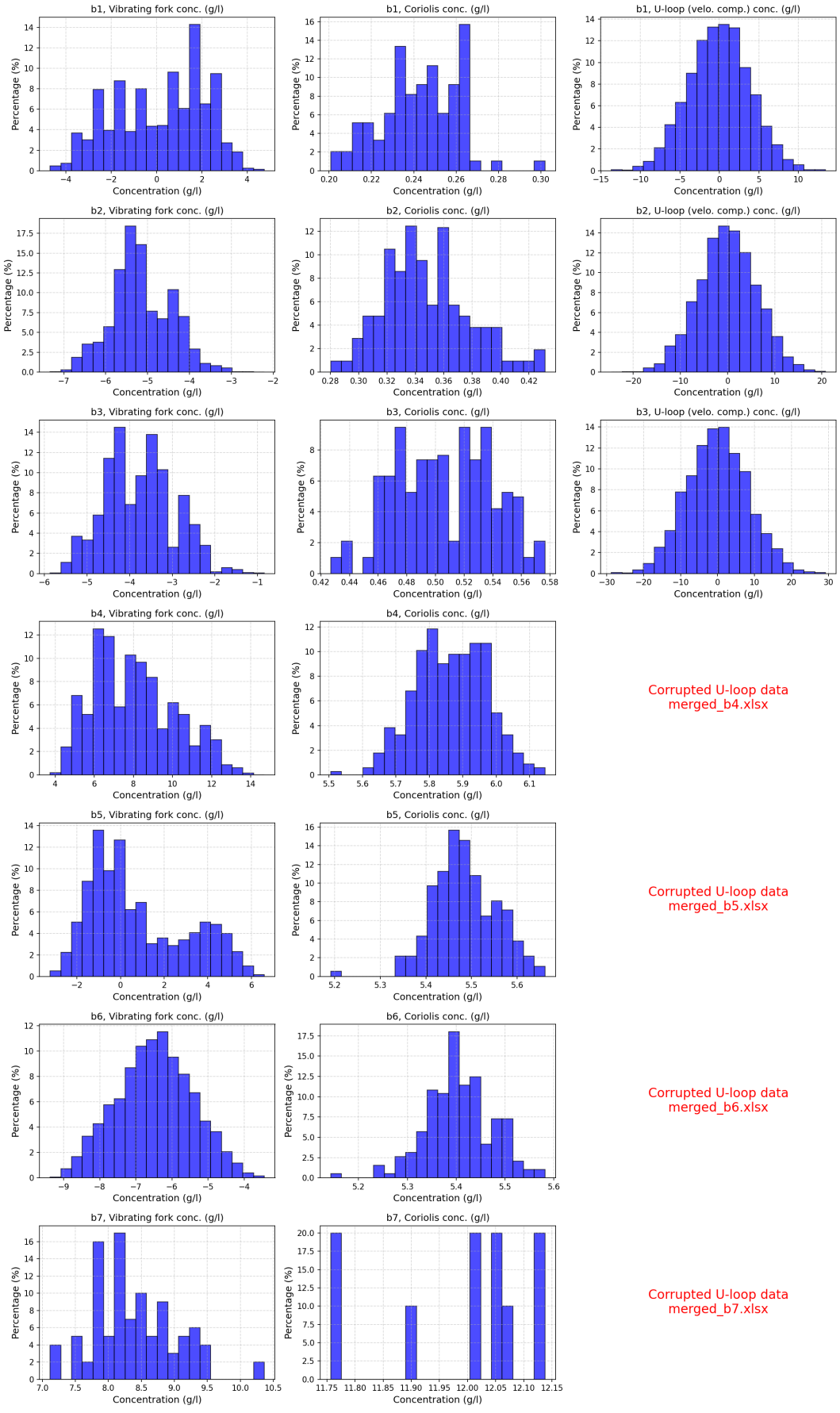

Corrupted U-loop data
merged_b4.xlsx

Corrupted U-loop data
merged_b5.xlsx

Corrupted U-loop data
merged_b6.xlsx

Corrupted U-loop data
merged_b7.xlsx

Figure B.1: B series histograms (test 1-7)

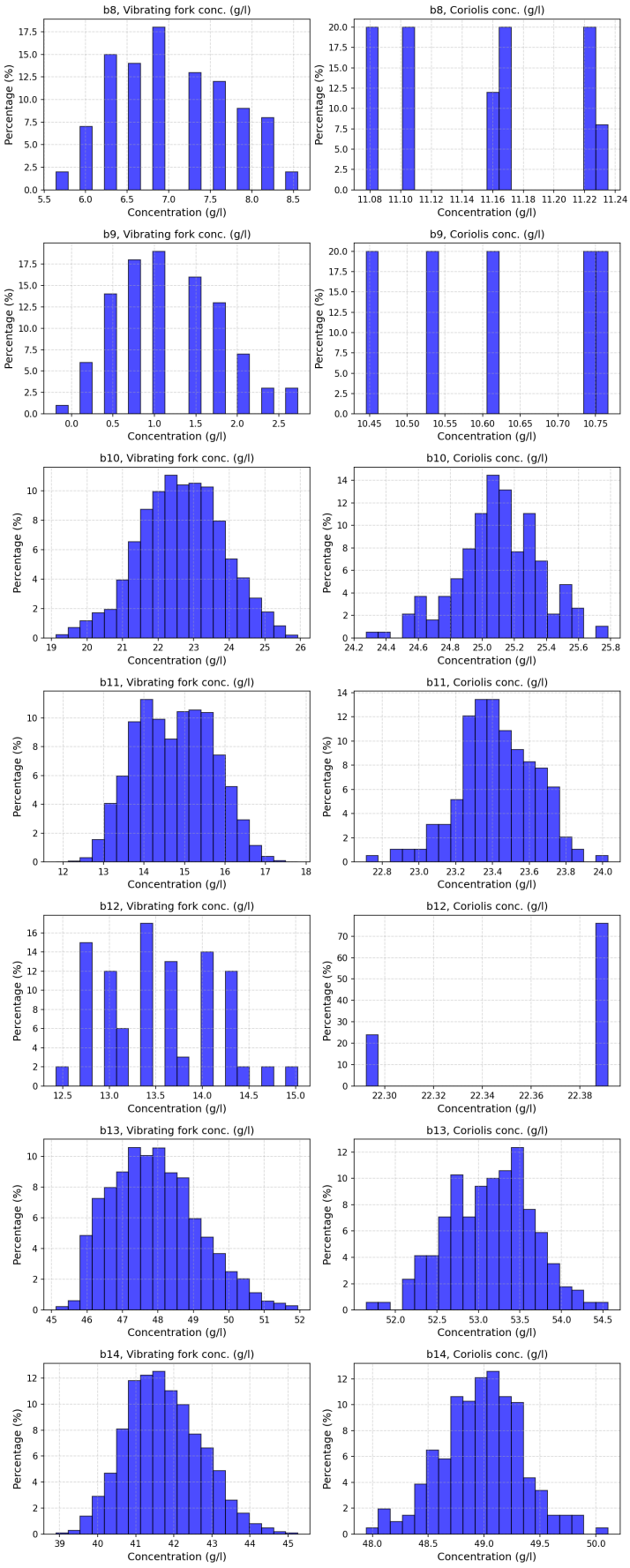

Corrupted U-loop data
merged_b8.xlsx

Corrupted U-loop data
merged_b9.xlsx

Corrupted U-loop data
merged_b10.xlsx

Corrupted U-loop data
merged_b11.xlsx

Corrupted U-loop data
merged_b12.xlsx

Corrupted U-loop data
merged_b13.xlsx

Corrupted U-loop data
merged_b14.xlsx

Figure B.2: B series histograms (test 8-14)

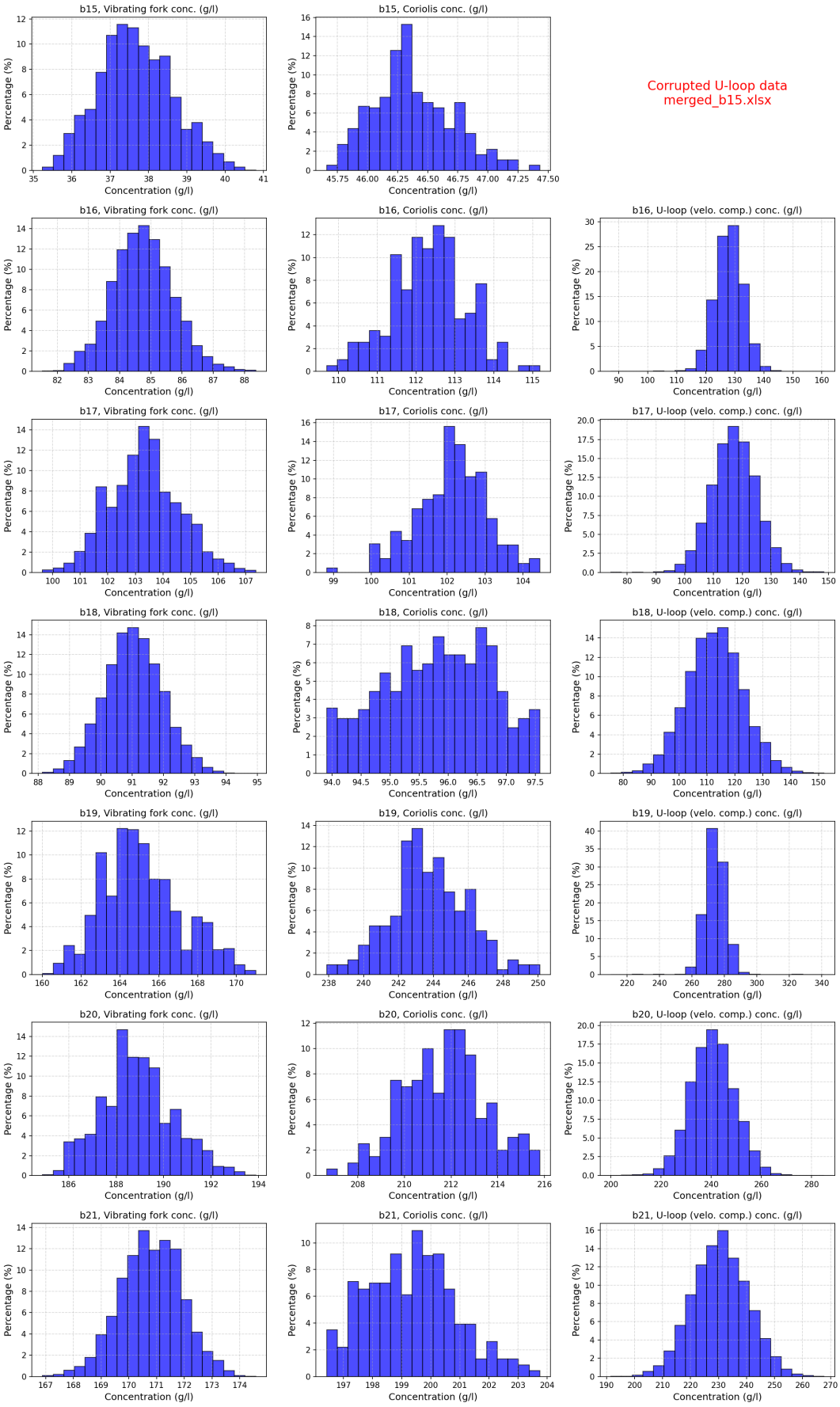

Figure B.3: B series histograms (test 15-21)

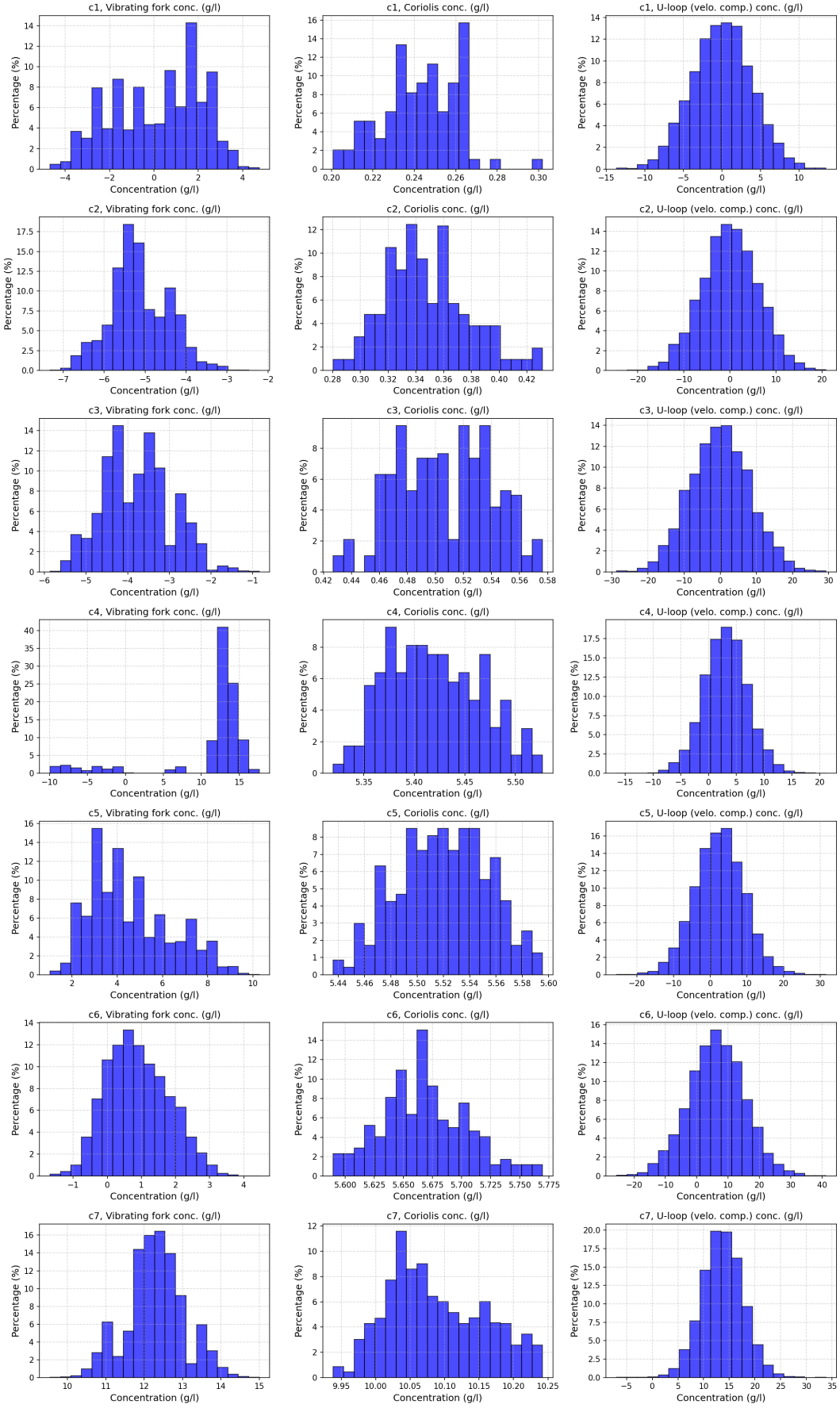

Figure B.4: C series histograms (test 1-7)

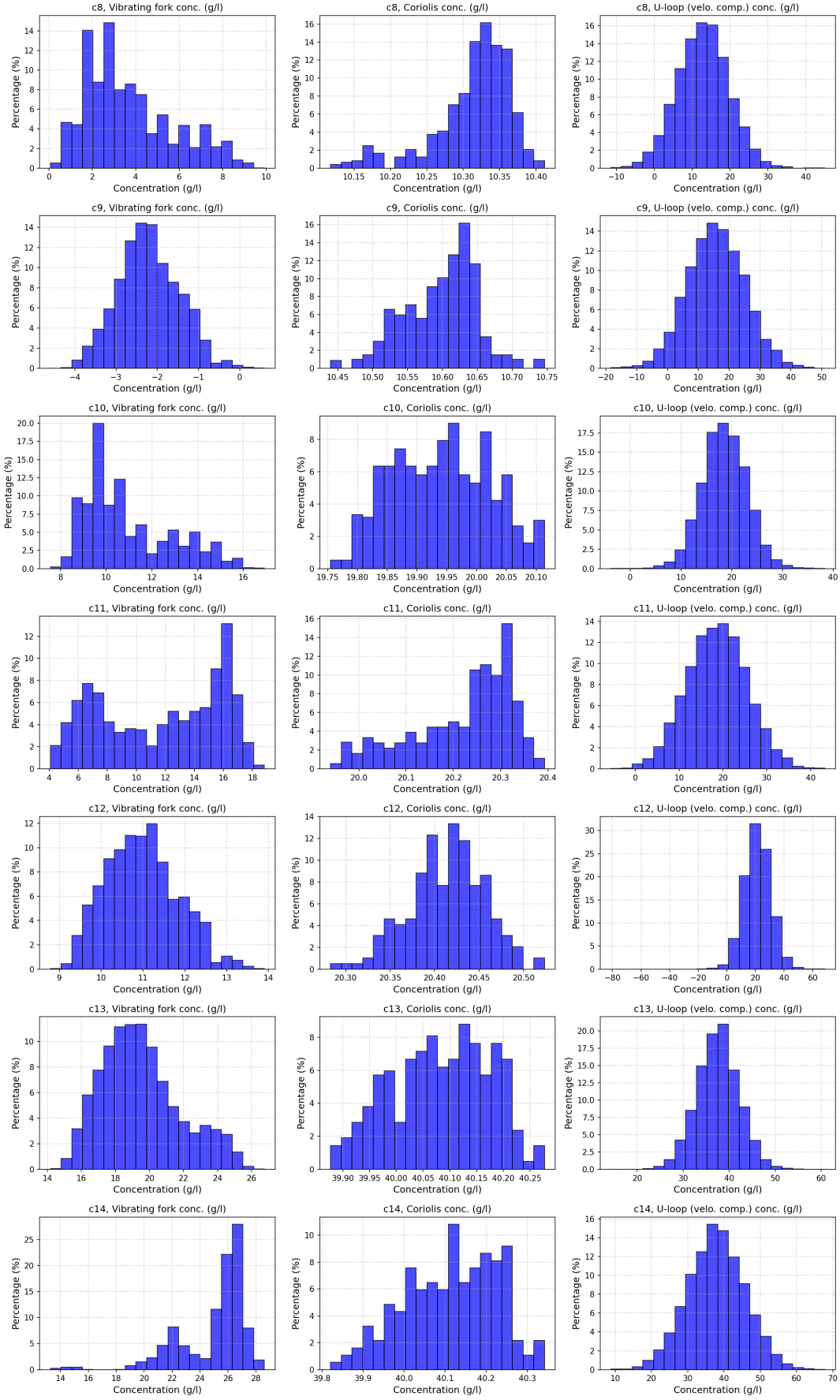

Figure B.5: C series histograms (test 8-14)

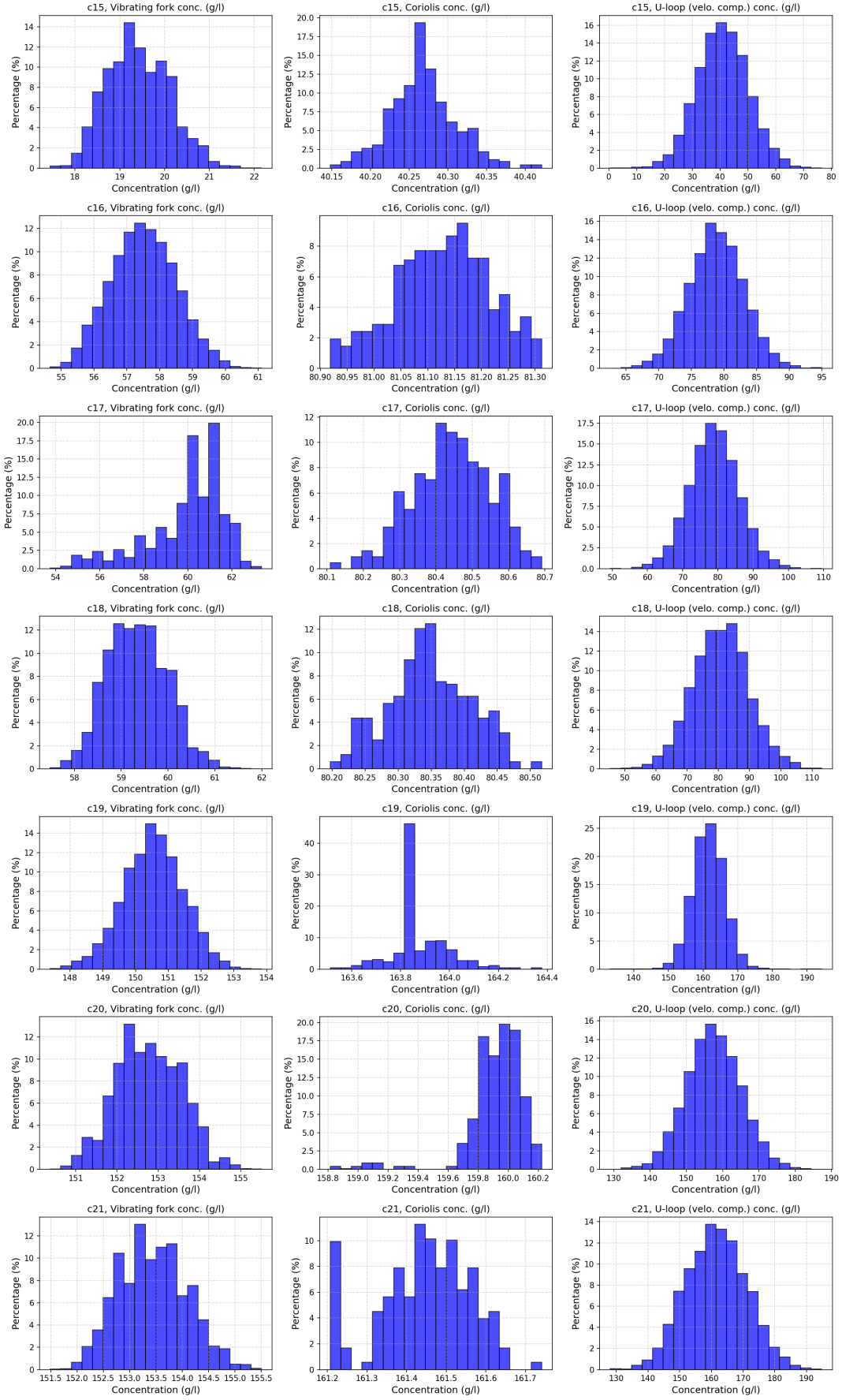

Figure B.6: C series histograms (test 15-21)

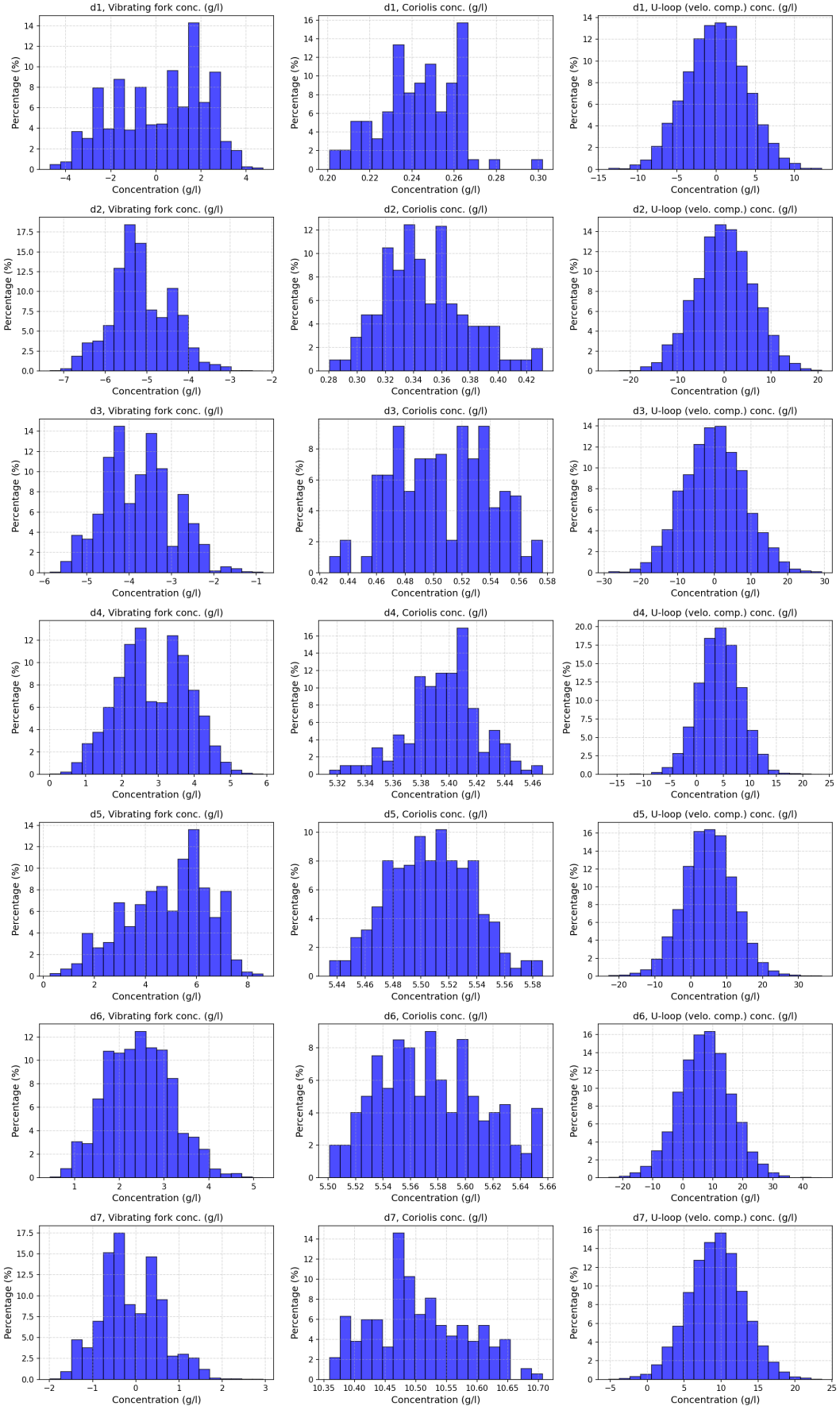

Figure B.7: D series histograms (test 1-7)

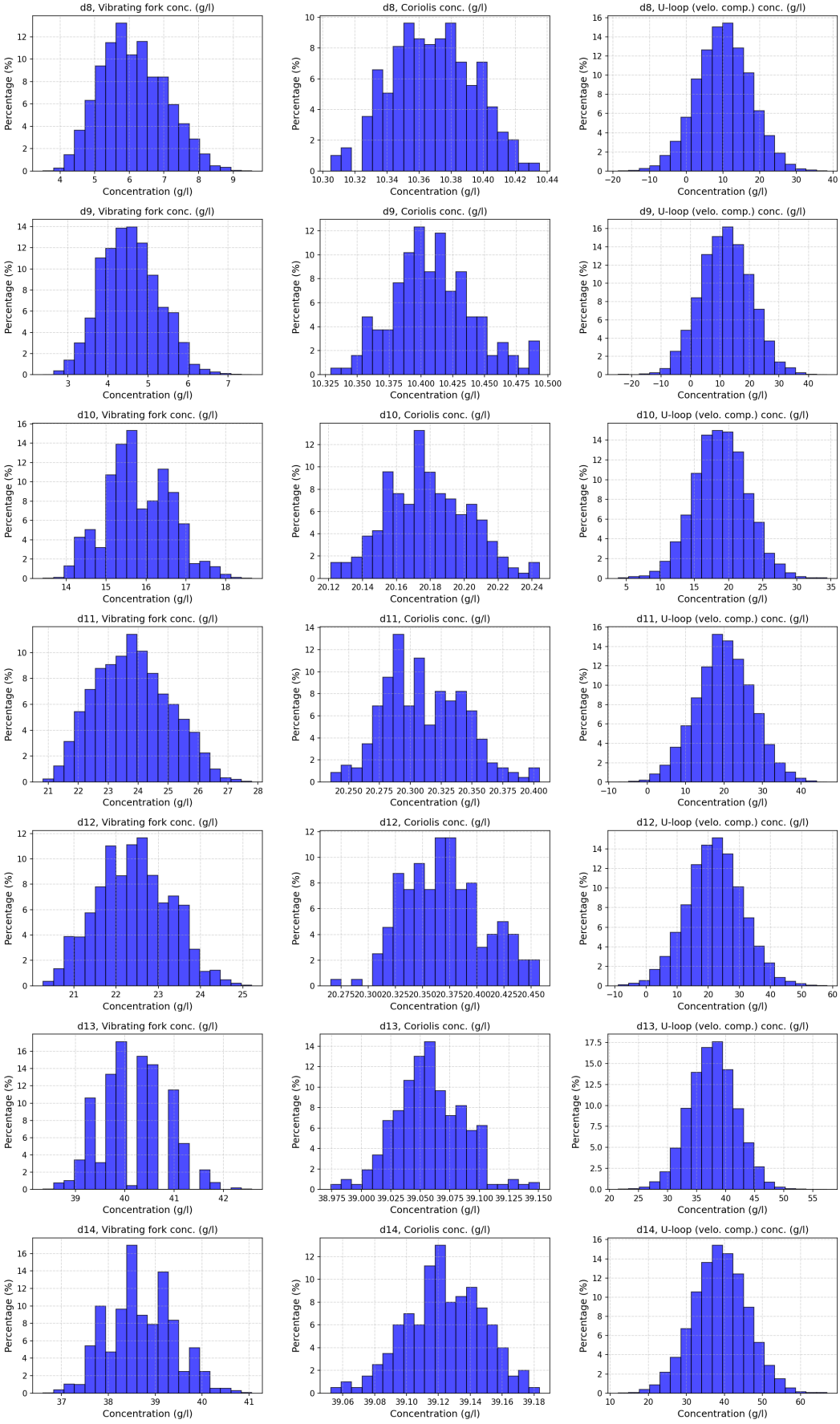

Figure B.8: D series histograms (test 8-14)

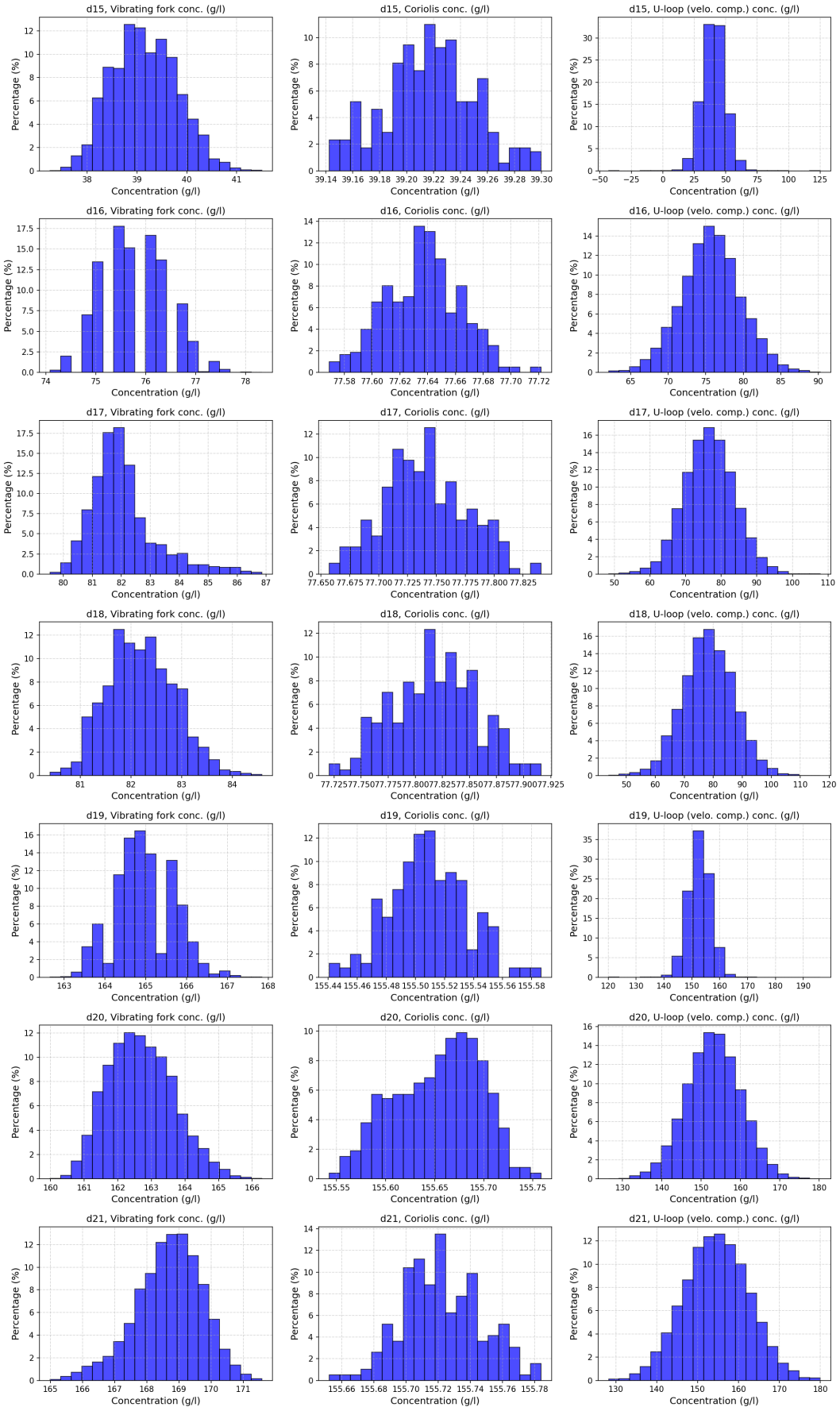

Figure B.9: D series histograms (test 15-21)

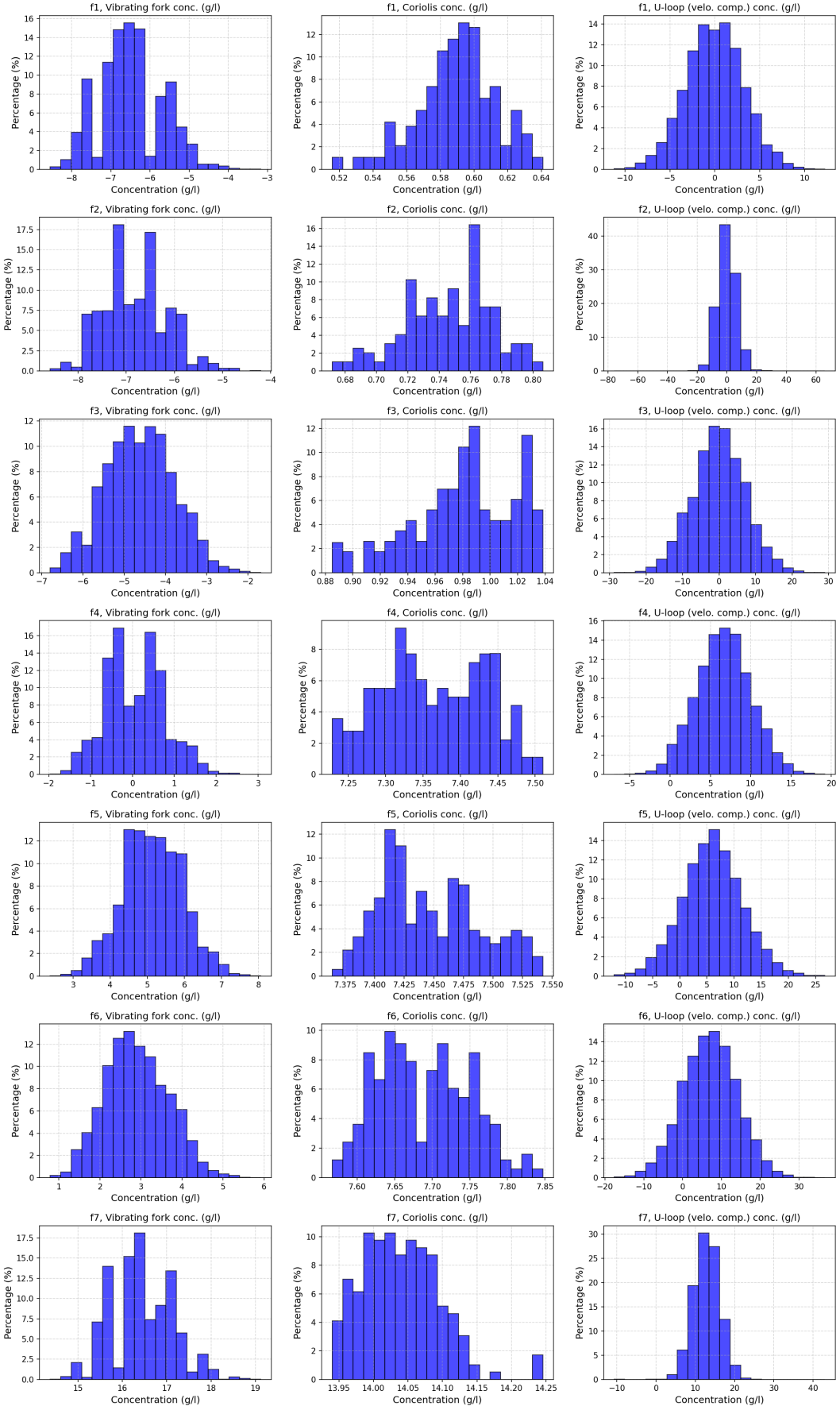

Figure B.10: F series histograms (test 1-7)

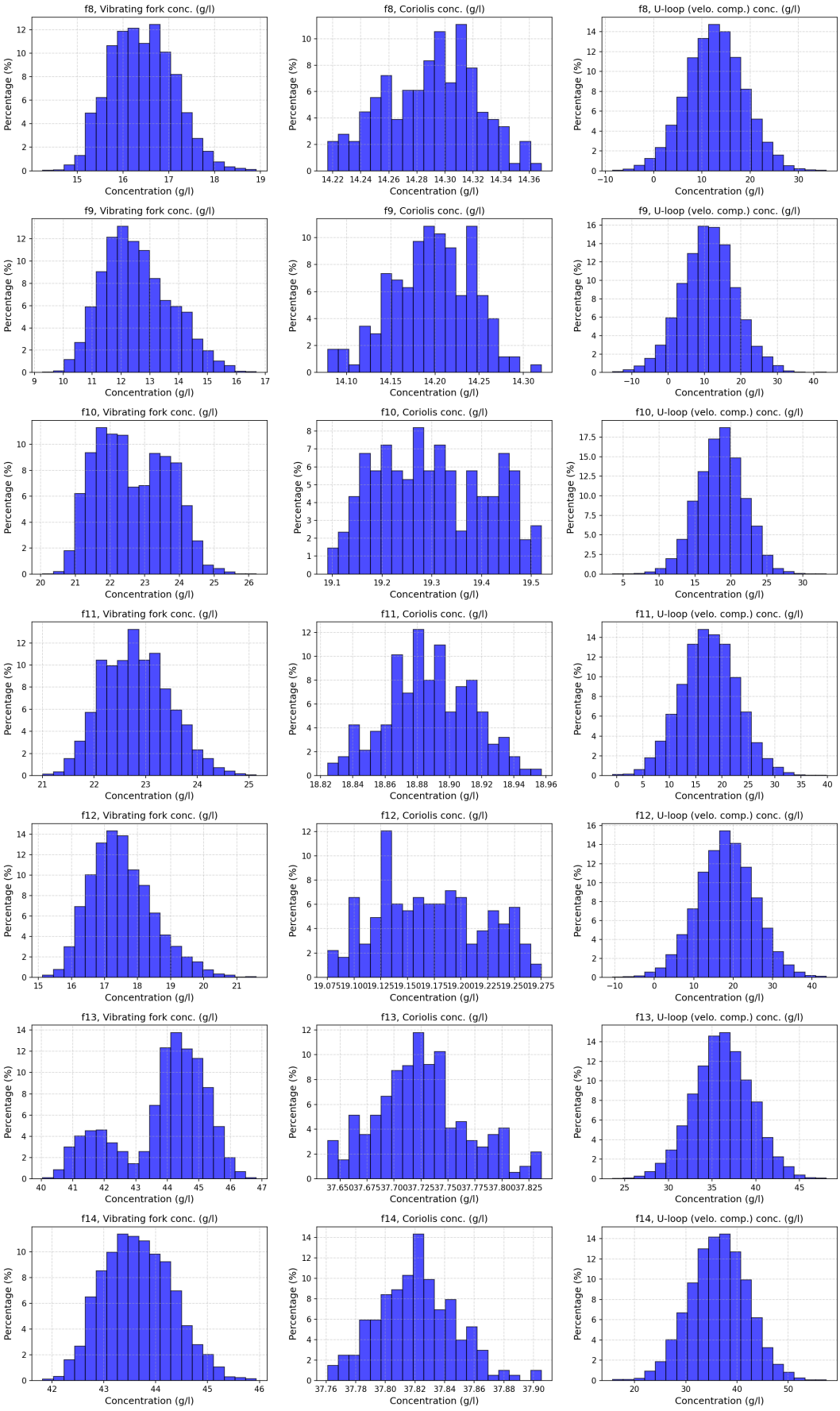

Figure B.11: F series histograms (test 8-14)

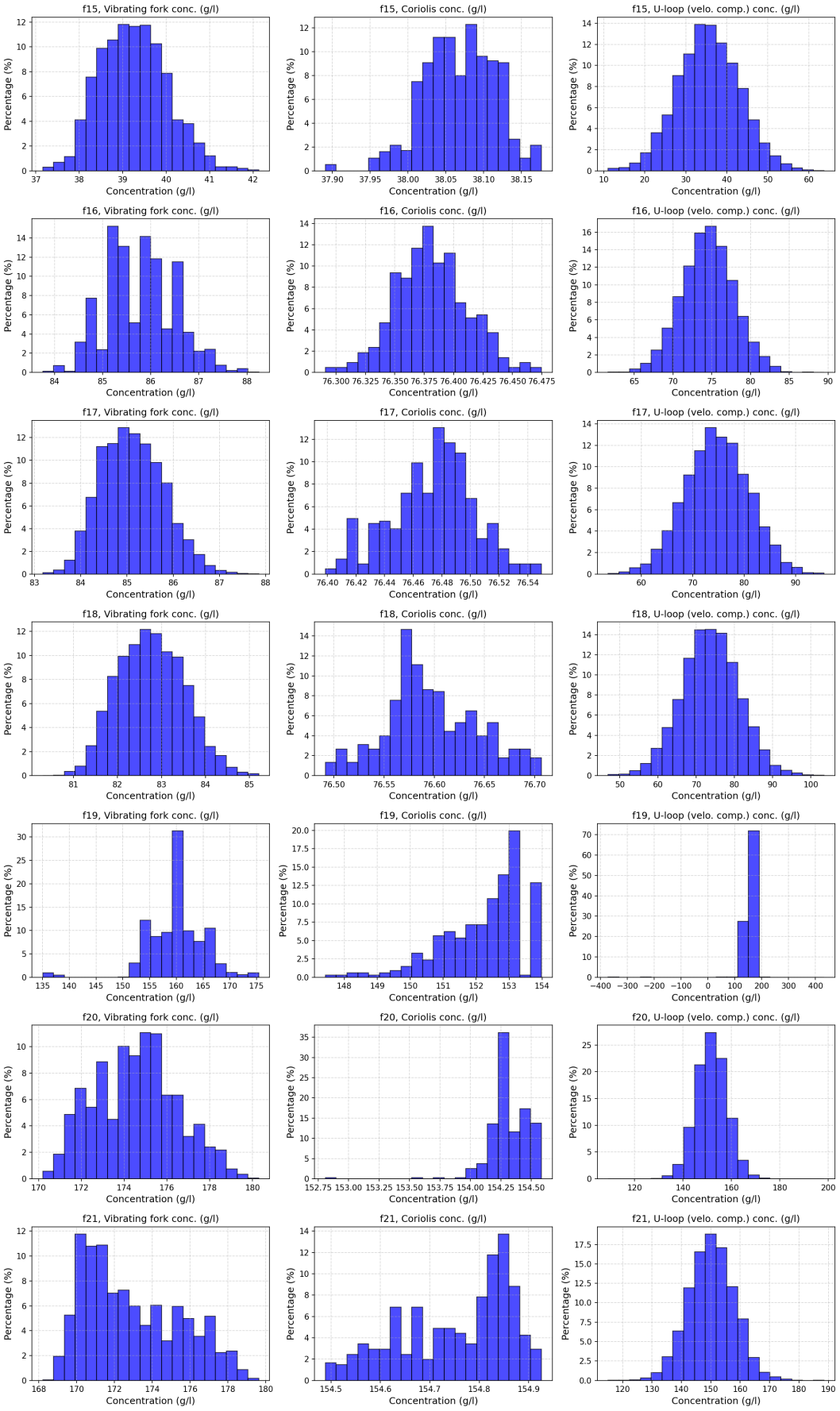

Figure B.12: F series histograms (test 15-21)

C

Scatter plots

Note: The range of the concentration axis is not the same for all methodologies. More precise methodologies display smaller ranges.

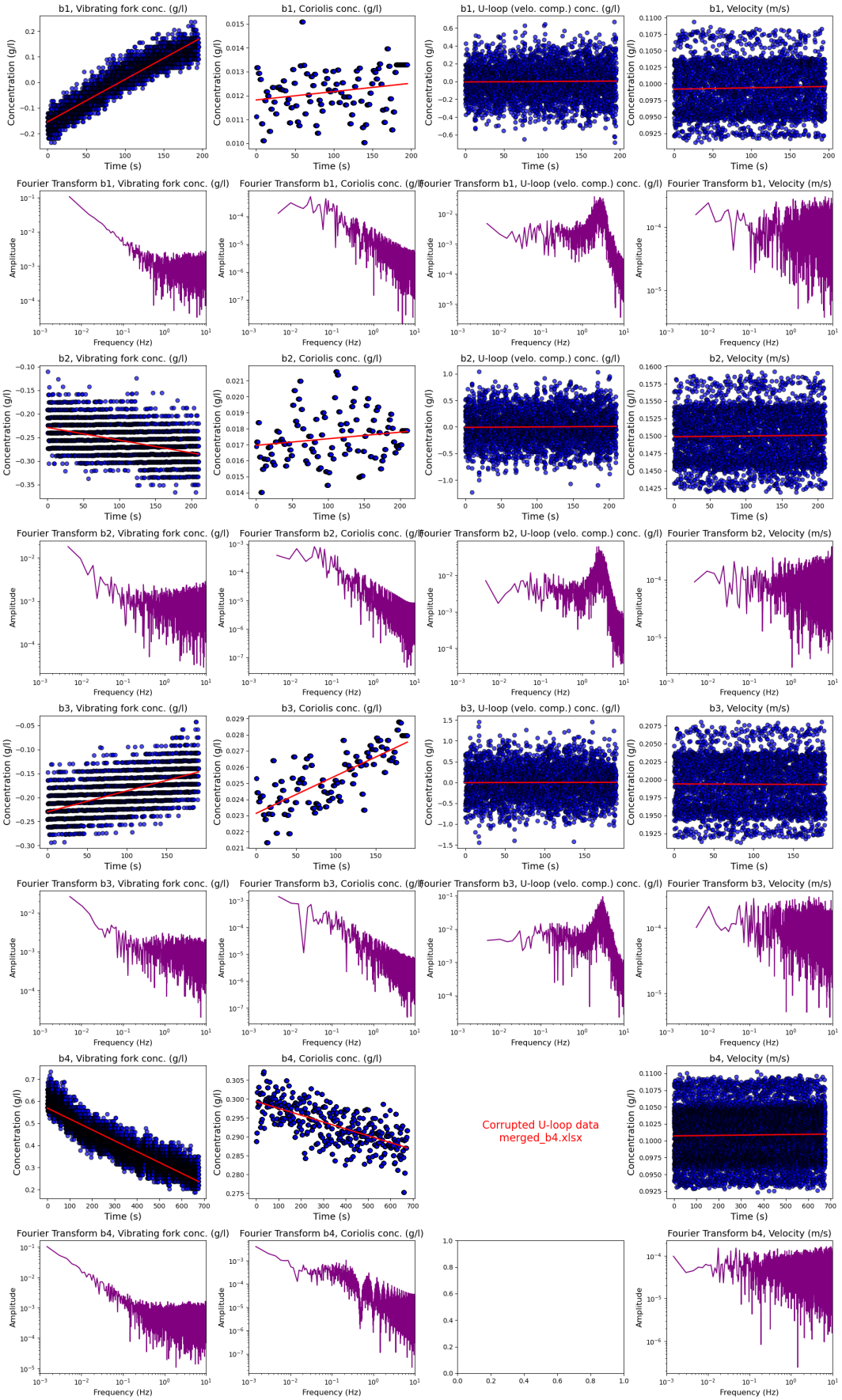

Figure C.1: B series time-series and Fourier transfer (b1-b4)

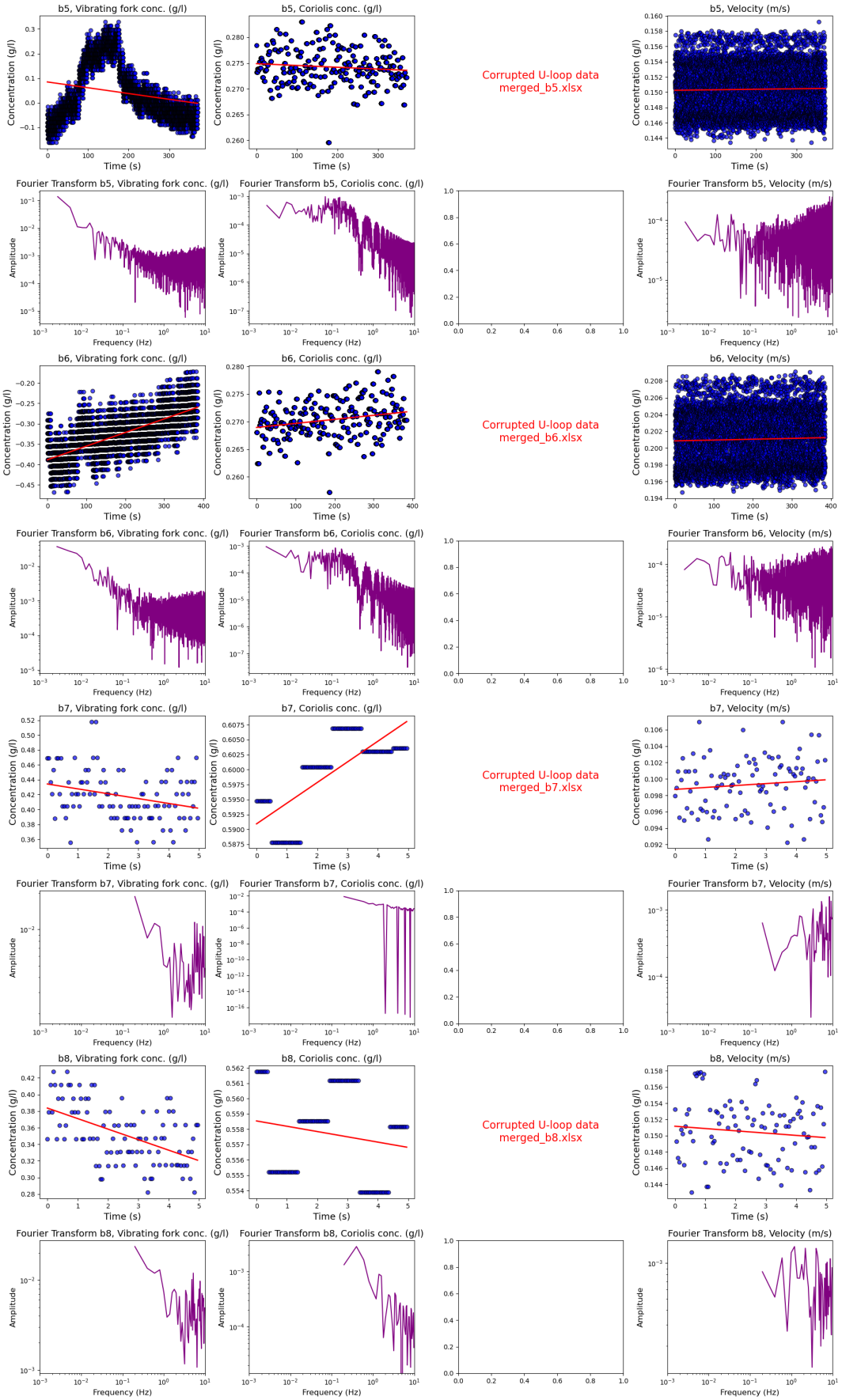

Figure C.2: B series time-series and Fourier transfer (b5-b8)

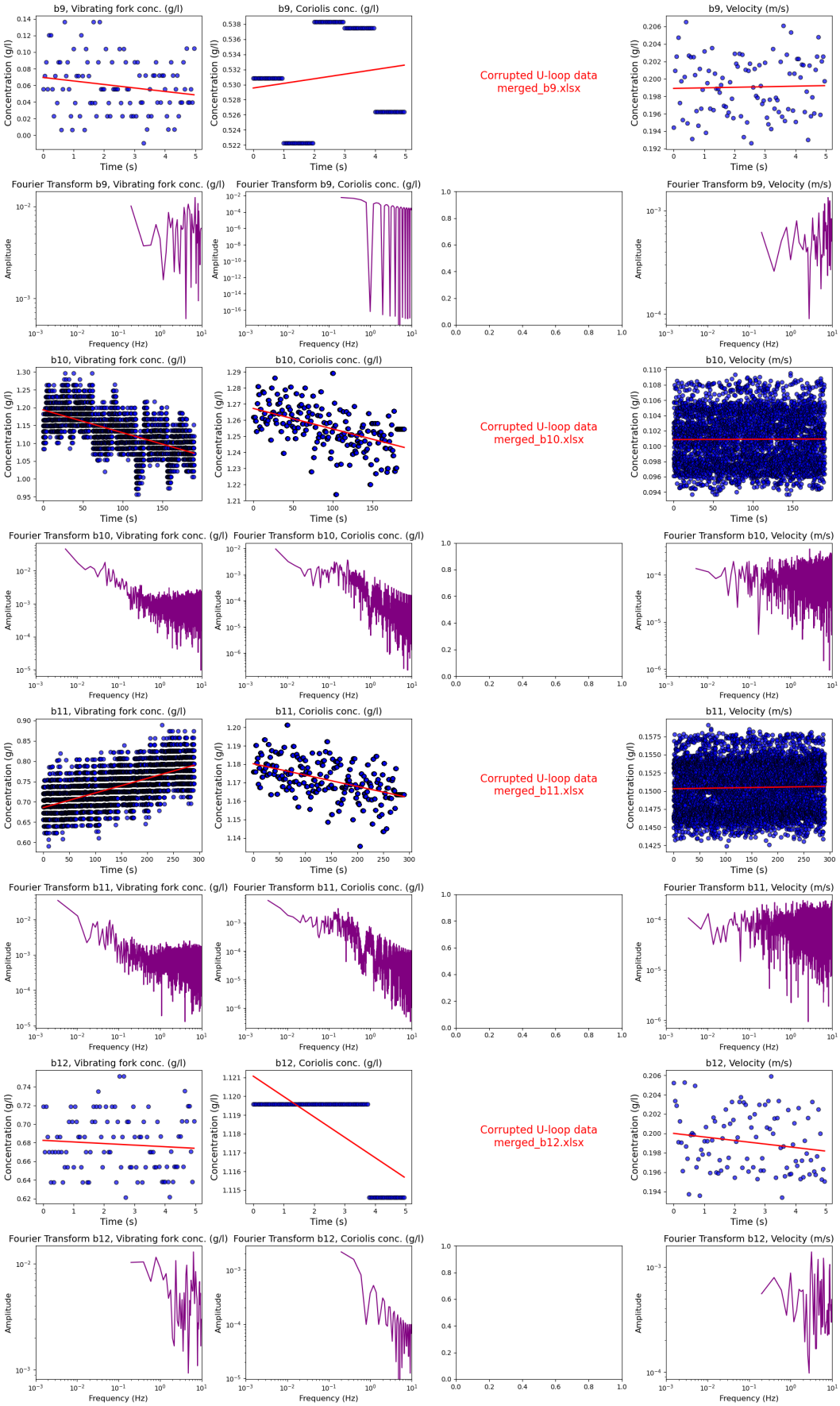

Figure C.3: B series time-series and Fourier transfer (b9-b12)

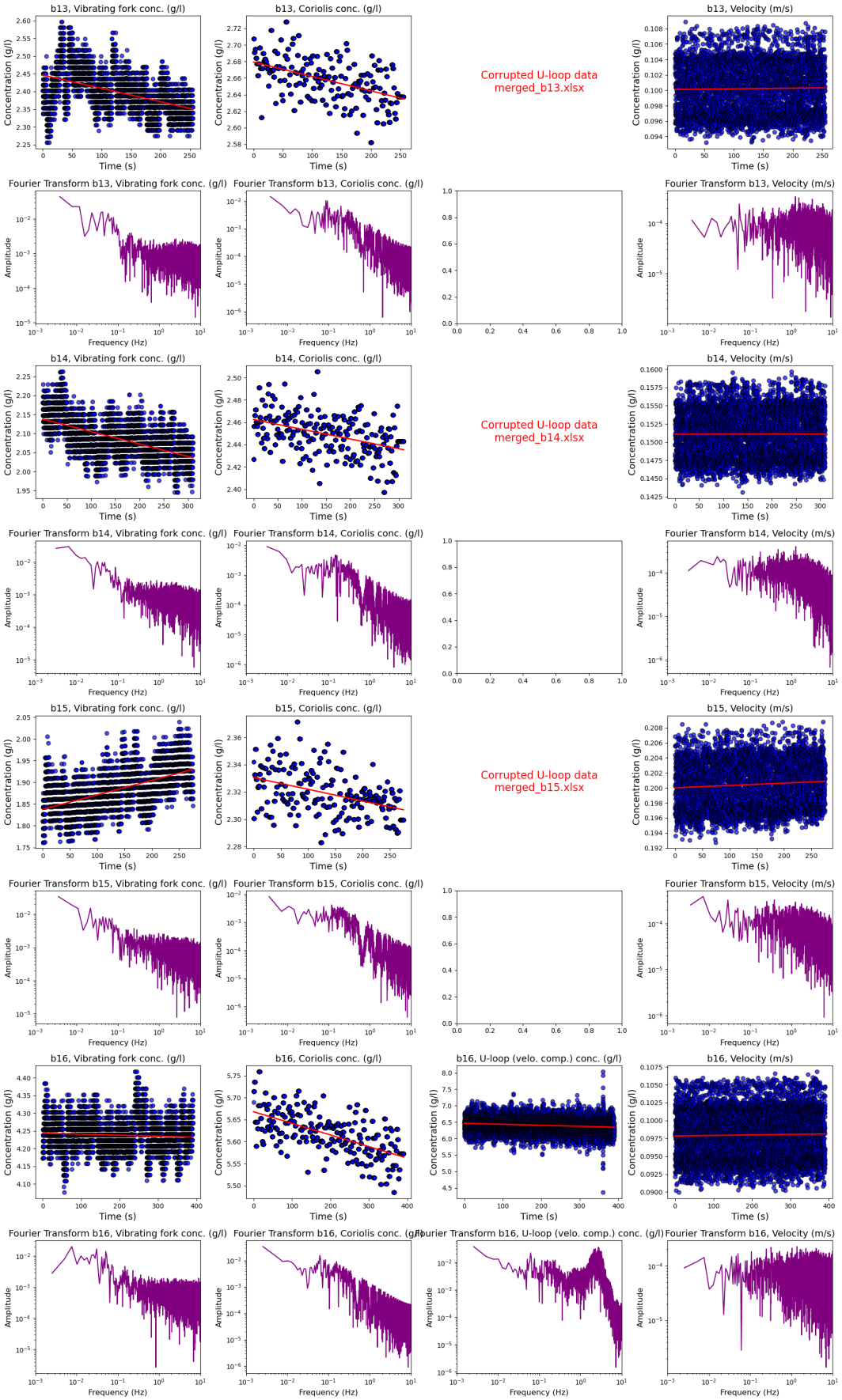

Figure C.4: B series time-series and Fourier transfer (b13-b16)

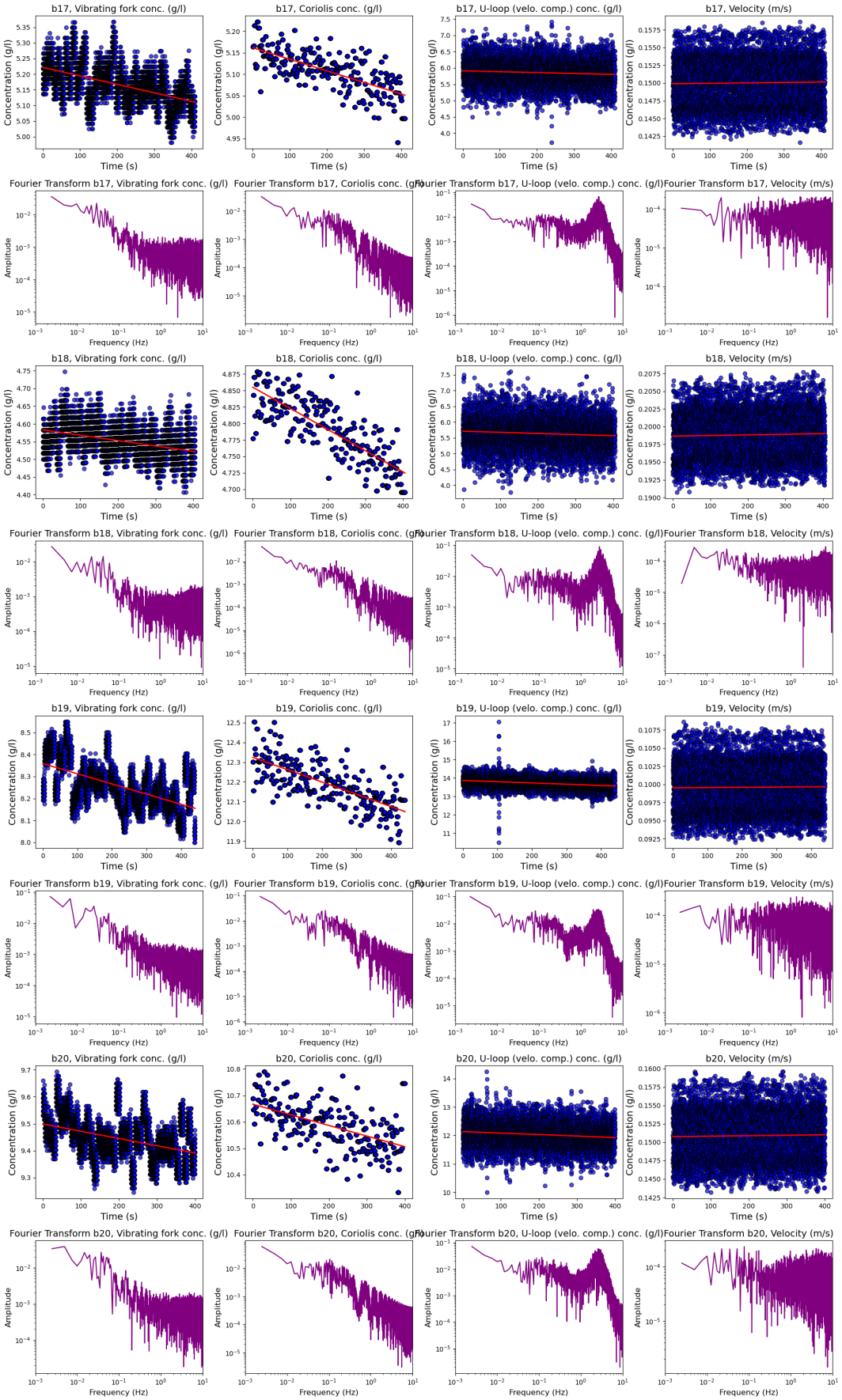

Figure C.5: B series time-series and Fourier transfer (b17-b20)

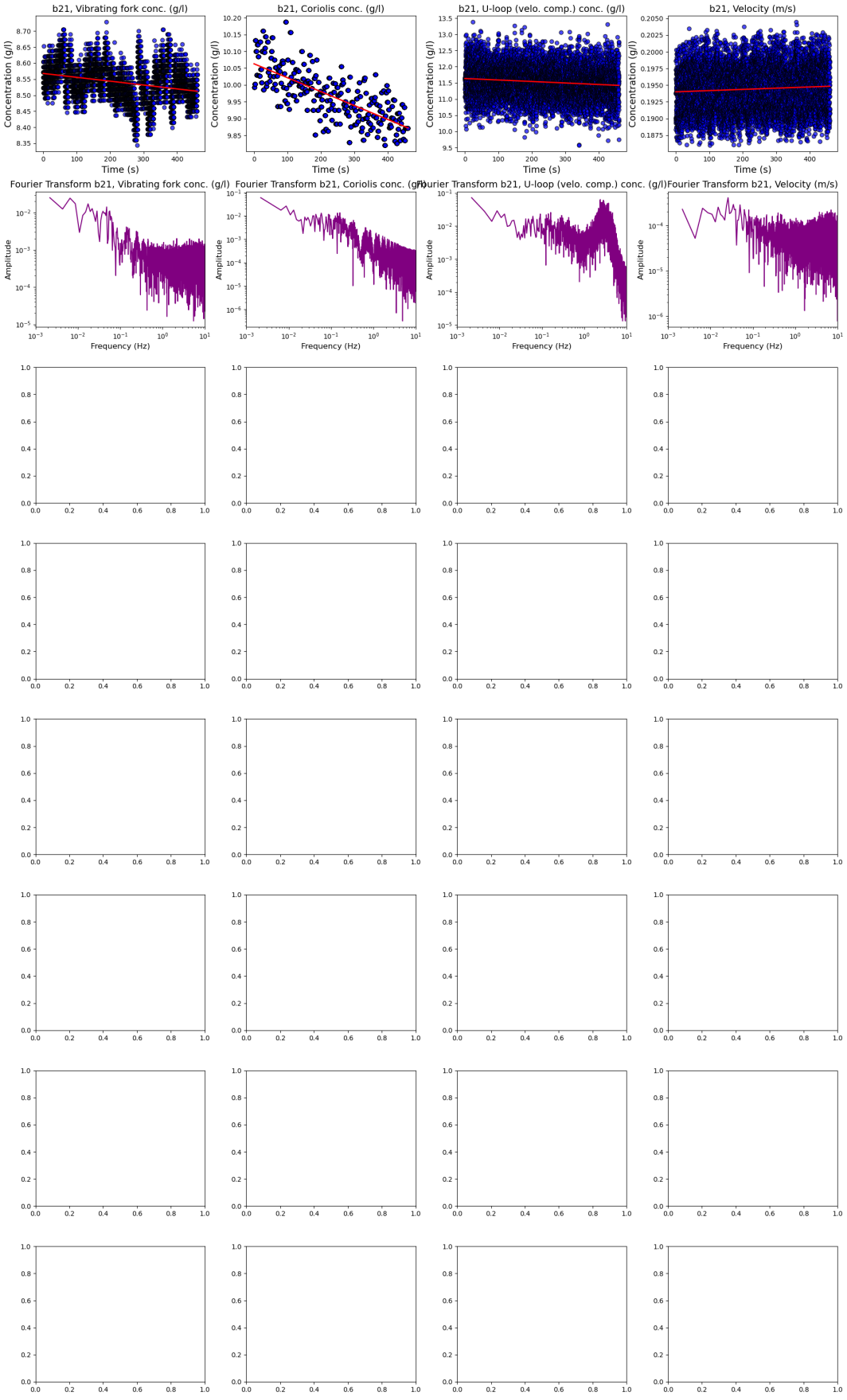

Figure C.6: B series time-series and Fourier transfer (b21)

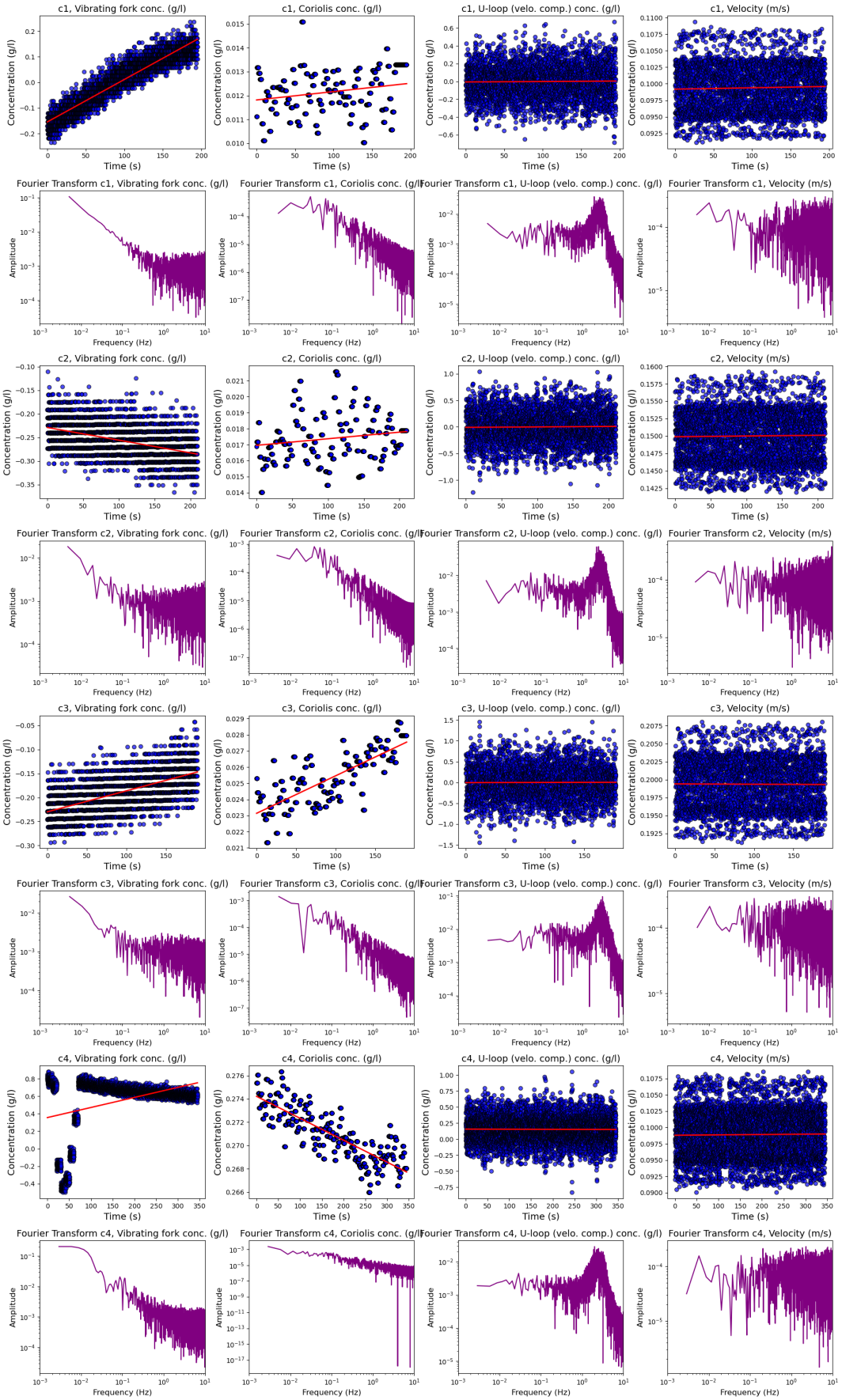

Figure C.7: C series time-series and Fourier transfer (c1-c4)

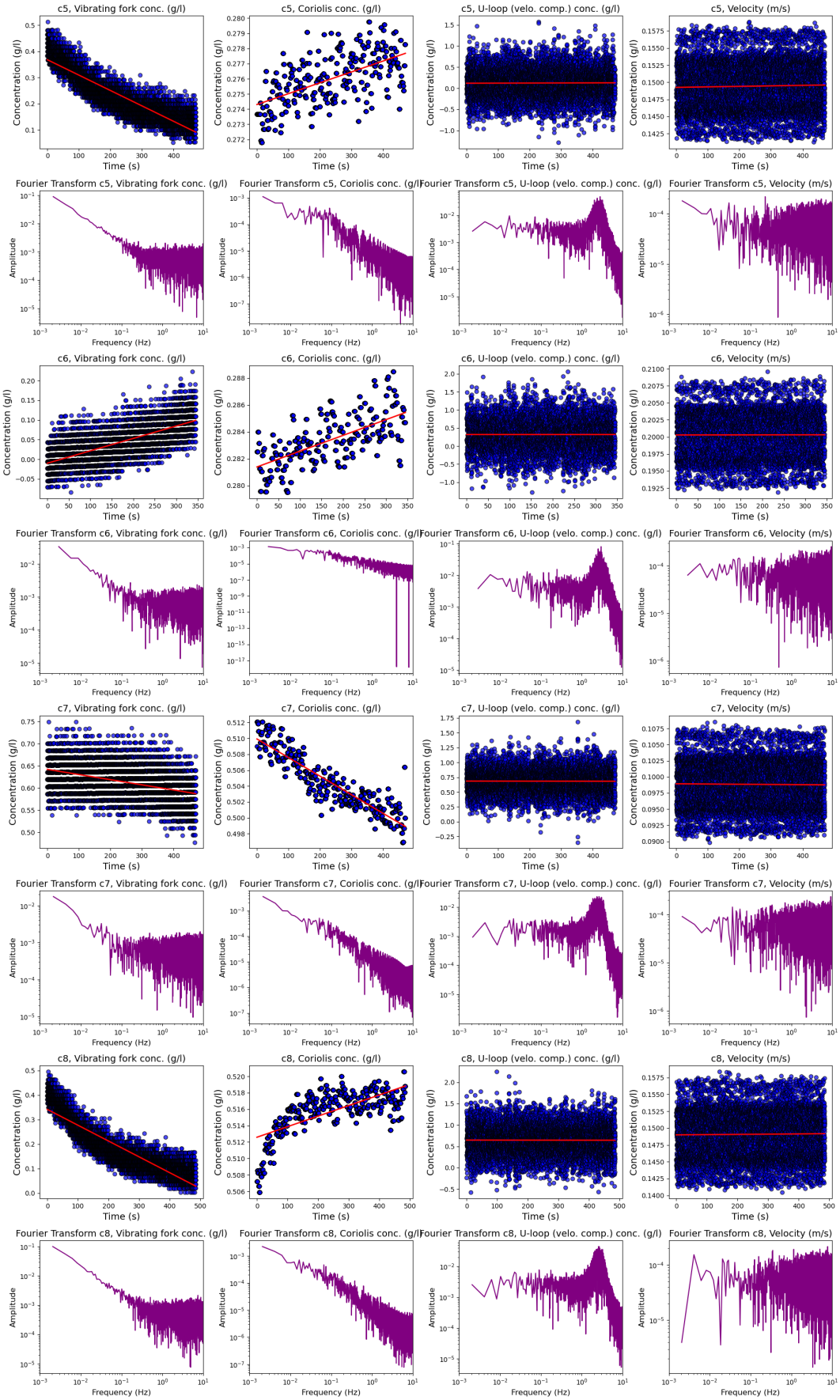

Figure C.8: C series time-series and Fourier transfer (c5-c8)

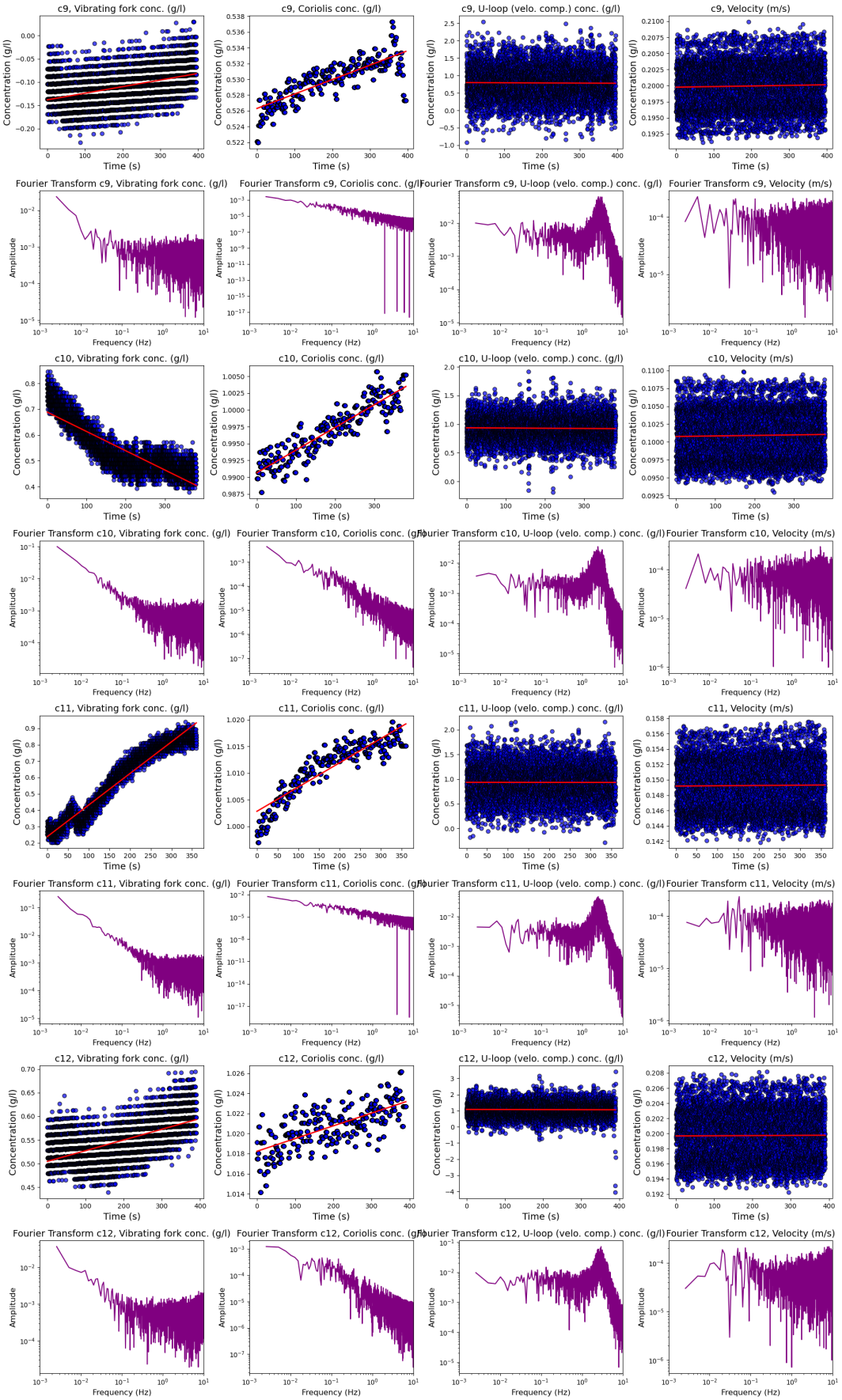

Figure C.9: C series time-series and Fourier transfer (c9-c12)

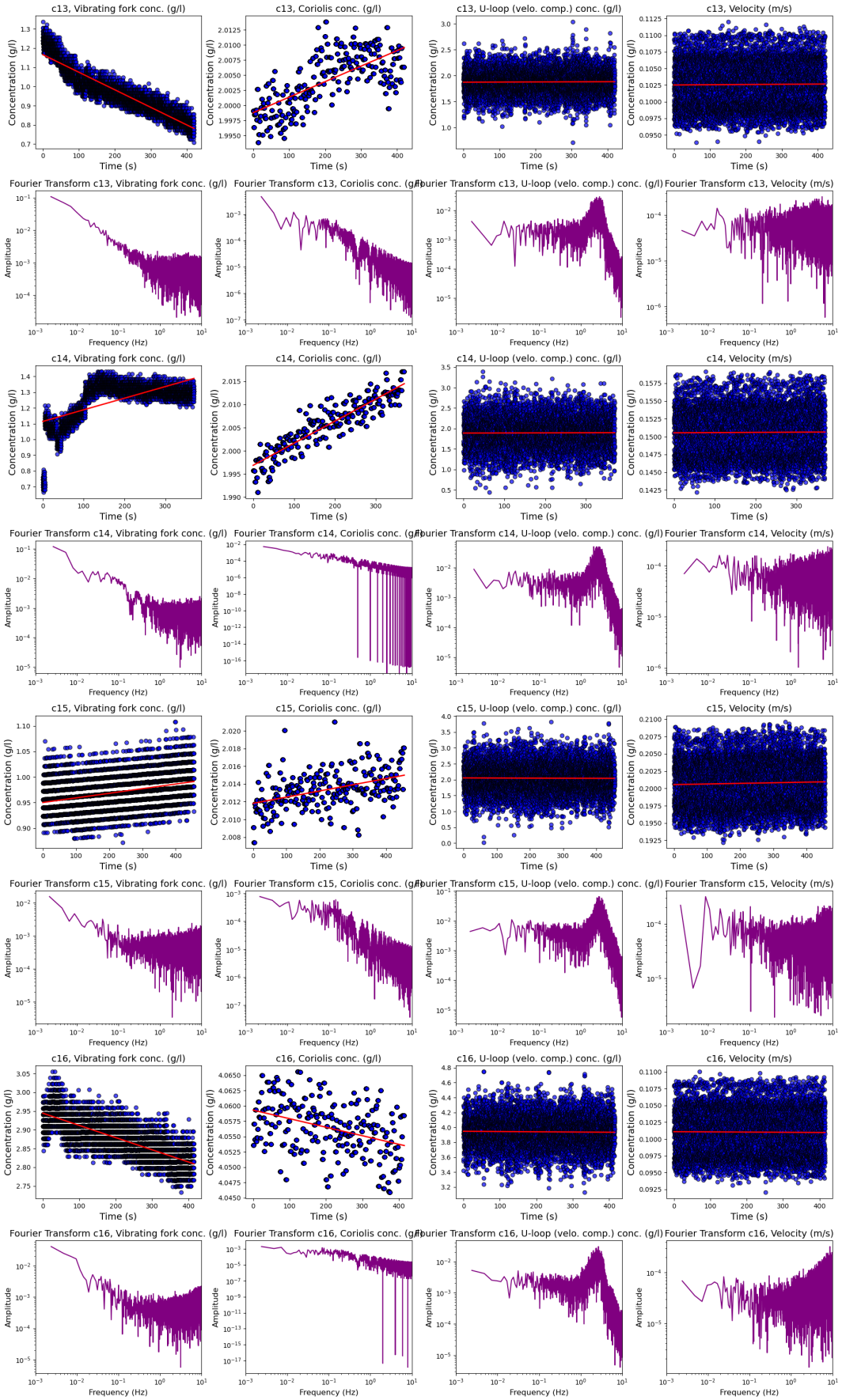

Figure C.10: C series time-series and Fourier transfer (c13-c16)

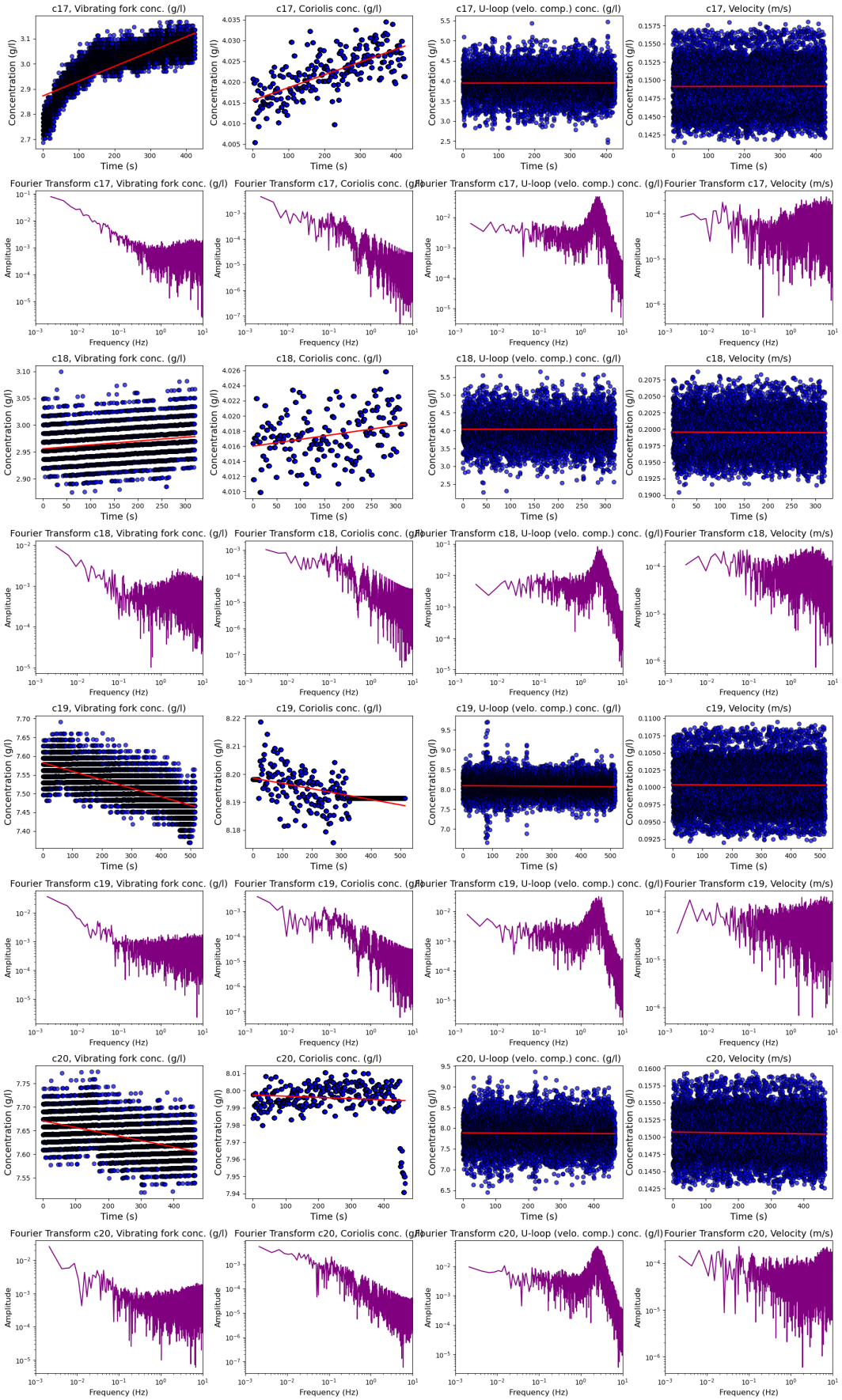

Figure C.11: C series time-series and Fourier transfer (c17-c20)

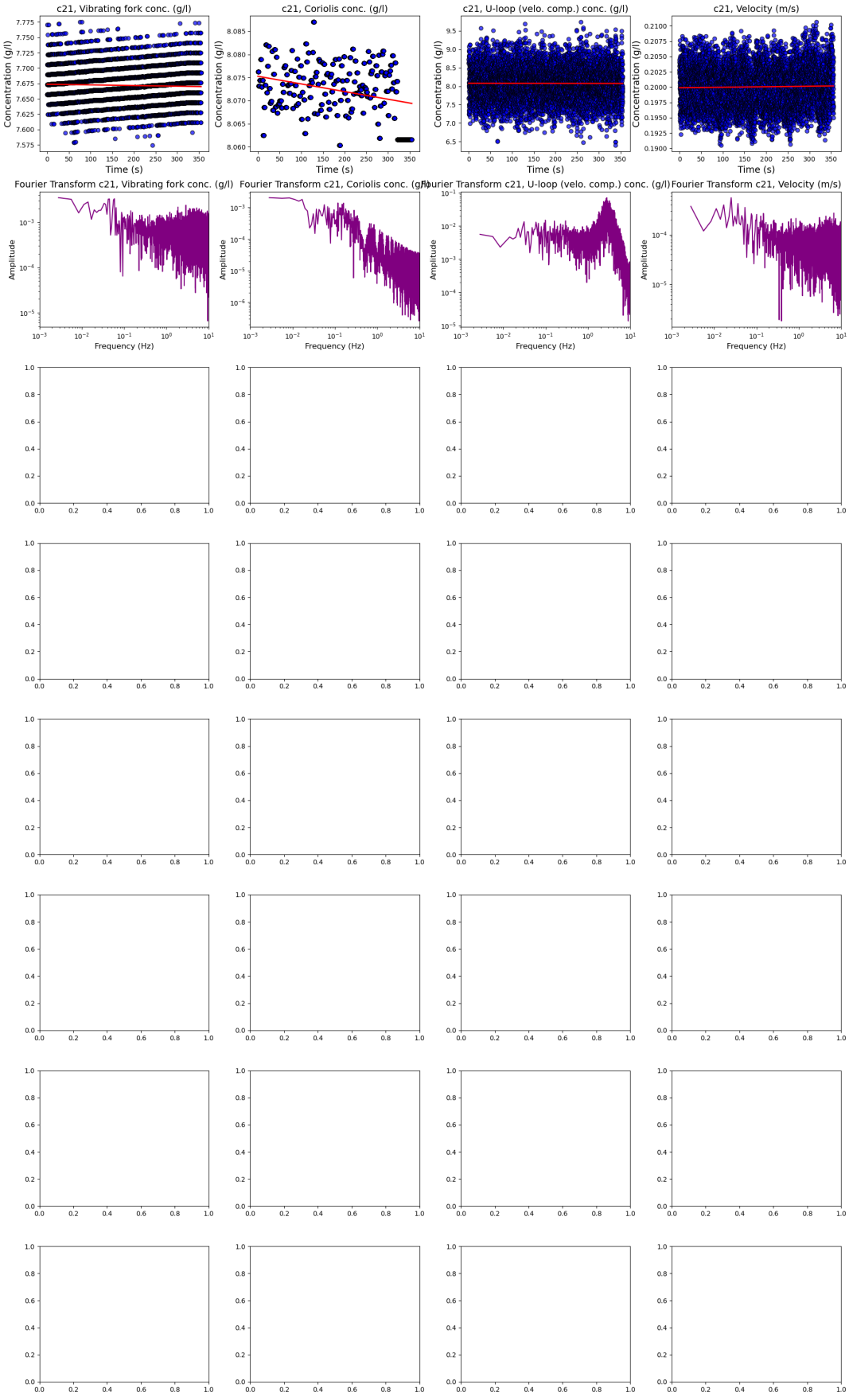

Figure C.12: C series time-series and Fourier transfer (c21)

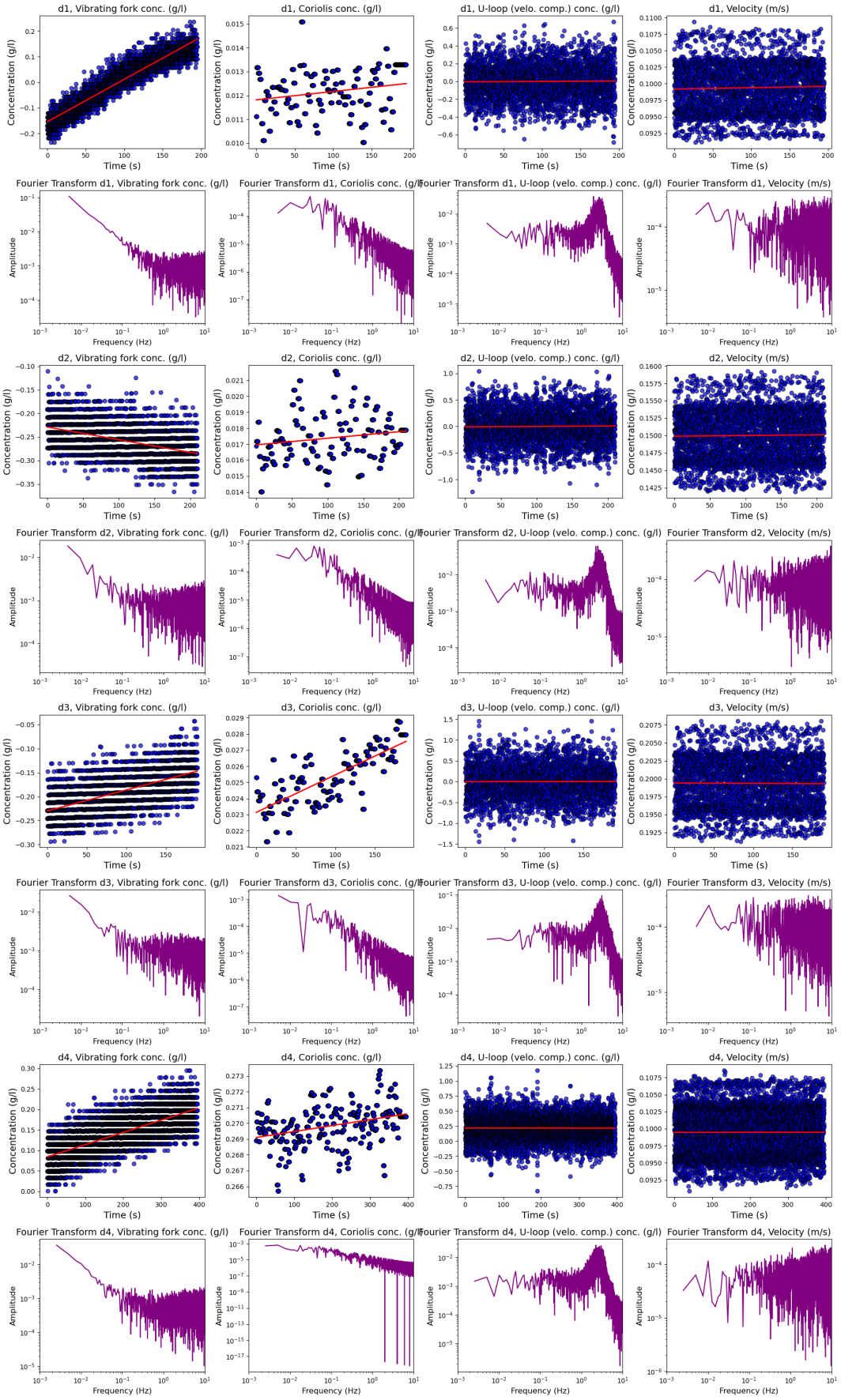

Figure C.13: D series time-series and Fourier transfer (d1-d4)

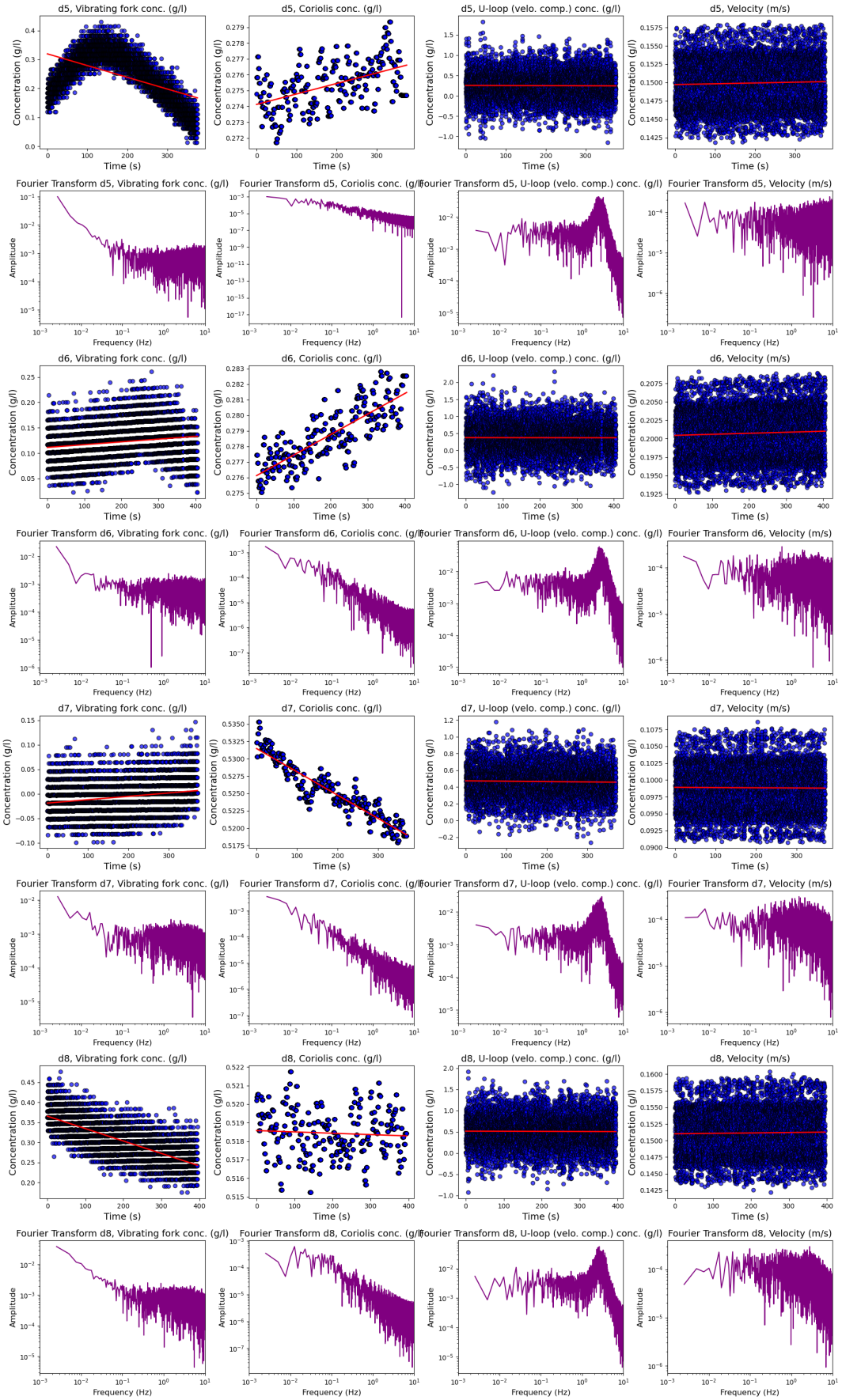

Figure C.14: D series time-series and Fourier transfer (d5-d8)

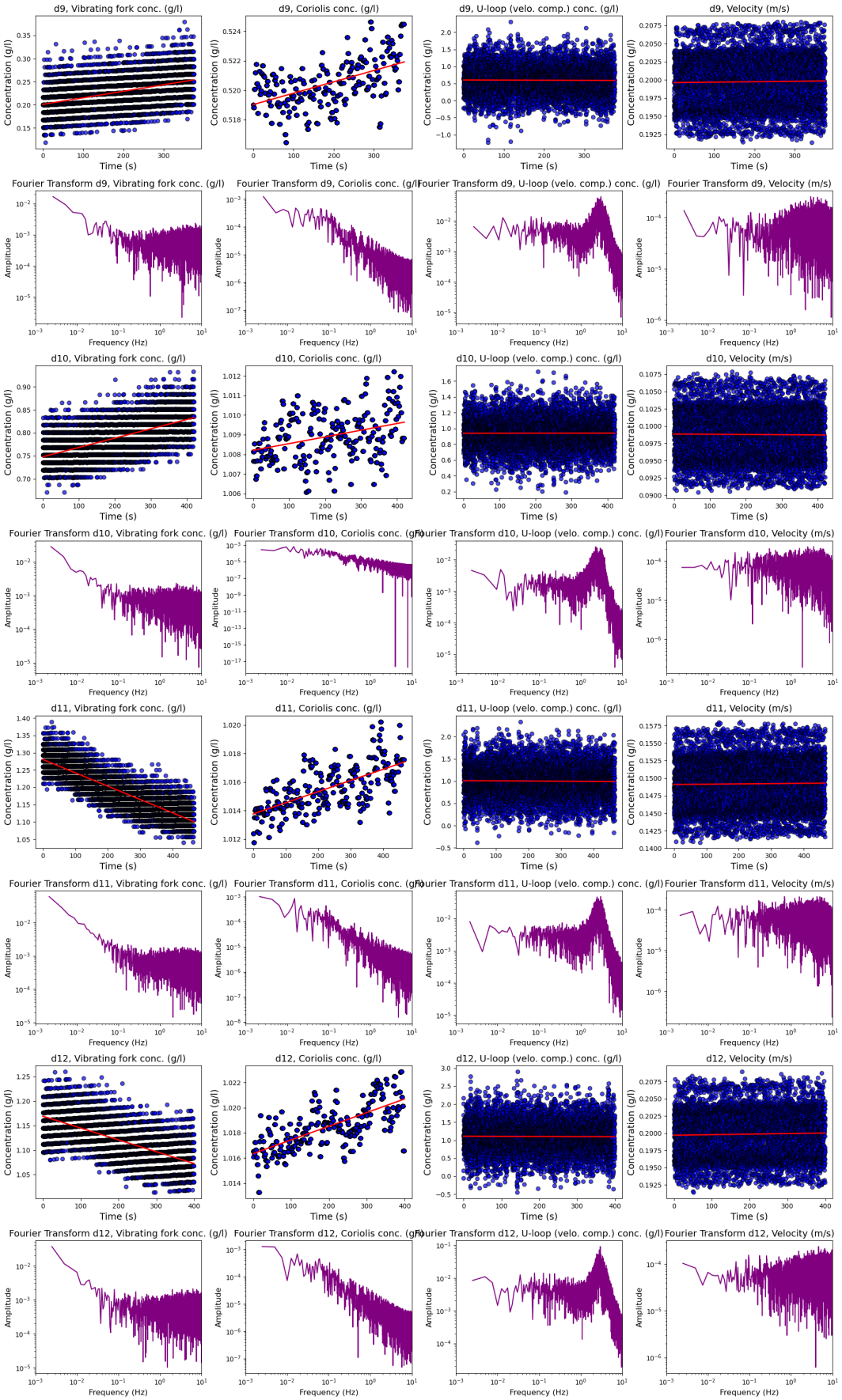

Figure C.15: D series time-series and Fourier transfer (d9-d12)

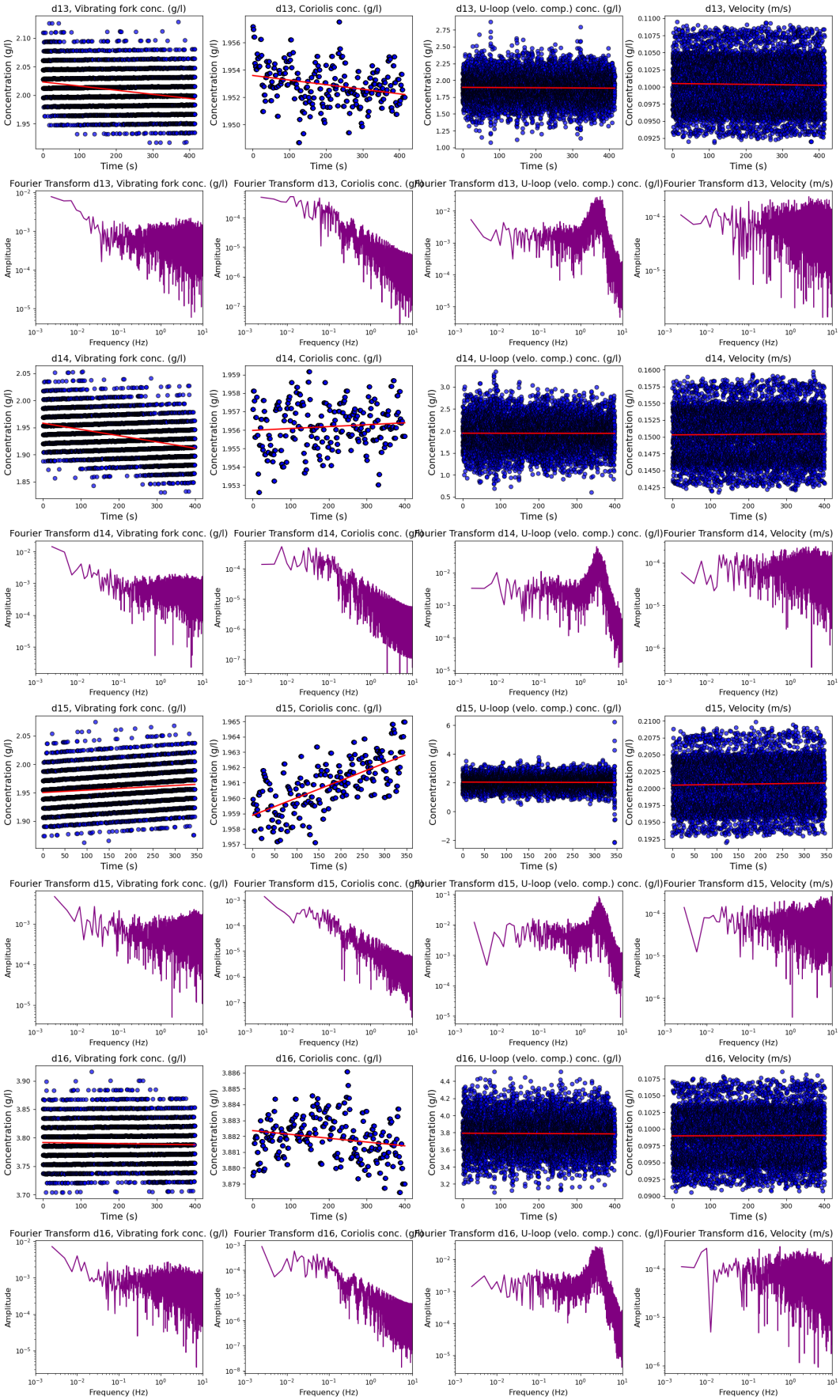

Figure C.16: D series time-series and Fourier transfer (d13-d16)

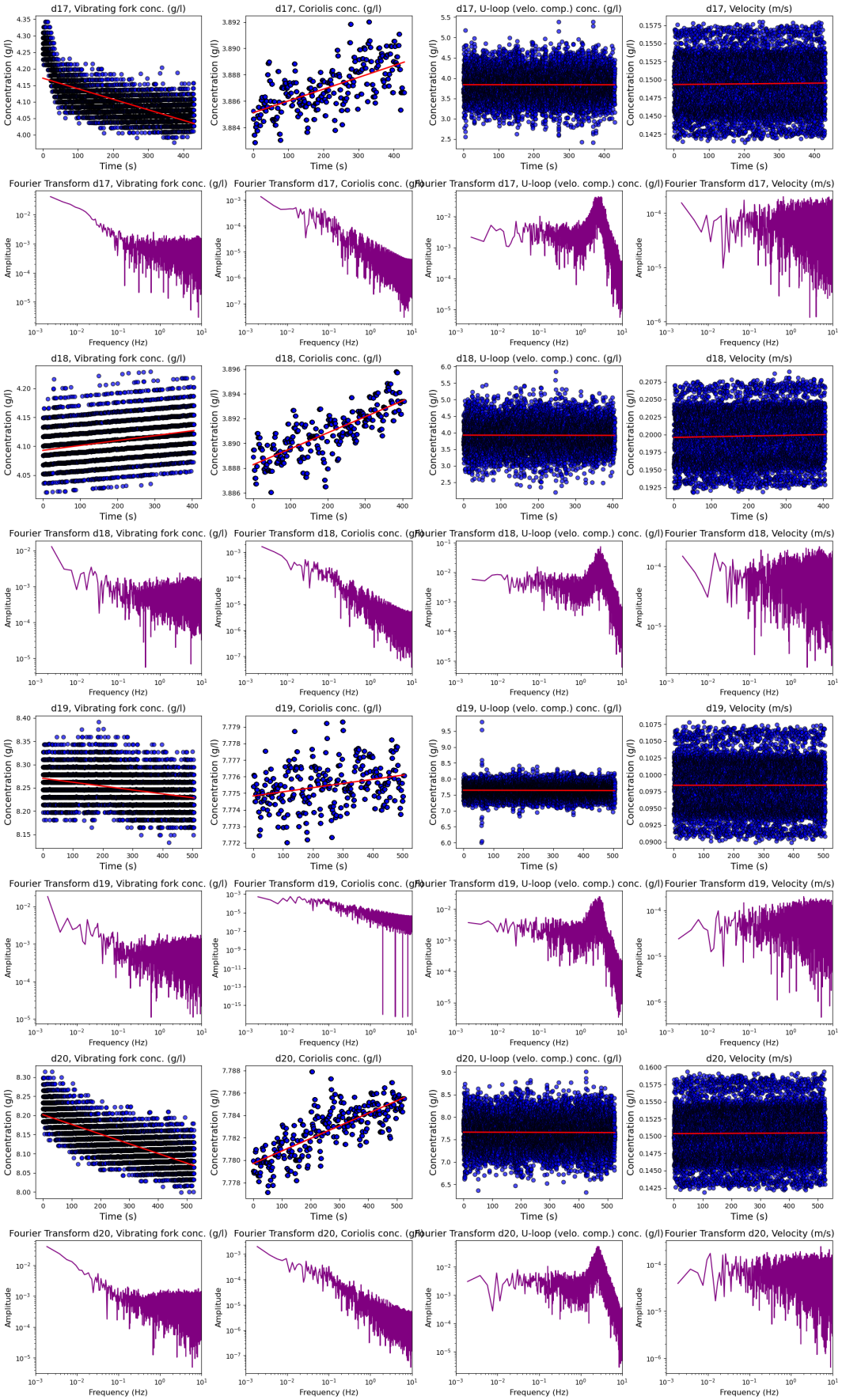

Figure C.17: D series time-series and Fourier transfer (d17-d20)

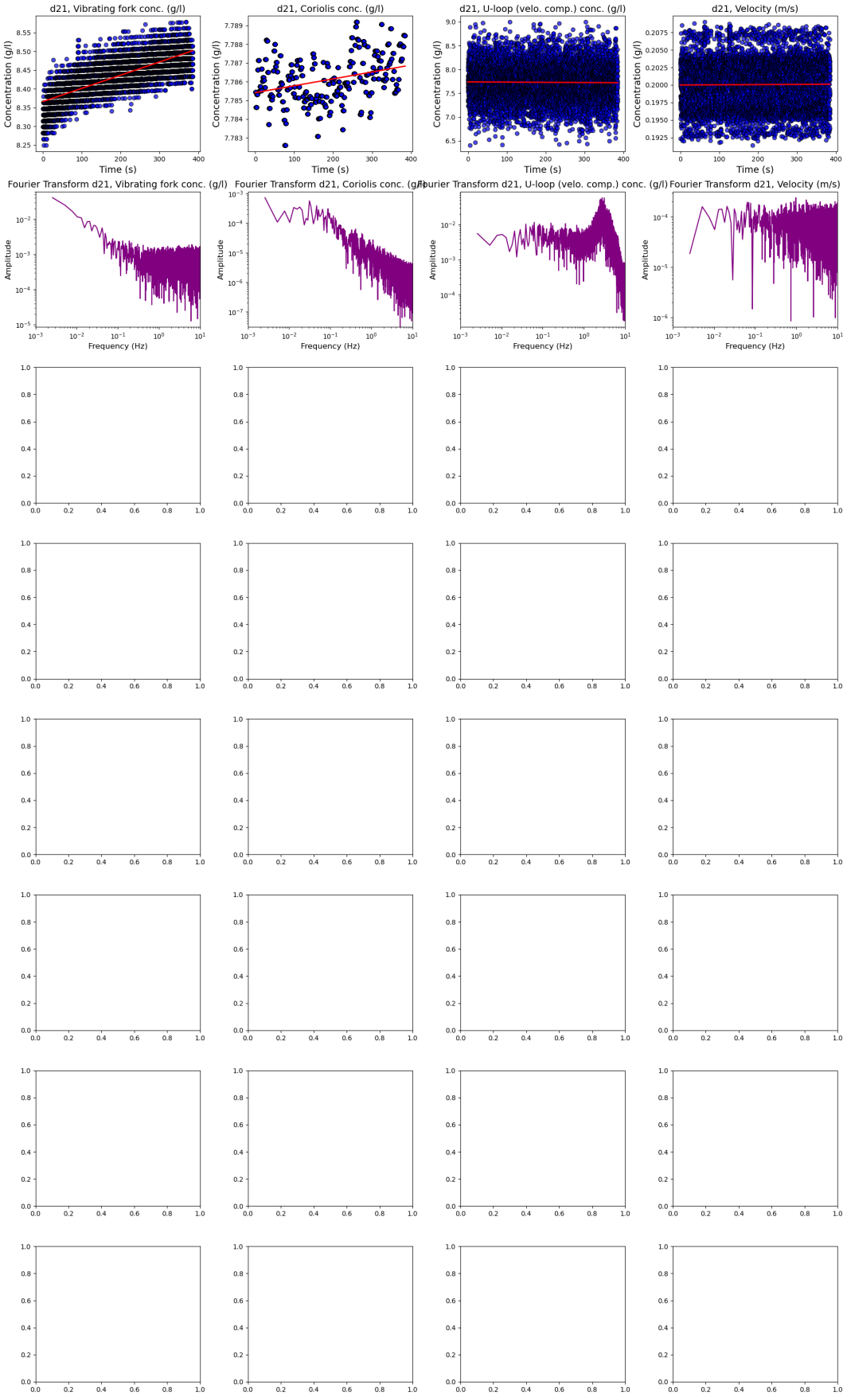

Figure C.18: D series time-series and Fourier transfer (d21)

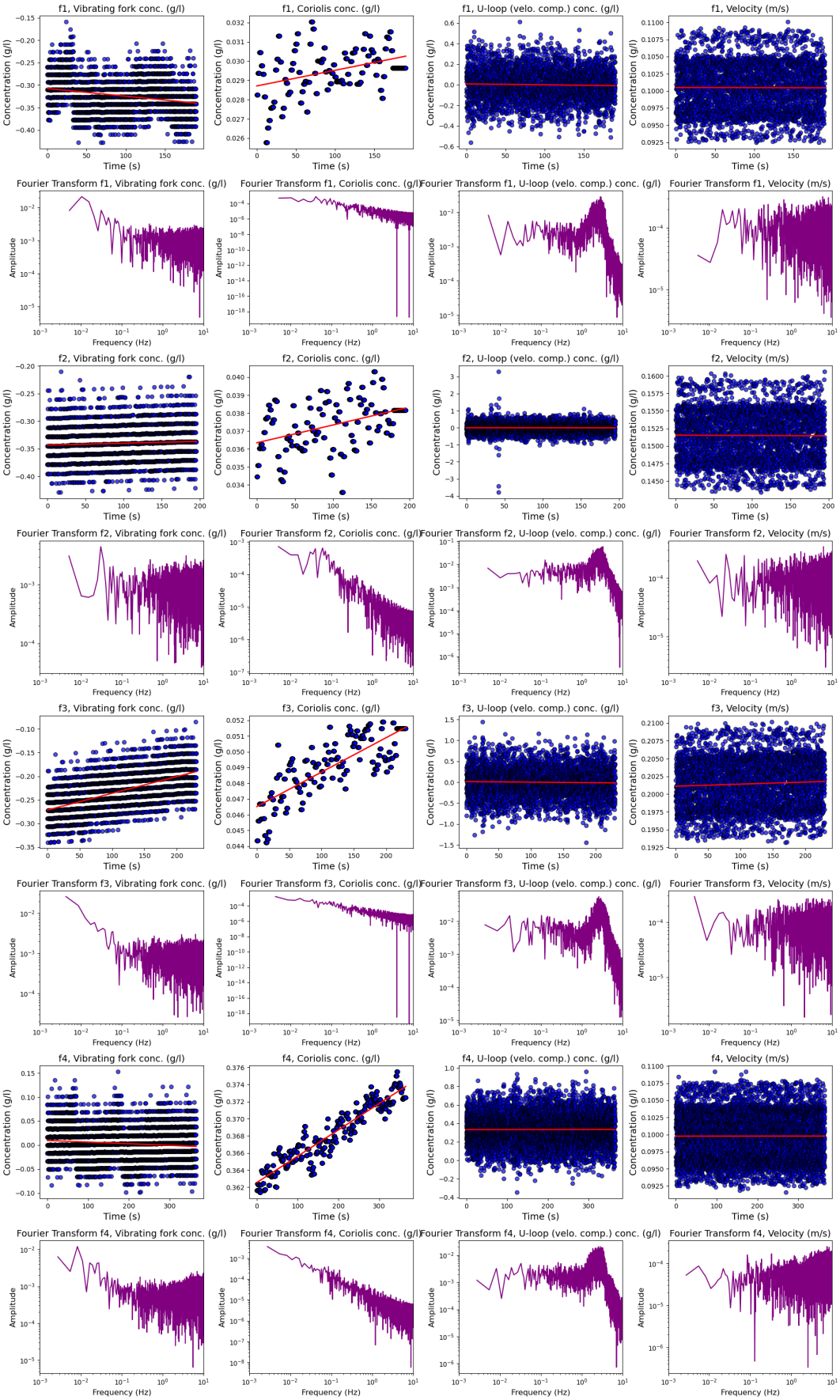

Figure C.19: F series time-series and Fourier transfer (f1-f4)

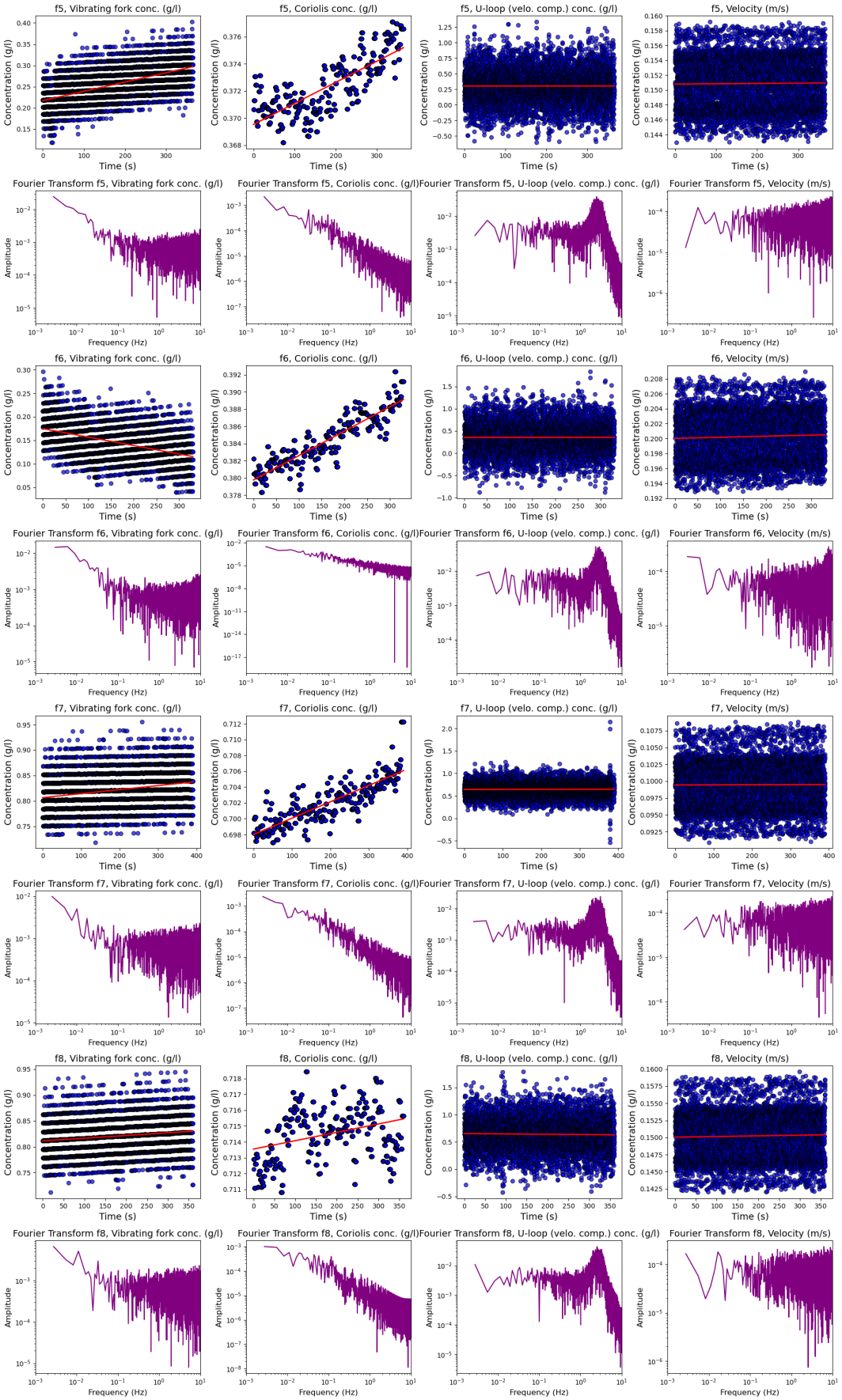

Figure C.20: F series time-series and Fourier transfer (f5-f8)

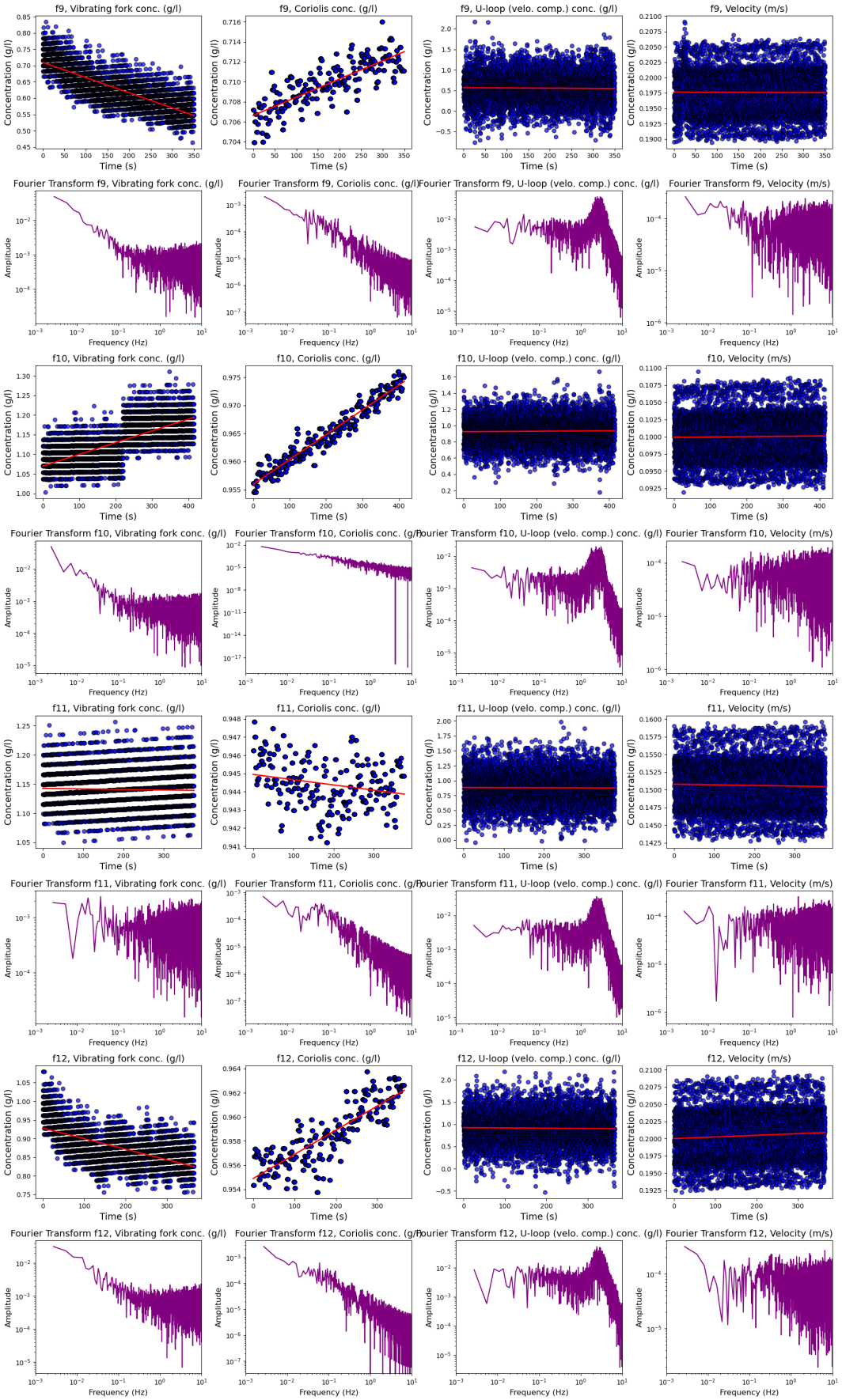

Figure C.21: F series time-series and Fourier transfer (f9-f12)

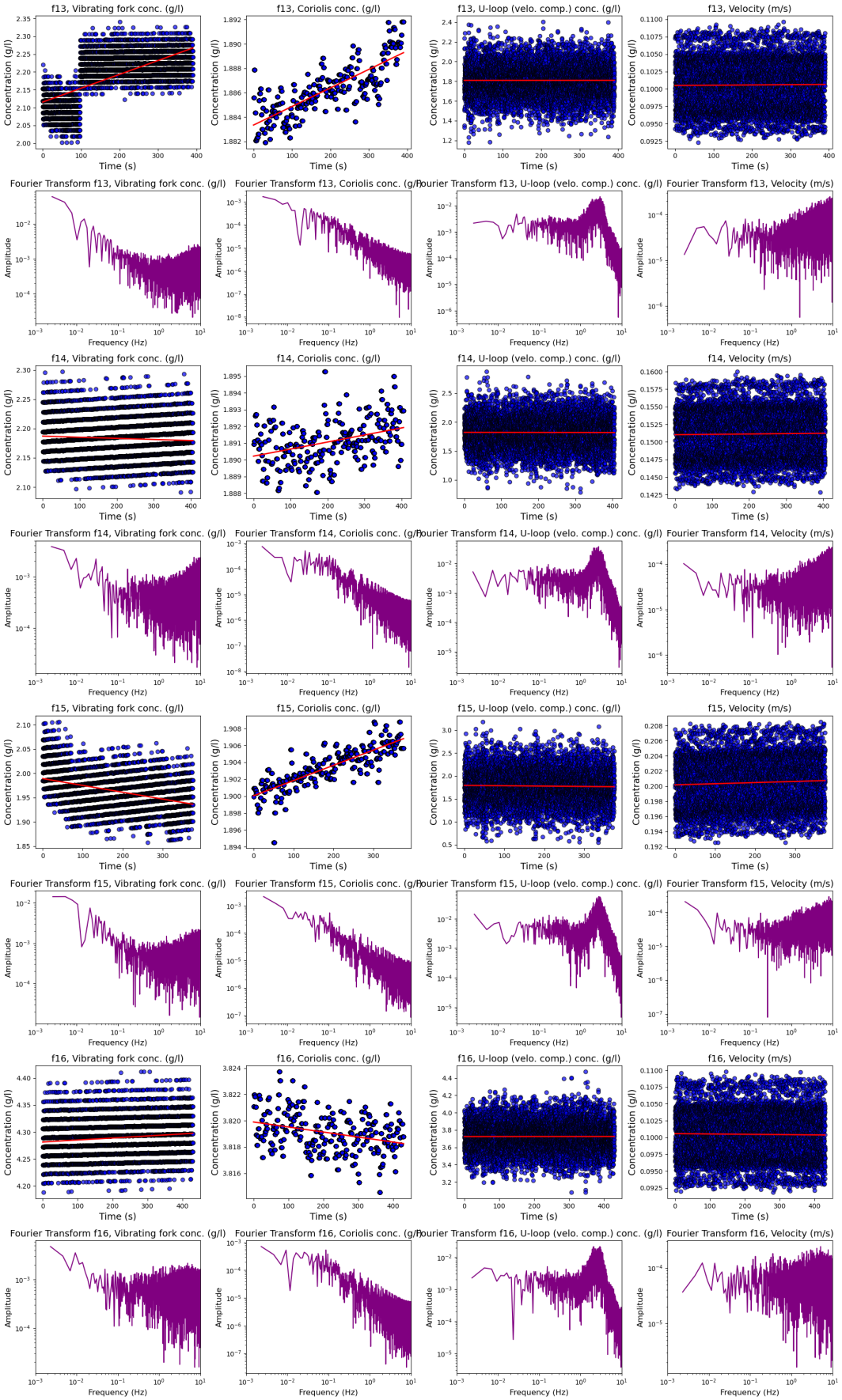

Figure C.22: F series time-series and Fourier transfer (f13-f16)

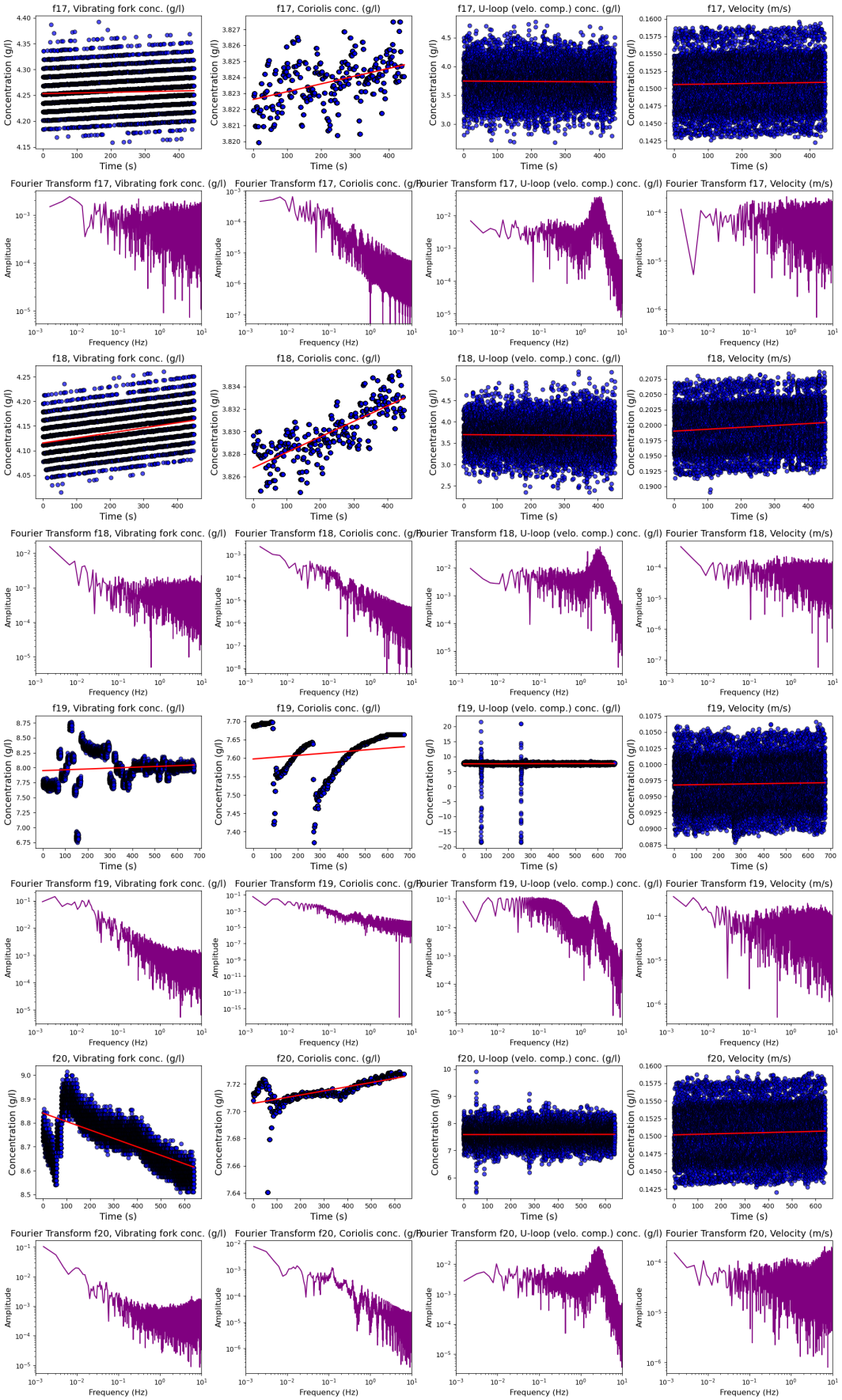

Figure C.23: F series time-series and Fourier transfer (f17-f20)

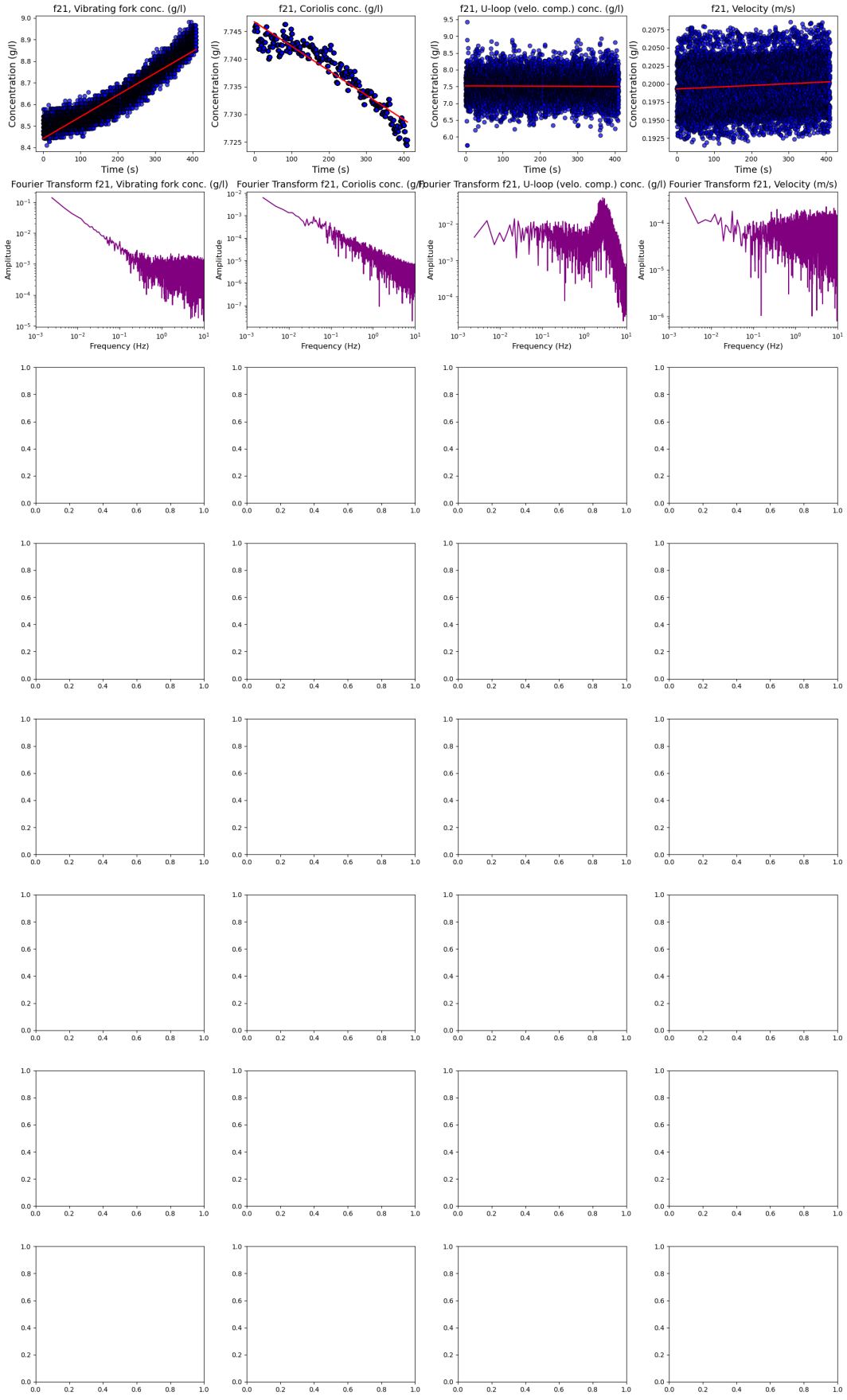

Figure C.24: F series time-series and Fourier transfer (f21)

D

Statistical data

	Absolute relative error (%)			
Target concentration (g/L)	**Manual sample**	**Vibrating fork**	**Coriolis**	**U-loop**
B series				
5	17.59	124.73	11.69	
10	28.61	44.17	13.63	
20	41.05	23.76	19.90	
40	46.26	10.76	25.83	
80	53.38	18.35	31.54	51.82
160	66.18	11.21	38.76	57.99
C series				
5	5.15	70.72	10.70	38.71
10	2.09	69.65	4.35	42.66
20	3.11	43.11	2.47	6.41
40	1.58	45.84	2.10	4.12
80	0.20	25.01	2.59	1.16
160	0.49	3.22	2.83	1.84
D series				
5	3.89	32.23	9.85	21.08
10	3.63	64.62	5.27	9.87
20	2.88	18.24	2.91	8.32
40	1.55	1.45	0.53	3.49
80	0.99	4.17	1.13	2.08
160	1.35	5.18	1.07	2.41
F series				
5	19.63	62.63	3.69	8.82
10	11.60	17.72	7.00	7.31
20	13.51	15.00	0.87	5.81
40	11.85	9.31	2.02	6.65
80	7.10	8.83	1.56	4.34
160	9.41	7.83	1.97	3.53

Table D.1: Absolute relative error per target concentration per test series

	Standard deviation (g/L)			
Target concentration (g/L)	**Manual sample**	**Vibrating fork**	**Coriolis**	**U-loop**
B series				
0	0.000	1.177	0.027	6.061
5	0.751	1.783	0.080	
10	0.586	0.672	0.105	
20	2.862	0.884	0.170	
40	3.121	1.051	0.401	
80	8.544	1.030	0.945	7.490
160	18.159	1.552	1.828	8.225
C series				
0	0.000	1.177	0.027	6.061
5	0.080	2.949	0.039	6.529
10	0.156	1.169	0.059	6.648
20	0.295	2.305	0.076	6.824
40	0.486	1.831	0.082	7.183
80	0.492	1.151	0.086	6.711
160	2.460	0.809	0.169	7.412
D series				
0	0.000	1.177	0.027	6.061
5	0.044	1.092	0.031	6.551
10	0.042	0.794	0.045	6.541
20	0.092	0.969	0.033	7.224
40	0.314	0.966	0.032	7.348
80	0.805	0.829	0.034	6.621
160	1.599	0.927	0.031	6.254
F series				
0	0.000	0.770	0.029	5.603
5	0.069	0.761	0.057	5.295
10	0.057	0.854	0.045	5.574
20	0.058	0.878	0.062	5.262
40	0.111	0.918	0.039	5.479
80	0.412	0.710	0.035	5.686
160	0.690	3.218	0.506	12.225

Table D.2: Standard deviation per target concentration per test series

E

CFD study

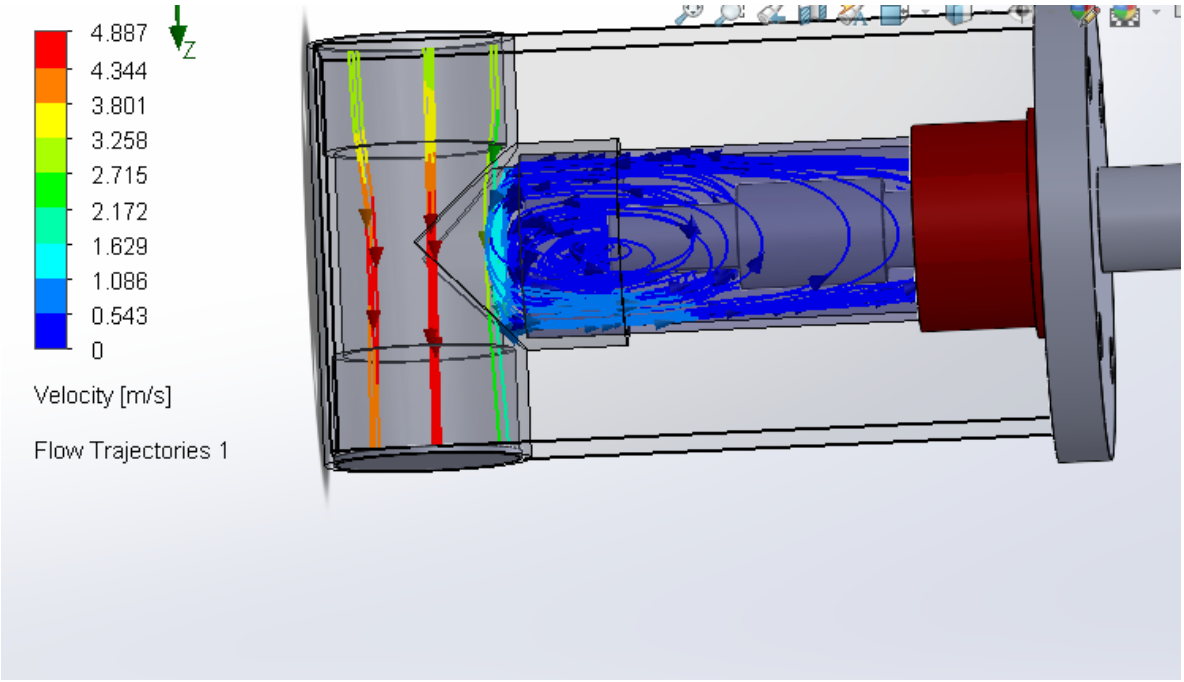

Figure E.1: CFD study T section

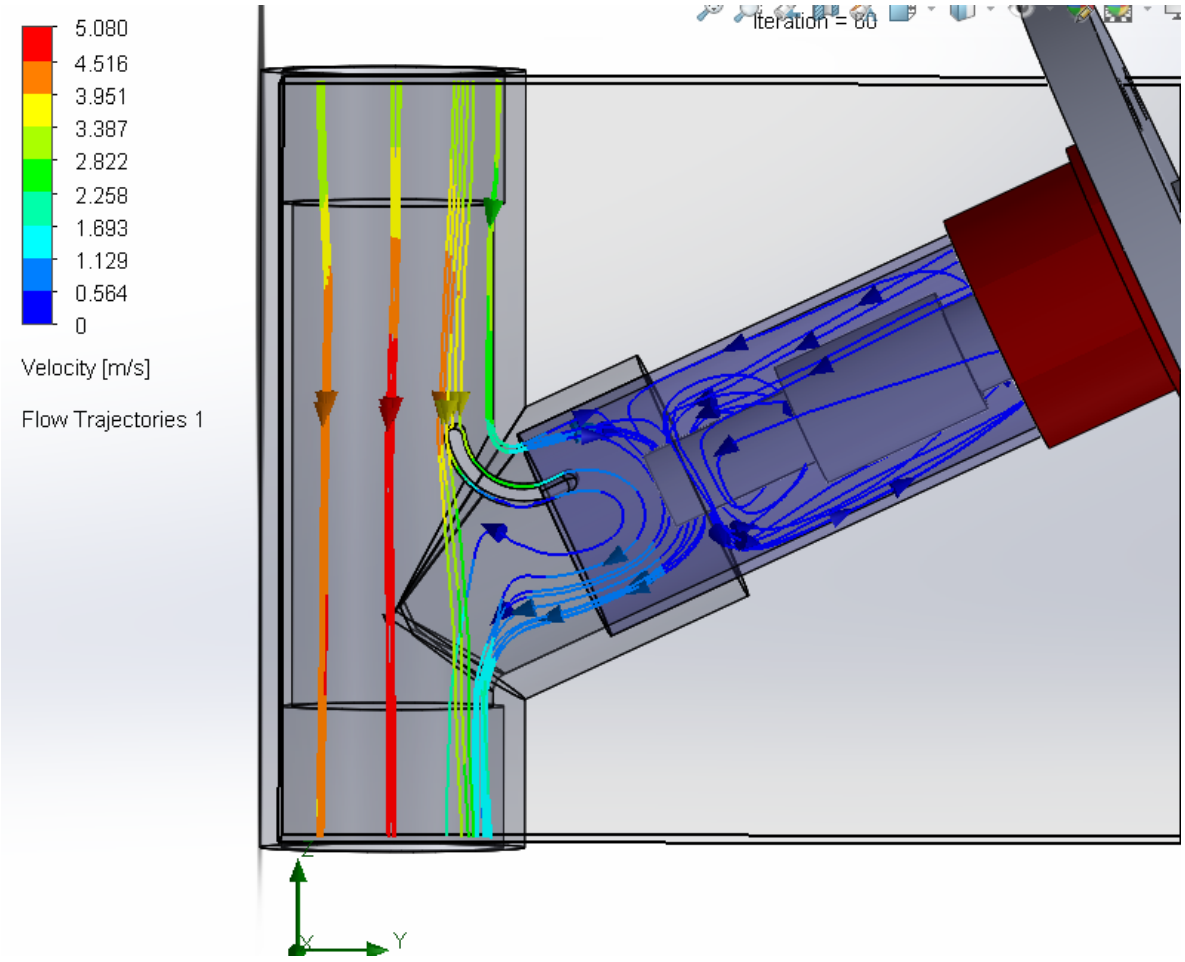

Figure E.2: CFD study Y section

F

Python Code

Python code: Calculated pressure drop U-loop

```python
import math
import pandas as pd  # For creating the table
import matplotlib.pyplot as plt

# Constants and given data
rho_w = 1000        # Density of water (kg/m^3)
d = 0.04            # Pipe diameter (m)
mu = 0.001          # Dynamic viscosity (Pa·s)
epsilon = 0.0000015  # Pipe roughness (m)
h = 1.02            # Pipe height or length (m)
g = 9.81            # Acceleration due to gravity (m/s^2)

# Function to solve Colebrook-White equation for friction factor
def colebrook_white(Re, d, epsilon):
    """
    Solve the Colebrook-White equation iteratively for the friction factor.
    Returns both the final friction factor and the list of iterations for plotting.
    """
    f_guess = 0.02
    f_iterations = [f_guess]  # Record the initial guess

    for _ in range(100):  # Iterate to refine the solution
        f_new = 1 / (2 * math.log10((epsilon / d) / 3.7 + 2.51 / (Re * math.sqrt(f_guess))))**2
        f_iterations.append(f_new)  # Record each iteration
        if abs(f_new - f_guess) < 1e-6:  # Convergence criteria
            return f_new, f_iterations
        f_guess = f_new

    return f_guess, f_iterations

# Function to calculate pressures
def calculate_pressures(rho_m, rho_w, g, h, delta_p_r):
    """
    Calculate the pressures Δp1 and Δp2 based on the given parameters.
    """
    delta_basis = (rho_m - rho_w) * g * h  # Pressure difference due to gravity
    delta_p_1_flow = delta_basis + delta_p_r  # Δp1 with flow
    delta_p_2_flow = delta_basis - delta_p_r  # Δp2 with flow

    return delta_p_1_flow, delta_p_2_flow, delta_basis
```

```
41
42 # Mixture densities and velocities to loop through
43 mixture_densities = [1000, 1098]
44 velocities = [0, 4]
45
46 # Initialize a list to store the results for the table
47 results = []
48
49 # Loop through each combination of density and velocity
50 for rho_m in mixture_densities:
51     for v in velocities:
52         if v == 0:
53             Re = 0
54             f = 0
55             delta_p_r = 0
56             f_iterations = []
57         else:
58             Re = (rho_m * v * d) / mu
59             f, f_iterations = colebrook_white(Re, d, epsilon)
60             delta_p_r = f * (h / d) * (rho_m * v**2) / 2
61
62         # Calculate pressures
63         delta_p_1_flow, delta_p_2_flow, delta_basis = calculate_pressures(
64             rho_m, rho_w, g, h, delta_p_r
65         )
66
67         # Append results to the list
68         results.append({
69             "Mixture Density (kg/m^3)": rho_m,
70             "Velocity (m/s)": v,
71             "Reynolds Number": f"{Re:.2f}",
72             "Friction Factor": f"{f:.6f}",
73             "Pressure Loss Δ(P, Pa)": f"{delta_p_r:.2f}",
74             "Δp1 (Flow, Pa)": f"{delta_p_1_flow:.2f}",
75             "Δp2 (Flow, Pa)": f"{delta_p_2_flow:.2f}"
76         })
77
78         # Plot the friction factor iterations for visualization
79         if f_iterations:
80             plt.plot(f_iterations, marker='o', label=f"Re={Re:.2f}, v={v} m/s")
81
82 # Convert the results list to a DataFrame for tabular display
83 df = pd.DataFrame(results)
84
85 # Display the friction factor iteration graph
86 plt.title("Friction Factor Iterations (Colebrook-White)")
87 plt.xlabel("Iteration Step")
88 plt.ylabel("Friction Factor (f)")
89 plt.legend()
90 plt.grid()
91 plt.show()
92
93 # Print the table
94 print(df)
```

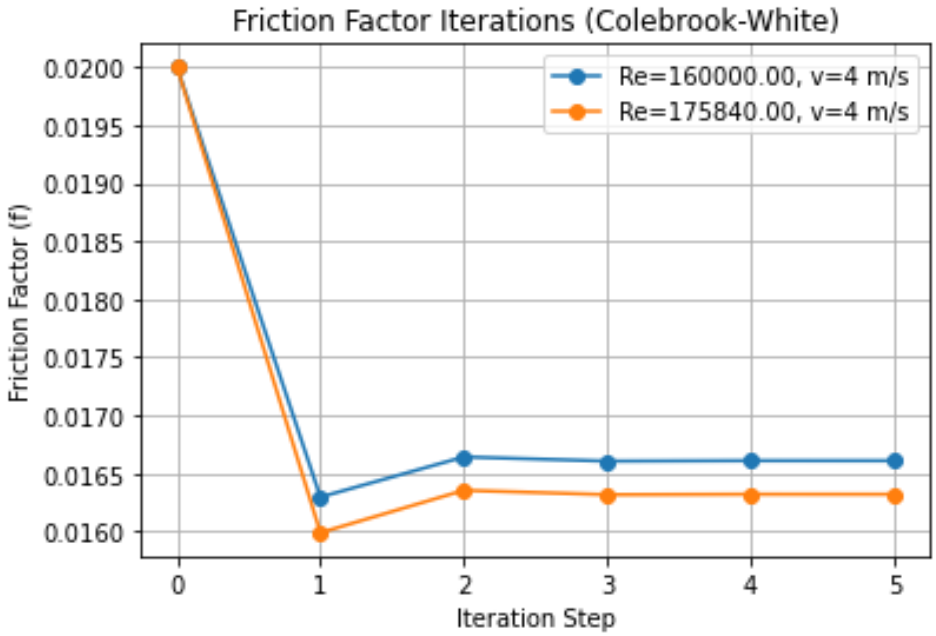

Figure F.1: Iterative calculation of the friction factor

Python code: Merge data of two DAC's

```python
import pandas as pd
import os

# Specify the series (e.g., 'd' for d series, 'b' for b series)
series = 'd'  # Change this to 'b' for b series or any other series

# Get the current working directory
current_directory = os.path.dirname(os.path.abspath(__file__))

# Loop through each pair of D0 to D18 and corresponding Prolink files
for i in range(1, 22):
    # Define file paths
    prolink_file_path = os.path.join(current_directory, f'{series}{i} prolink.xlsx')
    d_file_path = os.path.join(current_directory, f'{series}{i}.xlsx')
    output_file_path = os.path.join(current_directory, f'merged_{series}{i}.xlsx')

    # Check if both files exist before processing
    if not (os.path.exists(prolink_file_path) and os.path.exists(d_file_path)):
        print(f"Files for {series}{i} not found. Skipping.")
        continue

    # Load Prolink data with header row at index 4
    prolink_df = pd.read_excel(prolink_file_path, header=4)
    # Load D1 data
    d_df = pd.read_excel(d_file_path)

    # Select only relevant columns and rename for easier access
    prolink_df = prolink_df[['Unnamed: 0', 'sec', 'g/l', '°C']].rename(columns={
        'Unnamed: 0': 'DateTime',       # DateTime column
        'sec': 'Elapsed_Time',          # Elapsed time in seconds
        'g/l': 'Density',               # Density
        '°C': 'Temperature'             # Temperature
    })
```

```
34
35      # Convert DateTime and Elapsed_Time columns to appropriate types
36      prolink_df['DateTime'] = pd.to_datetime(prolink_df['DateTime'], errors='coerce
            ')
37      prolink_df['Elapsed_Time'] = pd.to_numeric(prolink_df['Elapsed_Time'], errors=
            'coerce')
38
39      # Drop rows with missing values in essential columns
40      prolink_df = prolink_df.dropna(subset=['DateTime', 'Elapsed_Time', 'Density',
            'Temperature'])
41
42      # Set DateTime as the index for resampling
43      prolink_df.set_index('DateTime', inplace=True)
44
45      # Resample in 1-second intervals and calculate mean values for Density and
            Temperature
46      prolink_resampled = prolink_df.resample('2S').mean().reset_index()
47
48      # Convert DateTime in D1 file to ensure alignment
49      d_df['Time'] = pd.to_datetime(d_df['Time'], errors='coerce')
50      d_df = d_df.dropna(subset=['Time'])
51
52      # Merge the resampled Prolink data with D1 based on nearest DateTime
53      merged_df = pd.merge_asof(d_df.sort_values('Time'), prolink_resampled.
            sort_values('DateTime'),
54                                left_on='Time', right_on='DateTime', direction='
                                    nearest')
55
56      # Drop the extra DateTime column from Prolink after merging
57      merged_df.drop(columns=['DateTime'], inplace=True)
58
59      # Save the result to a new file
60      merged_df.to_excel(output_file_path, index=False)
61      print(f"Merged file saved as {output_file_path}")
```

Python code: Calculate concentration from density and temperature

```
1  import os
2  import pandas as pd
3
4  # Define constants
5  sediment_density = 2620  # kg/m³
6  g = 9.81  # Gravity constant (m/s²)
7  h = 1.02  # Height constant (m)
8
9  # Correction values for U-loop (velocity compensated) density calculation
10 c1 = 2.209610517  # Replace with the actual correction value for d1, d4, d7, etc.
11 c2 = 4.844631673  # Replace with the actual correction value for d2, d5, d8, etc.
12 c3 = 8.503409931  # Replace with the actual correction value for d3, d6, d9, etc.
13
14 # Get the current working directory
15 current_directory = os.path.dirname(os.path.abspath(__file__))
16
17 # Define the water density calculation function based on temperature
18 def calculate_water_density(temperature):
19     a0 = 9.99864928 * 10**2
20     a1 = 5.72357369 * 10**(-2)
21     a2 = -7.96007024 * 10**(-3)
22     a3 = 5.32777547 * 10**(-5)
23     a4 = -2.6032268 * 10**(-7)
24     a5 = 5.11178237 * 10**(-10)
```

```
    return (a0 + a1 * temperature + a2 * temperature**2 + a3 * temperature**3 + a4 * temperature**4 + a5 * temperature**5)

# Define a function to calculate concentration
def calculate_concentration(sensor_value, water_density):
    return (sensor_value - water_density) / (1 - (water_density / sediment_density))

# Define a function to calculate U-loop (pressure compensated) density
def calculate_u_loop_pressure_density(dp1, dp2, water_density):
    dp1_2 = dp1 + 31.293
    dp2_2 = dp2 + 35.426
    return ((dp1_2 + dp2_2) / (2 * g * h)) + water_density

# Determine correction value for U-loop (velocity compensated) based on file index
def get_correction_value(file_index):
    if file_index % 3 == 1:  # d1, d4, d7, etc.
        return c1
    elif file_index % 3 == 2:  # d2, d5, d8, etc.
        return c2
    else:  # d3, d6, d9, etc.
        return c3

# Loop through each file from merged_d0 to merged_d18
for i in range(1, 22):
    file_name = f'merged_d{i}.xlsx'
    file_path = os.path.join(current_directory, file_name)

    # Check if the file exists
    if not os.path.exists(file_path):
        print(f"{file_name} not found. Skipping.")
        continue

    # Load the Excel file
    df = pd.read_excel(file_path)

    # Add calculated columns
    df['Water Density (kg/m3)'] = df['Temperature'].apply(calculate_water_density)
    df['Fork Conc. (g/l)'] = df.apply(
        lambda row: calculate_concentration(row['Fork (Formula Result)'], row['Water Density (kg/m3)']), axis=1
    )
    df['U-loop Conc. (g/l)'] = df.apply(
        lambda row: calculate_concentration(row['DP1 (Formula Result) 1'], row['Water Density (kg/m3)']), axis=1
    )
    df['Coriolis Conc. (g/l)'] = df.apply(
        lambda row: calculate_concentration(row['Density'], row['Water Density (kg/m3)']), axis=1
    )
    df['DP1.2'] = df['DP1 (Formula Result)'] + 31.293
    df['DP2.2'] = df['DP2 (Formula Result)'] + 35.426
    df['U-loop (pressure compensated) density (kg/m3)'] = df.apply(
        lambda row: calculate_u_loop_pressure_density(row['DP1 (Formula Result)'], row['DP2 (Formula Result)'], row['Water Density (kg/m3)']), axis=1
    )
    df['U-loop (press. comp.) Conc. (g/l)'] = df.apply(
        lambda row: calculate_concentration(row['U-loop (pressure compensated) density (kg/m3)'], row['Water Density (kg/m3)']), axis=1
    )

```

```
    # Calculate U-loop (velocity compensated) density with appropriate correction
    correction_value = get_correction_value(i)
    df['U-loop (velocity compensated) density (kg/m3)'] = df['U-loop (pressure
        compensated) density (kg/m3)'] + correction_value

    # Calculate U-loop (velocity compensated) concentration
    df['U-loop (velo. comp.) Conc. (g/l)'] = df.apply(
        lambda row: calculate_concentration(row['U-loop (velocity compensated)
            density (kg/m3)'], row['Water Density (kg/m3)']), axis=1
    )

    # Calculate Density Fork2 (kg/m3)
    df['Density Fork2 (kg/m3)'] = df['Fork'] * 628.52 - 618.84

    # Calculate Fork2 Concentration (g/l)
    df['Fork2 Conc. (g/l)'] = df.apply(
        lambda row: calculate_concentration(row['Density Fork2 (kg/m3)'], row['
            Water Density (kg/m3)']), axis=1
    )

    # Arrange the columns as requested, with original columns first
    original_columns = [col for col in df.columns if col not in [
        'Water Density (kg/m3)', 'DP1.2', 'DP2.2', 'U-loop (pressure compensated)
            density (kg/m3)', 'U-loop (velocity compensated) density (kg/m3)',
        'Fork Conc. (g/l)', 'Coriolis Conc. (g/l)', 'U-loop Conc. (g/l)',
        'U-loop (press. comp.) Conc. (g/l)', 'U-loop (velo. comp.) Conc. (g/l)', '
            Density Fork2 (kg/m3)', 'Fork2 Conc. (g/l)'
    ]]
    calculated_columns = [
        'Water Density (kg/m3)', 'DP1.2', 'DP2.2', 'U-loop (pressure compensated)
            density (kg/m3)', 'U-loop (velocity compensated) density (kg/m3)',
        'Fork Conc. (g/l)', 'Coriolis Conc. (g/l)', 'U-loop Conc. (g/l)',
        'U-loop (press. comp.) Conc. (g/l)', 'U-loop (velo. comp.) Conc. (g/l)', '
            Density Fork2 (kg/m3)', 'Fork2 Conc. (g/l)'
    ]

    # Reorder the DataFrame with original columns first and calculated columns at
        the end
    df = df[original_columns + calculated_columns]

    # Save the updated DataFrame, overwriting the original file
    df.to_excel(file_path, index=False)
    print(f"The file {file_name} has been updated with calculated columns at the
        end.")
```

G

Sediment Settling Velocity

Sediment particles settle due to gravity, with the terminal settling velocity w_0 occurring when drag equals gravitational force. Settling velocity is important to know to predict sediment behaviour in the hopper. The equation by Ferguson and Church (2004) provides a broad-range solution:

$$\Delta = \frac{\rho_s - \rho_w}{\rho_w} \tag{G.1}$$

$$w_0 = \frac{\Delta g\, d^2}{C_1\, \nu + \sqrt{0.75\, C_2\, \Delta\, g\, d^3}} \tag{G.2}$$

Where:

- w_0 (m/s): Terminal settling velocity.
- g (m/s^2): Gravitational acceleration.
- d (m): Diameter of sediment particles.
- $C_1 = 18$, $C_2 = 1$: Empirical constants for natural sands.
- Δ: Density ratio between sediment and water (dimensionless).
- ν (m^2/s): Kinematic viscosity of water.

In practice, collective settling reduces individual settling speeds. Richardson and Zaki (1954) describe this phenomenon as:

$$w_s = w_0(1 - c_v)^n \tag{G.3}$$

Where:

- w_s: Settling velocity considering sediment concentration (m/s).
- c_v: Sediment volume concentration.
- n: Exponent dependent on Reynolds number.

The exponent n can be computed using Rowe's (1987) method for laminar to turbulent transition:

$$Re_p = \frac{w_0\, d}{\nu}, \quad n = \frac{4.7 + 0.41\, Re_p^{0.75}}{1 + 0.175\, Re_p^{0.75}} \tag{G.4}$$

Where:

- Re_p: Particle Reynolds number (dimensionless).

Table G.1: Settling velocities (w_s) in cm/s for varying diameters and concentrations.

Diameter (μm)	$c = 5$ **(g/L)**	$c = 10$ **(g/L)**	$c = 20$ **(g/L)**	$c = 40$ **(g/L)**	$c = 80$ **(g/L)**	$c = 160$ **(g/L)**
1.00	0.00009	0.00009	0.00008	0.00008	0.00008	0.00007
5.00	0.0022	0.0021	0.0021	0.0020	0.0019	0.0016
10.00	0.0086	0.0085	0.0084	0.0081	0.0075	0.0065
50.00	0.2033	0.2015	0.1980	0.1911	0.1780	0.1537
100.00	0.7302	0.7241	0.7121	0.6885	0.6431	0.5594
250.00	3.1133	3.0919	3.0495	2.9660	2.8039	2.4992

H

Sieve Analyses

ZEEFANALYSE NEN-EN 933-1

	Frac Gr	Frac %	Cum %
300µm	0.2	0.2	100
250µm	10.6	10.6	89
212µm	10.2	10.2	79
180µm	15.8	15.8	63
150µm	31.8	31.9	31
125µm	19.0	19.0	12
106µm	5.5	5.5	7
90µm	3.0	3.0	4
REST	3.8	3.8	0

Figure H.1: Sieve analysis Multiquartz HN

Granulometry (%):

fraction	typ.	warranty
>63 µm	< 0,01	< 0,1
>20 µm	1	<5
10-20µm	4	
5-10µm	10	
2-5 µm	24	
<2 µm	61	> 50
D_{50} µm	1,3	

Figure H.2: Sieve analysis Koalin Zettlitz Ia